Chair of Nonferrous Metallurgy

Doctoral Thesis

NANOMETALLURGY OF NONFERROUS METALS

Diego Santa Rosa Coradini, Mestre

July 6, 2023

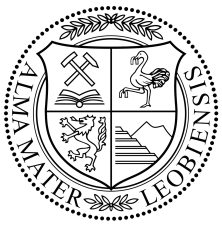

MONTAUNIVERSITÄT LEOBEN

www.unileoben.ac.at

Affidavit

I declare on oath that I wrote this thesis independently, did not use other than the specified sources and aids, and did not use any unauthorized aids. I declare that I have read, understood, and complied with the guidelines of the senate of the Montanuniversitaet Leoben for "Good Scientific Practice". Furthermore, I declare that the electronic and printed version of the submitted thesis are identical, both, formally and with regard to content.

Date July 6, 2023

Signature Author

Diego Santa Rosa Coradini

Abstract

Intensive developments have been carried out in the field of nanometallurgy in recent decades.The majority of these developments concern the miniaturization of devices and the improvement of their performance while reducing their volume. In addition, novel applications in environmental preservation and medicine, such as sensors and filters, are also being explored. The main reason for this development lies in the surface properties that can strongly influence the properties of nanoscale materials. For example, the electrical conductivity of nanoscale Cu wires coated with graphene can be increased. However, the resistance in pure nanomaterials, such as Cu NW (nanowire) without coating, increases due to surface effects. Additionally, another classical effect at the nanoscale is the lowering of the melting point. The present work aims to investigate degradation effects at the nanoscale by observing the behavior of Cu NW when exposed to a cold plasma environment, revealing a strong oxidation effect. Nanowires were also heated in a transmission electron microscope (TEM), where an unexpected sublimation effect was observed. In-situ alloying was also tested by heating a binary combination of an Al lamella of nanomaterials with Cu ND and Au nanoparticles (NP). A TEM was used for the characterization of in-situ alloying formation. Techniques such as selected-area electron diffraction (SAED), high-resolution atomic imaging, bright-field TEM (BFTEM), and high-angle annular dark-field TEM (HAADF) are employed for material characterization. The composition analysis was performed using energy-dispersive spectroscopy (EDS) prior to the experiments. In-situ heating was achieved using a microelectromechanical system (MEMS) in the form of a silicon E-chip. Different heating programs were applied depending on the phenomena under investigation. For sublimation experiments, heating ramps were conducted in the temperature range of 600 °C to 850 °C. In the

case of nanoalloying experiments, the temperatures used depended on the alloying system. For example, the Al/Cu system was melted at 660 °C and annealed at 440 °C for 5 minutes. The melting temperature for the Al/Au system was 660 °C, and the annealing temperature was 250 °C for a duration of 2 hours.

Zusammenfassung

In den letzten Jahrzehnten wurden intensive Entwicklungen im Bereich der Nanometallurgie durchgeführt. Der größte Teil davon betrifft die Miniaturisierung von Geräten und die Verbesserung ihrer Leistung bei gleichzeitiger Verringerung ihres Volumens. Darüber hinaus werden auch neue Anwendungen im Bereich des Umweltschutzes und der Medizin, wie Sensoren und Filter, erforscht. Der Hauptgrund für diese Entwicklung liegt in den Oberflächeneigenschaften, die bei nanometrischen Materialien deren Eigenschaften stärker beeinflussen können. So kann beispielsweise die elektrische Leitfähigkeit von nanometrischen Cu-Drähten, die mit Graphen beschichtet sind, erhöht werden. Der Widerstand in reinen Nanomaterialien – wie z. B. Cu ND (Nanodraht) ohne Beschichtung - erhöht sich jedoch aufgrund der Oberflächeneffekte. Zudem liegt mit der Schmelzpunktsenkung ein weiterer klassischer Effekt im Nanomaßstab.

Die vorliegende Arbeit zielt darauf ab, Degradationseffekte im Nanomaßstab zu untersuchen, indem beobachtet wird, wie sich Cu-Nanodrähte (ND) verhalten, wenn sie einer kalten Plasmaumgebung ausgesetzt werden, ein starker Oxidationseffekt festgestellt. Nanodrähte wurden auch in einem Transmissionselektronenmikroskop (TEM) erhitzt, wobei ein unerwarteter Sublimationseffekt festgestellt eintritt. Das In-situ-Legieren wurde ebenfalls getestet, indem eine binäre Kombination aus einer Al-Lamelle von Nanomaterialen mit Cu ND und Au Nanopartikeln (NP) erhitzt wurde.

Ein TEM wurde eingestze für die Charakterisierung der In-situ-Legierung-Bildung Anwendung. Für die Materialcharakterisierung kommen Techniken wie die Elektronenbeugung mit ausgewählter Fläche (SAED), hochauflösende atomare Bildgebung, Hellfeld (BFTEM) und Hochwinkel-Dunkelfeld (HAADF) zum Einsatz. Mithilfe der elektronendispersiven Spektroskopie (EDS) erfolgte eine Analyse der Zusam-

mensetzung im vorlauf der Experimente. Die In-situ-Erhitzung wurde mithilfe eines mikroelektronischen mechanischen Systems (MEMS) in Form eines Silizium-E-Chips erreicht. Je nach den untersuchten Phänomenen verschiedene Heizprogramme Anwendung.

Für Sublimationsexperimente wurden Heizrampen im Temperaturbereich von 600 °C bis 850 °C durchgeführt. Bei Nanolegierungsexperimenter richteten sich die verwendeten Temperaturen nach dem Legierungssystem, z. B. wurde das Al/Cu-System bei 750 °C geschmolzen und 5 Minuten lang bei 440 °C geglüht. Die Schmelztemperatur für das Al/Au-System lag bei 800 °C und die Glühtemperatur bei 250 °C für eine Dauer von 2 h.

Danksagung

Die Möglichkeit bekommen zu haben in Österreich arbeiten zu dürfen war ein wichtiger und bedeutender Meilenstein in meiner professionellen Laufbahn sowie auch in meinem privaten Leben. Ich bin dem Lehrstuhl der Nichteisenmetallurgie sehr dankbar für die Unterstützung, die mir in den letzten Jahren entgegengebracht wurde, daher möchte ich mich bei einigen Personen, die mich während meiner Zeit auf der Montanuniversität begleitet haben, bedanken. Als Erstes möchte ich mich bei meinem Betreuer Prof Stefan Pogatscher für die tatkräftige Unterstützung, Geduld und das Vertrauen, dass in mich gesetzt wurde, bedanken. Ich bin auch sehr dankbar, dass ich am Lehrstuhl für Nichteisenmetallurgie viel Unterstützung von meinen KollegInnen erfahren habe und gute Freundschaften knüpfen konnte. Durch meine großartigen KollegInnen war es immer einfach Motivation zu finden. Mein Dank gilt auch den Sekretariaten für ihre hervorragende Arbeit. Ich möchte mich außerdem bei Thomas M. Kremmer, Luigi Cattini, Matheus A. Tunes und Peter J. Uggowitzer für ihre Unterstützung mit dem TEM (Transmissionselektronenmikroskopie), ihre Freundschaft, die Zeit, die sie mir gewidmet haben und für die Meinungen, die mit mir geteilt wurden, bedanken. Ebenfalls bin ich meiner Familie und meinen Freunden in Brasilien sehr dankbar, da sie trotz der Entfernung stets für mich da waren. Besonders möchte ich mich bei meiner Freundin Barbara Schaffer danken, für die Zeit, Geduld und Liebe, die sie mir während herausfordernden Zeiten entgegengebracht hat.

Contents

Chapter 1

Introduction

Advances in technology are nourishing society with relevant new features such as electric cars, the ability to leave the surface of the earth, enjoy fast travels around the globe, and more. However, many of these applications are double-edged swords since the comfort promoted by them degrades the environment around us. Therefore, the necessity of optimization and new solutions are an important factor, leading society to gather efforts in the creation of sustainable ways of production. One unexpected front of science that is giving creative and positive results are emerging in nanotechnology, where possible applications range from water treatment to improving energy generation and electrothermal properties of materials [1, 2, 3, 4, 5]. Besides the environmental relevance, nanomaterials-related advances are also studied in the field of metallurgy. For instance, the field of nanometallurgy focuses on improving properties by studying nanometric-sized phases and new techniques of production. One example can be found in producing a new Al-alloy that can withstand radiation in an interstellar environment due to the stability of nanometric-sized phases [6, 7]. As stated, many applications and new solutions exploit the use of nanomaterials, but why is this class so applicable and widely discussed in this new epoch of science?

One possible way to answer it would be by mentioning a terminology called size-effect, which is responsible for many different properties between bulk and nanomaterials. The size-effect can be described by the surface-to-volume ratio factor (SVR) which increases with decreasing in volume [8, 9, 10, 11, 12]. Such properties either allow the usage of material in metastable conditions or impair or limit their

usage. Case in point, Si nanowires (NWs) used as anodes in lithium-ion batteries lose retention capacity during usage due to the loss of Si [13]. Another reported NW susceptible to degradation is the Ag NWs when used as an electrode. Typically, it can be affected by Rayleigh instability over critical temperatures. Under a specific range of UV light, it can have its partial breakage accelerated [14]. Another reported degradation mechanism occurs under electrical stress, where a NW network can suffer cracks or percolate while suffering Joule heating [14, 15]. Furthermore, sublimation and oxidation are also possible degradation mechanisms. For example, Cu NWs are susceptible to oxidization under low-reactive plasma environments and can sublimate when heated within a transmission electron microscope (TEM) [12, 16]. Additional sublimation effects were also reported for Ag nanoparticles, and Mg pillars while heated in a low-pressure environment like a TEM [17, 18]. Therefore, the goal of this thesis is to present a new methodology that could be used to study, produce, and alloys on a nanometric scale within the TEM. The alloy system study will be Al-Au and Al-Cu systems. The methodology consists of the work of Quick and Tunes et al. [6], where an electron-transparent 50 μm piece is heated within the TEM. Additionally, the thesis will also discuss the limitations that could impair this methodology, such as Cu NW degradation [12, 16].

1.1 Approach

The main goal of this thesis is to describe and discuss nanometallurgy on the nanoscale, going from topics like degradation, size-effect, and alloying. For the work sequence, to test properly the capabilities of the TEM, and in situ heating of the specimens, different setups were tested. The sequence consisted of the observation of Cu NW degradation under a plasma environment [12], studying its stability while heated within a TEM [16], afterward nanoalloying was attempted by using Cu NW, and Au Np in conjunction with a TEM lamella [19]. For the Cu NW degradation block, Cu NWs were subjected to distinct environments. At first, they were exposed to low-reactive plasma for different time frames. The goal consisted of observing their stability by characterizing it before and after the experiments. The

results observed led to the paper described in section 4 called "Degradation of Cu nanowires in a low-reactive plasma environment" [12]. The second aspect studied was the Cu NW behavior while heated within a TEM (low-pressure environment). The heating sequences were heating ramps varying from 873 to 1123 K, and the temperature was held until appreciable effects were observed. The second work resulted in the paper called "Unravelling nanometallurgy with *in situ* electron-microscopy: a case study with Cu nanowires" [16] presented in chapter 5. Concerning the alloying block, Al was considered a solute material due to its availability, and low melting point (660°C). As for alloy elements Cu and Au were considered. Cu, because it is one of the major alloying elements present in the Al industry, and Au was considered due to well-established studies concerning thermodynamic behaviour [20, 21, 22]. Therefore, two different systems were analyzed for the alloying, Al-Au, and Al-Cu. These two systems were selected due to different solubility levels. Cu has maximum solubility of 2.5 at.% at 823 K, and Au has 0.06 at.% at 923 K [20, 23]. Furthermore, the precipitation sequences of Al_2Cu (θ) and Al_2Au(η) are well studied [23, 24]. The results of this work are presented in Chapter 6 under the name "In situ transmission electron microscopy as a toolbox for the emerging science of nanometallurgy" [19].

1.2 Document Structure

To properly elucidate the concepts of nanoalloying and the degradation of the NWs, some fundamental principles need to be summarized. Chapters 1 and 2 will give an introduction to the topic, and present the state-of-the-art on the topic of nanomaterials, presenting concepts like the thermodynamics for nanomaterials, the sublimation enthalpy, the influence of size on thermodynamic properties, the decrease in cohesive energy. In addition, some transmission electron microscope techniques, sample preparation, and in situ heating will be presented. Chapter 3 will show an overall glimpse of the methodology used in the different experimental setups used in the dissertation. Chapters 4 and 5 will highlight the results of Cu NW degradation on oxidation and sublimation when heated within a TEM. Chapter 6 shows the results

of the nanoalloys with Al-Au and Al-Cu. Chapter 7 summarizes the research and will discuss the possibility of application in industry and future follow-up work. Finally, the Appendix contains a short description of published research with major contributions from the author linked to the thesis.

1.3 Reference

[1] Madhuri Kumari, Ravinder Kumar Tomar, et al. Nanotechnology for remediation of water environment. In *IRC-SET 2021*, pages 373–385. Springer, 2022.

[2] Komal Mehta. Nanotechnology for energy and the environment. In *Nanotechnology*, pages 19–33. CRC Press, 2022.

[3] Wang C.P., Liu X.J, Ohnuma I., Kainuma R., and Ishida K. Thermodynamic Database of the Phase Diagrams in Cu-Fe Base Ternary Systems. *Journal of Phase Equilibria & Diffusion*, 25(4):320–328, 2004.

[4] Divya P Barai, Kalyani K Chichghare, Shivani S Chawhan, and Bharat A Bhanvase. Synthesis and characterization of nanofluids: Thermal conductivity, electrical conductivity and particle size distribution. In *Nanotechnology for Energy and Environmental Engineering*, pages 1–49. Springer, 2020.

[5] Jitendra S Sangwai. *Nanotechnology for energy and environmental engineering*. Springer, 2020.

[6] Matheus A Tunes, Lukas Stemper, Graeme Greaves, Peter J Uggowitzer, and Stefan Pogatscher. Prototypic lightweight alloy design for stellar-radiation environments. *Advanced Science*, 7(22):2002397, 2020.

[7] Patrick D Willenshofer, Matheus A Tunes, Ho T Vo, Lukas Stemper, Oliver Renk, Graeme Greaves, Peter J Uggowitzer, and Stefan Pogatscher. Radiation-resistant aluminium alloy for space missions in the extreme environment of the solar system. *arXiv preprint arXiv:2210.03397*, 2022.

[8] Qi WH. and Wang MP. Size effect on the cohesive energy of nanoparticle. *Journal of Materials Science Letters*, 21(22):1743–1745, 2002.

[9] Madan Singh, Sekhants'o Lara, and Spirit Tlali. Effects of size and shape on the specific heat, melting entropy and enthalpy of nanomaterials. *Journal of Taibah University for Science*, 11(6):922–929, 2017.

[10] Alexander van Teijlingen, Sean A Davis, and Simon R Hall. Size-dependent melting point depression of nickel nanoparticles. *Nanoscale Advances*, 2020.

[11] Liang LH., Liu D., and Jiang Q. Size-dependent continuous binary solution phase diagram. *Nanotechnology*, 14(4):438, 2003.

[12] Diego SR Coradini, Matheus A Tunes, Thomas M Kremmer, Claudio G Schön, Peter J Uggowitzer, and Stefan Pogatscher. Degradation of Cu nanowires in a low-reactive plasma environment. *npj Materials Degradation*, 4(1):1–8, 2020.

[13] Jeong-Hyun Cho and S Tom Picraux. Silicon nanowire degradation and stabilization during lithium cycling by sei layer formation. *Nano letters*, 14(6):3088–3095, 2014.

[14] Peiyuan Guan, Renbo Zhu, Yanzhe Zhu, Fandi Chen, Tao Wan, Zhemi Xu, Rakesh Joshi, Zhaojun Han, Long Hu, Tom Wu, et al. Performance degradation and mitigation strategies of silver nanowire networks: A review. *Critical Reviews in Solid State and Materials Sciences*, 47(3):435–459, 2022.

[15] Nicolas Charvin, Joao Resende, Dorina T Papanastasiou, David Munoz-Rojas, Carmen Jiménez, Ali Nourdine, Daniel Bellet, and Lionel Flandin. Dynamic degradation of metallic nanowire networks under electrical stress: A comparison between experiments and simulations. *Nanoscale Advances*, 3(3):675–681, 2021.

[16] Diego Santa Rosa Coradini, Matheus Araujo Tunes, Patrick Willenshofer, Cameron Quick, Thomas Kremmer, Stefan Luidold, Peter J Uggowitzer, and Stefan Pogatscher. Unravelling nanometallurgy with in situ electron-microscopy: A case study with Cu nanowires.

[17] Michael A Asoro, Desiderio Kovar, and Paulo J Ferreira. In situ transmission electron microscopy observations of sublimation in silver nanoparticles. *ACS nano*, 7(9):7844–7852, 2013.

[18] Qian Yu, Min-Min Mao, Qing-Jie Li, Xiao-Qian Fu, He Tian, Ji-Xue Li, Scott X Mao, and Ze Zhang. In situ observation on dislocation-controlled sublimation of mg nanoparticles. *Nano letters*, 16(2):1156–1160, 2016.

[19] Diego SR Coradini, Matheus A Tunes, Patrick Willenshofer, Sebastian Samberger, Thomas Kremmer, Phillip Dumitraschkewitz, Peter J Uggowitzer, and Stefan Pogatscher. In situ transmission electron microscopy as a toolbox for the emerging science of nanometallurgy. *Lab on a Chip*, 2023.

[20] Laure Bourgeois, Zezhong Zhang, Jiehua Li, and Nikhil V Medhekar. The bulk and interfacial structures of the η (Al_2Au) precipitate phase. *Acta Materialia*, 105:284–293, 2016.

[21] Kenichi Nakajima, Osamu Takeda, Takahiro Miki, Kazuyo Matsubae, Shinichiro Nakamura, and Tetsuya Nagasaka. Thermodynamic analysis of contamination by alloying elements in aluminum recycling. *Environmental science & technology*, 44(14):5594–5600, 2010.

[22] Rana RS., Rajesh Purohit, and Das S. Reviews on the influences of alloying elements on the microstructure and mechanical properties of aluminum alloys and aluminum alloy composites. *International Journal of Scientific and research publications*, 2(6):1–7, 2012.

[23] Murray JL., Okamoto H., and Massalski TB. The Al-Au (aluminum-gold) system. *Bulletin of Alloy Phase Diagrams*, 8(1):20–30, 1987.

[24] V Raghavan. Al-Au-Cu (aluminum-gold-copper). *Journal of Phase Equilibria and Diffusion*, 29(3):260–261, 2008.

Chapter 2

State of the art

2.1 Market and applications

Miniaturization is an outcome of the development of information technology due to the desire of manufacturing smaller, cheaper, and faster devices [1]. For instance, the reduction in size of the transistor from 7 to 2 nm of size can lower power consumption by 75% and improve performance by 45% [2], which, states one of the milestones of miniaturization. Moreover, the astounding growth in performance and integration of transistors allow the construction of integrated circuits as small as 2 nm [1, 2]. The decrease in size and change in costs over the years is showcased in figure 2.1 inset (a), where the decrease in the size of electronic features over time is presented. Inset (b), on the other hand, shows the trade-off between the decrease in the cost of transistor production over time versus the increase in the price of the technology used to manufacture them. However, the increase in investment pays off due to the breadth of nanomaterial applications, ranging from health care to the aerospacial industry [3, 4, 5, 6, 7, 8, 9]. For example, in the medical field, nanomaterials can be used as drug-delivery systems and biosensors [10, 11]. Environmental engineering uses nanofilters for water cleaning and waste recycling. In the case of polymers, nanoadditives can be added within the process to improve the properties of the recycled material [12, 11]. Other applications comprise the adoption of nanoadditives to depolymerize polymers back to monomers for recycling [13, 11] and nanostructuring materials via additive manufacturing which

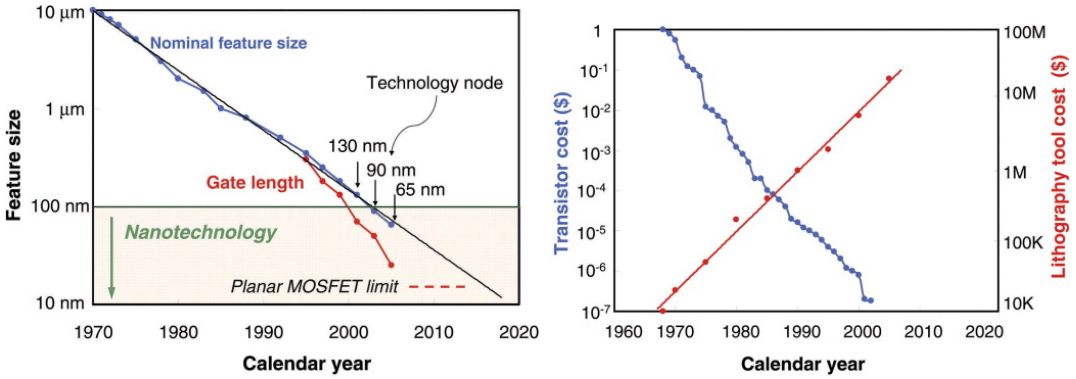

Figure 2.1: Figure 1 displays the correlation between the technological advance in the transistor industry over time by presenting (a) the decrease in the size of the transistor over the years; (b) shows the decrease in the cost of production of the transistors, and the increase in the cost of the lithographic tool along the years beginning from 1970 up to 2020.[23]

can positively affect the final product properties [14]. Nevertheless, complex manufacturing methods are necessary to enable such applications. Production-wise, two different classifications are considered: top-down and bottom-up processes. The top-down process focuses on atomizing a bulk precursor, which can agglomerate in a film [15, 11]. Bottom-up aims at producing material by using basic fundamental blocks like atoms or molecules to generate its final product [16, 17, 18, 11]. As a general example of the top-down route, one could refer to nanolithography [19, 18, 11], where the material is etched from bulk to the desired volume. For the bottom-up route, one can consider techniques like chemical-vapor deposition (CVD), and plasma or flame spraying synthesis [20, 21, 11]. Furthermore, the global nanomaterials market size is expected to have a growth rate of 14.1% from 2021 to 2028, additionally, the market size was estimated at USD 11.3 billion in 2020 [22].

Therefore, it is important to note that miniaturization comes with nanometric-size materials defined by their dimensions. More specifically, this class of materials must have one of its dimensions in a size range of 1 to 100 nm [24]. In addition to it, due to its size different properties arise, which are different than that of its bulk counterparts can be found. A classical example can be found in the literature on topics like melting temperature depression, or Rayleigh instability to mention a few [25, 26].

2.2 Thermodynamics

Historically, thermodynamics is an intriguing topic to many scientists throughout the years. One major breakthrough occurred in the development of early steam engines in the 17th century, to help solve an energy crisis in London[27]. This development has also helped in the establishment of the thermodynamic principles that are called the zeroth, first, second, and third law [28, 29, 30]. The Zeroth law, however, was defined only later on around 1930.

- The Zeroth law of thermodynamics provides a foundation for temperature in a system. It is considered that equilibrium occurs when different systems in contact reach the same temperature [28, 29, 30].

- The first law defines the conservation of energy within a thermodynamic process in a closed system. The change in the internal energy (δU_{system}) is equal to the difference between the heat supplied δQ_{system} and the work δW_{system} executed by the system namely $\delta U_{system} = \delta Q_{system} - \delta W_{system}$ [31]. Hence, energy can be transformed from one to another, but not created nor destroyed [28, 29, 30].

- The Second law defines the irreversibility of a natural event and implies the existence of entropy ∂S, and is calculated by the relation $\partial S = \partial q_{rev}/T$. One way of showcasing it is by stating that energy does not spontaneously transfer from a colder to a hotter body. So, the second law has a broad spectrum of application, whereas it can state if a phenomenon is reversible or irreversible. A phenomenon is reversible when $\delta S_{Universe} = \partial Q/T$, and indicates spontaneity and irreversibility when $\delta S_{Universe} > \partial Q/T$ [28, 29, 30]. It is important to know that reversibility and irreversibility are only possible to define when the universal conditions are known. Hence, no loss of information exists. On the other hand, while analyzing the entropy of a system the latter is not true, mainly due to loss of information to the surrounding [28, 29, 30].

- Finally, the Third law shows that the entropy of a system approaches a con-

stant value when the temperature is near absolute zero. For the zero absolute, however, the system reaches its ground state, where the minimum thermal energy is achieved, thus, the system has only one configuration or microstate. It is impossible to find such conditions since the material can possess different possible microstates due to atomic vibration, material configuration, and so on [28, 29, 30]. Therefore, entropy can be calculated according to the Boltzmann principle [28, 30, 29], $S = k_b * ln\Omega$. Where S is the entropy of the system, k_b is the Boltzmann constant and Ω is the number of microstates [28, 29, 30].

2.2.1 Free energy

Free energy can be seen as the energy or work available in a system to promote a reaction or transformation. Thus, by knowing the volume changes and entropic changes one could understand how the system evolves or reaches equilibrium. However, a problem in that interpretation is the necessity of knowing the universal entropy, which is almost an impossible task [30]. A solution for that matter was first proposed by the German physicist Hermann von Helmholtz and was postulated as $A = E - TS$, where A is the Helmholtz free energy, E is energy, T temperature, and S entropy[32]. For that matter, he considers that a closed volume would only change heat with the surrounding until an equilibrium would be reached, in that scenario no volume change would occur. Equation 2.1 to 2.4 shows a simple formal demonstration of Helmholtz free energy.

$$dU = dq - dW \tag{2.1}$$

Considering the second law is presented equation 2.2.

$$dS = dq/T \tag{2.2}$$

For a constant volume $dw = d(P * V) = VdP$. So, equation2.3 can be found.

$$dU = TdS - VdP \tag{2.3}$$

So, the equation 2.4 can be calculated

$$dA = d(U - TS) = dW \tag{2.4}$$

So, with that Helmholtz free energy is $dA = d(U - TS)$, where values lesser than zero represent a spontaneous process and 0 equilibrium. Moreover, the equation allows the calculation of the maximum useful work that a system can provide at constant temperature and volume. On the other hand, Gibbs free energy is calculated in a different way where the pressure and the temperature of the system were constant, and the volume would change. Therefore, by considering the equations 2.1, and 2.2 under the mentioned conditions equation 2.5 can be found.

$$dU = TdS - pdV \tag{2.5}$$

By knowing the definition of enthalpy, where $dH = du + pdV$. The following relation can be calculated

$$dG = dH - TdS = 0 \tag{2.6}$$

As observed, the conditions adopted $dH - TdS$ would result in 0, which would be an equilibrium condition. However, G energy shows the spontaneity of a reaction by presenting $dG < 0$, otherwise for $dG > 0$ would present a non-spontaneous reaction. Unlike Helmholtz equation, Gibbs equation shows free energy as being the difference between the enthalpy and heat lost by the system and can return the maximum reversible work done by the system. With that in mind, table 2.1 shows the main differences between the Gibbs and Helmholtz free energy.

Table 2.1: Comparison between Gibbs and Helmholtz free energy

Gibbs free energy	Helmholtz free energy
Can define the maximum reversible work obtained from a particular system	Can define the useful work within a closed system
Calculated for systems under constant pressure and temperature	Calculated for systems under constant temperature and volume
Spontaneous reaction or transformation for $\partial G < 0$	Spontaneous reaction or transformation for $\partial A > 0$

So, because of the difference in nature between the two formulations, their applicability is different. Normally, Helmholtz free energy is used when change of pressure is not feasible. As an example, an explosive reaction would require the use of Helmholtz-free energy due to pressure changes within the system [33]. On the other hand, Gibbs's energy is considered in situations where transformations occur in constant pressure situations. Therefore, for the present work, Gibbs's free energy formulation was chosen due to the constant pressure environment found within the TEM chamber.

2.2.2 Phase diagram

Materials in nature can be of many different phases, which possess defined boundaries and unique states like solid, liquid, and gaseous [34]. These different phases can be plotted in a phase diagram and they work like a chart showing how to obtain a unique phase while being in an equilibrium condition [36]. Therefore, the state variables used to define a system are pressure, volume, concentration, and temperature [34, 36]. Moreover, a phase diagram can be calculated by using principles like Gibbs free energy [37, 36]. Where a pressure versus temperature phase diagram can be given by comparing dG/dT with dP/dT (the same calculation can be executed with composition instead of temperature or pressure). Additionally, for the calculation of complex systems with many phases, computational methods like CALPHAD (Calculation of Phase diagrams) are used [37]. However, for the

validation and improvement of a calculated phase diagram, empirical experiments are necessary [36]. Commonly, for alloys, the material is heated to a specific temperature until equilibrium is reached, after that its properties are measured and compared [34, 36]. For measuring, techniques like thermal analysis (TA), X-ray diffraction (XRD), dilatometry, and electrical conductivity can be used to observe it [38]. The necessity of these measurements is associated with the physical-chemical properties changes that occur after a phase transformation [34]. Nevertheless, due to the nature of the state equations, a phase diagram only shows an equilibrium stage, which might not represent reality due to kinetic reasons [39]. Another factor, that may affect the representation of the phase diagram can be found in the size of a sample [26]. Nanometric-sized samples can present different properties than their bulk counterpart due to the surface energy. For example, Equation 2.7 shows the total Gibbs free energy for a nanomaterial [40].

$$G^{Total,nano} = G^{Bulk} + G^{Surface} \tag{2.7}$$

Where $G^{Surface}$ can be presented as equations 2.8 and 2.9.

$$G^{Surface} = 2 * C * \sigma_i * V_i / r_{sphere} \tag{2.8}$$

$$G^{Surface} = 2 * C * \sigma_i * V_i / r_{cylinder} \tag{2.9}$$

Where C is the correction factor concerning the surface tension measurement, V_i is the molar volume of the component i, σ_i is the surface energy of component i, and r is the radius of the measured volume (either sphere or cylinder). Figure 2.2 shows the difference between the phase diagrams of a nanometric alloy, and its bulk counterpart presented by Ghasemi et al. [40].

2.2.3 Size effect

Although the field of nanomaterials has experienced significant development in recent years, the size effect has been recognized since the mid-nineteenth century. In

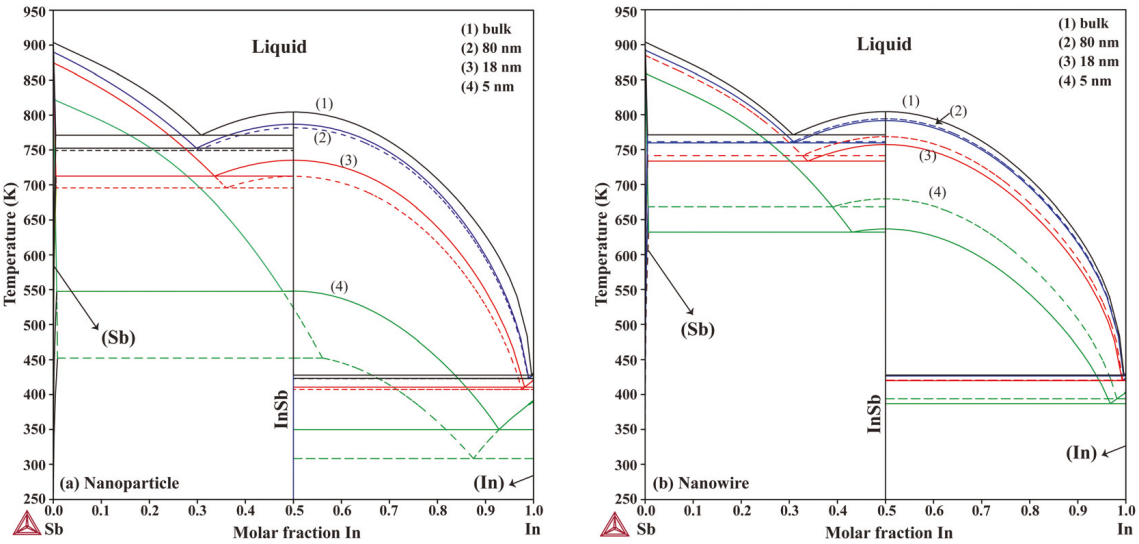

Figure 2.2: Calculated phase diagram considering nanometric dimensions plotted by Ghasemi et al [40]. (a) nanoparticles and (b) nanowires for a radius of 5, 18, and 80 nm. Solid lines represent the calculated diagram with the assumed relevant surface energy for InSb nanoparticles and nanowires, {111} and {110} surface energies, respectively. For comparison, nanoparticles phase diagrams with {110} surface energy of InSb and nanowires with {111} surface energy of InSb is also calculated and displayed with dashed lines.

fact, Faraday observed that the melting point of a surface occurs at a lower temperature than the bulk melting point [41]. However, it was not until 1909 that the concept of size dependence of surface energy was proposed by Pawlow [42], leading to a breakthrough in our understanding of the size effect. The size effect can be inferred from the first law of thermodynamics and from Gibbs free energy, as shown in Equation 2.10, where pressure, temperature, and number of moles in the system are held constant.

$$dG_{surface} = dE_{int} - TdS + 2\gamma dA \tag{2.10}$$

Here, $dG_{surface}$ represents the change in free energy caused by the surface, dE_{int} represents the energy within the bulk of the system, dS represents the change in entropy, T represents temperature, and γ represents surface tension. In this formulation, the difference between Equations 2.1 to 2.6 lies in the terms for internal energy (dU) and work (dW), where $dU = dE_{int} + dE_{surf}$ and $dW = \gamma dA$. Different methods can be used to describe the size-dependent behavior, such as Lindemann's hypothesis, shown in Equation 2.11.

$$T_{m(r)}/T_{m(\infty)} = \exp[-(\alpha - 1)/(r/3h - 1)^{-1})] \tag{2.11}$$

Where $T_{m(r)}$ and $T_{m(\infty)}$ are the melting point of the particle in question and bulk, respectively, r represents the radius of a spherical particle, h stands for the height of the atomic monolayer at the surface of atoms on a bulk crystal. The constant α is a ratio between the atomic displacement at the surface, and at the volume of the particle [41]. In addition to these observations, the influence of the size on other properties like cohesive energy, sublimation behaviour, oxidation, and other degradation processes was also observed [43, 44, 45, 46, 25, 26]. So, describing concepts like surface energy volume-to-surface ratio, cohesive energy, and other size-related properties need to be elucidated. Equation 2.12 showcases the effects of the size over cohesive energy [48], the energy required to separate bonded atoms apart [47, 25].

$$E_{tot} = E_0 * (n - N) + (1/2) * E_0 * N \tag{2.12}$$

The equation calculates the cohesive energy (E_{tot}), by taking into account the energy contribution of the interior atoms N. For that, the number of atoms within a nanosolid (N) is subtracted from the number of atoms at the first layer of the surface n. E_0 in the equation stands for the cohesive energy per atom. [48]. So to calculate it per mole the equation can be written as presented in Equation 2.13.

$$E_n = A * E_{tot}/n \tag{2.13}$$

E_n is the energy per mole, and A is the Avogrado number. The same behaviour can be observed for the melting temperature of a nanosolid [25, 48]. The equation 2.14 shows the relationship between the melting temperature of nanosolid (T_{mn}) vs the melting temperature of the bulk material T_{mb}.

$$T_{mn} = T_{mb} * (1 - N)/2n \tag{2.14}$$

Qi and Wang also made a model that described this effect with a shape factor (α) [25]. The factor is described in Equation 2.15 by the ratio between the surface area of the nanoparticle (S) and its surface of any shape (S´). Where S´ is given by Equation 2.15.

$$S' = \alpha 4\pi R^2 \tag{2.15}$$

Moreover, by this factor and considering particles and atoms being spherical, one could find Equation 2.16, which shows the cohesive energy of a particle by taking into account the shape factor.

$$E_p = E_0(1 - 6\alpha r/D) \tag{2.16}$$

Despite only two different methods being described here, different models can be used to define the decrease of the cohesive energy due to the size effect. Besides, it is also possible to understand these effects indirectly, one example would be by means of the change in partial vapor pressure [49]. Furthermore, cohesive energy in a solid can be calculated through the slope of the enthalpy of sublimation and the standard enthalpy of formation for elemental metals [50].

2.3 Sublimation enthalpy

By definition, sublimation occurs when a material transforms from solid to gas. So, for it to occur the energy given to the material need to be enough to reach the maximum heat capacity in the solid state, sever all interatomic interaction that holds the substance together, and provide enough energy to allow the unbounded atoms to transform to the gaseous state [51]. Hence, sublimation enthalpy can be calculated as described in Equation 2.17, where it is the sum of the whole energy necessary to achieve the gas phase, heating from a solid phase [51].

$$\Delta H_{sub} = \Delta H_{therm_{solid}} + \Delta H_{lantent_{solid-liq}} + \Delta H_{therm_{liquid}} + \Delta H_{latent_{liqui-gas}} \tag{2.17}$$

Whereas $\Delta H_{therm_{solid}}$ is the energy necessary to heat a solid to its melting point, $\Delta H_{latent_{solid-liq}}$ is latent heating of melting, $\Delta H_{therm_{liquid}}$ is the energy necessary to heat the material to its vaporization point, and the $\Delta H_{latent_{liqui-gas}}$ is the energy to vaporize the liquid. To define its energy empirically, the most successful method for indirect measurement consists of the Knudsen-cell mass-loss method [52, 53]. Direct measurements can take advantage of *in situ* transmission electron microscope methodologies, whereas direct observation and measurement of the kinetic phenomena is possible [11, 43]. Moreover, sublimation enthalpy is a fundamental property of metal since through it one can measure its cohesive energy [54].

2.3.1 Sublimation mechanism

As noted sublimation can be calculated by summing the whole energy needed from the solid state to the gaseous state. However, this formulation does not consider kinetics or the activation energy for the process to take place. Moreover, phase transitions from solid to gas or liquid to gas are pressure dependent [55]. For instance, different equations were developed to tackle these changes. Equation 2.18 shows the Clausius-Clapeyron equation [55].

$$dP/dT = \delta s/\delta \upsilon = (L/t)/\delta \upsilon \tag{2.18}$$

Where dP/dT is the slope of the curve pressure versus temperature, L is the latent heat of sublimation, $\delta \upsilon$ is the specifics volume, and δs is the specific entropy change of the phase transition. The equation shows the temperature for phase transformation at a specific temperature and pressure [55]. Additionally, another famous equation used to define phase transformation under different pressures or temperatures condition is the Kelvin equation presented in equation 2.19 [49].

$$ln(p/p_{sat}) = (2\gamma V_m)/(r * R * T) \tag{2.19}$$

Where p is the vapor pressure at a temperature T, p_{sat} is the saturated one, γ is the liquid/vapor surface tension, V_m is molar volume, R is the universal gas

constant and r is the radius of the droplet. Thus, the phase equilibrium depends on the droplet size, where smaller drops are capable of vaporizing earlier than bigger ones. Moreover, the equation also defines the curvature of the droplet in accordance with the difference between vapor pressure, and the measured pressure. For $p_{sat} > p$ the droplet is convex, and for $p > p_{sat}$ the droplet is concave [56, 57]. Since the Kelvin equation can be derived from the Gibbs equation considering a transformation from liquid to gas, the same approach can be used for solid to gas. Different applications came out to define the sublimation temperature, and pressure of nanometric size solid clusters, nanowires, and different kinds of nanomaterials [43, 58, 11]. The sublimation mechanism of metals was described by Somorjai [53]. In his work, it was considered that the activation energy for sublimation is equal to the heat of sublimation determined by a steady-state sublimation regime [53]. Further, it was considered that sublimation is a step-wise process, in which the atoms at the surface turn into adatoms and sublimate [53]. Taking it into account, it is possible to infer that sublimation can be a complex mechanism dependent on many different variables. Moreover, it can be indirectly measured by using the Knudsen effusion experiments, where the mass loss of a material over time for a certain pressure can be quantified [53, 59, 60]. Figure 2.3 presents a sketch of a Knudsen cell.

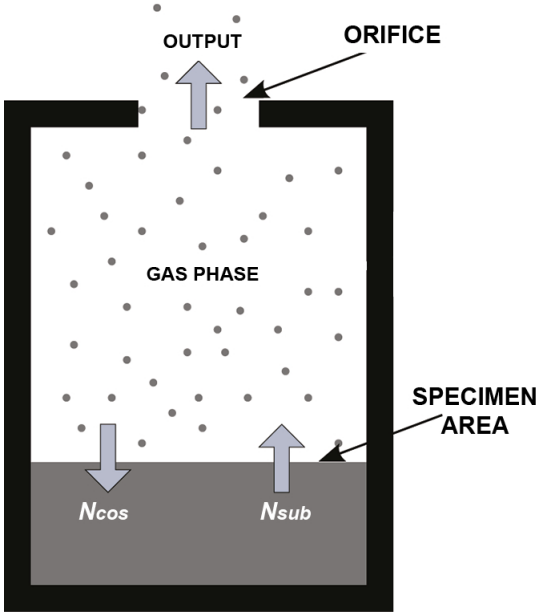

Figure 2.3: Schematic drawing of the Knudsen cell based on the work from Wetzel et al [59]. In the picture, the sketch shows where a sublimation achieved equilibrium. The sublimation rate is measured through the orifice by means of mass loss. Ncos stands for the number of atoms condensing, and Nsub the number of atoms sublimating.

So, by means of such an apparatus equation 2.20 is formulated [61].

$$\Gamma = m * dN_e/Ae * dt = \alpha_v(m/2 * \pi * k_b * T)^{(1/2)}(P^0 - P) \tag{2.20}$$

Where Γ is the amount of condensed phase formed or sublimated, m is the molar mass, A_e is the area of sublimation, N_e is the number of evaporating atoms, k_b is the Boltzmann constant, T temperature, P^0 is the equilibrium vapor pressure, and P is the pressure acting over the sample. As noted the equation shows the mass variation over time, for constant pressure and temperature. Therefore, by applying such conditions one can build an Arrhenius plot, and calculate back the enthalpy of sublimation [11], confirming if the studied conditions correspond to sublimation or not. Table 2.2 shows the sublimation energy for different metals.

Table 2.2: Sublimation enthalpy of different metals.

Metals	Sublimation enthalpy $[kJ * mol^{-1}]$
Ag	284.8 [62]
Cu	337.2 [62]
Au	368.4 [62]
Fe	413 [63]
Cr	395.4 [63]
Mg	282.1 [63]
Co	423.1 [63]
V	470.3 [63]
Ti	467.1 [63]
Nb	730 [63]
Mo	657.3 [63]
Ni	428 [63]

2.4 Transmission electron microscopy

The transmission electron microscope (TEM) plays a critical role whenever macroscopic properties are related to defects or interfaces that can´t be observed by means like scanning electron microscope or light microscope. For example, GP-zone (Guinier–Preston zone) act as hardening features in Aluminum alloys and can only be observed by a TEM [64]. So the analysis of nanometric features, a transmission electron microscope (TEM) is often a tool of choice [65]. Additionally, TEM is normally described as an equipped laboratory instead of a standalone microscope. The motivation for it is given due to the many possible different analyses that can be done within it, like scanning transmission electron microscopy (STEM); diffraction analysis; dislocation analysis; chemical composition analysis; electron energy loss spectroscopy (EELS); magnetic domain analysis; atomic mass contrast (Z-contrast), or high-resolution atomic imaging [66]. Moreover, different types of TEMs can be used for different analyses like environmental TEM, that allow the

analysis of nanomaterials within a solution, or atmosphere [67]. Also, a low-voltage electron microscope can be used to study biological specimens and operate at a voltage between 5 and 25 kV [68]; Cryo-TEM is another apparatus, which uses holders capable of maintaining the sample at liquid nitrogen or helium temperatures. This technique is important for observing macromolecular assemblies such as viruses and DNA. [69].

2.4.1 TEM imaging

Similar to a transmission light microscope (LM), the conventional TEM (CTEM) is based on the same principles, whereas the image formed is a shadow of the specimen cast on a screen. However, TEM images are formed due to electron interactions with matter. Moreover, unlike LM, TEMs use electromagnetic and electrostatic lenses instead of glass lenses to correct the generated illumination source [70]. Because electrons can interact with matter as both waves and particles, they generate distinct contrast types in electron scattering and diffraction patterns in electron diffraction.[70]. Additionally to it, the use of electrons increases the resolution to the sub-nanometric level. As a matter of example, a LM resolving power can go up to 300 nm for the green light in the visible spectrum. Such a difference emerges from the difference in wavelength size between an electron and a photon. The wavelength of a photon ranges from 300 nm to 700 nm. On the other hand, an electron can have its wavelength calculated by the de Broglie equation, which states that its wavelength is inversely proportional to its momentum as presented in Equation 2.21.

$$\lambda_e = h/\sqrt{2 * m_0 * E(1 + (E/2 * m_0 * c^2))} \tag{2.21}$$

Where h, m, and c represent the Planck constant, electron mass, and speed of light, respectively. So, the expected value wavelength for an electron, when accelerated with a 200 keV TEM, is around 2 pm. To calculate the theoretical resolution of a TEM, one more step is necessary: considering the Rayleigh criterion presented by equation 2.22.

$$\delta = 0.61 * \lambda/(\mu * sin(\beta)) \tag{2.22}$$

This equation gives the resolution by taking into account the wavelength of the source, the refraction constant (μ) of the medium, and the semi-angle of collection (β) of the magnifying lens [70]. Hence, by applying the wavelength of 2 pm to the equation, considering μ to unity, and the semi-angle to 3.5 $mrad$. The approximate resolution is approximately 0.14 nm. Even though a subnanometric resolution is possible. An extensive setup is necessary to guarantee it. Figure 2.4 presents a sketch of a TEM where the main parts are presented. As observed a CTEM is comprised of many different parts that are there to provide beam stability, decrease the possible aberrations generated by the lenses, and turn the beam parallel [35]. Further, most of the TEMs need to operate under high-vacuum due to the necessity to avoid possible electrical discharges and allow electrons to travel within the instrument without interaction with the atmosphere [70]. In addition to the need for good pumps, other important choices are necessary to achieve an optimal function of the microscope, like:

- the source used to generate the electron beams;
- accelerating voltage to be used;
- the type of camera used for recording;
- capacity for *in situ* experimentation;
- necessity for scanning transmission electron microscope (STEM);
- necessity for using electron dispersive spectroscopy (EDS);
- necessity for having correctors to increase the resolving power.

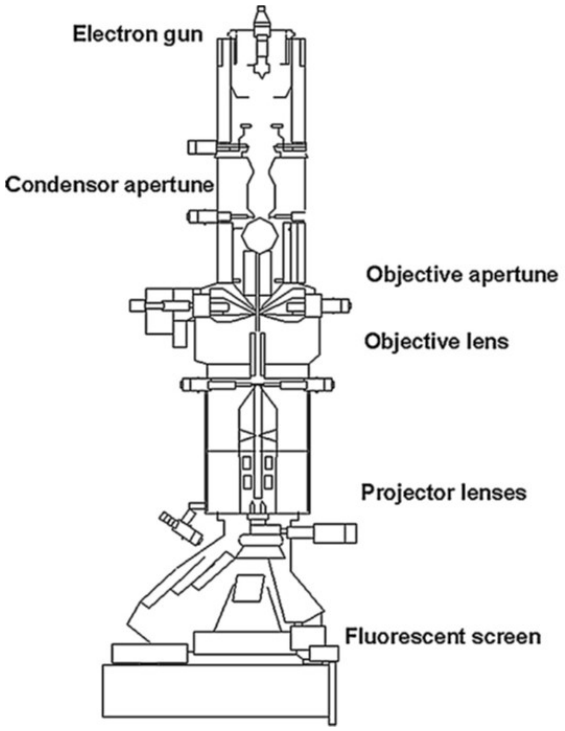

Figure 2.4: Sketch of a TEM showing the main components for functioning [71].

In addition to it, the aforementioned 3 pm of resolution is normally called the information limit of a microscope, which is not normally reached due to distinct sources like noise, bad sample preparation, lens imperfection, and machine limitations [70, 35]. Therefore, to increase the point resolution of a TEM, spherical, and chromatic correctors can be used. Another solution to enhance the TEM resolution is by increasing its acceleration voltage. However, such a method implies higher costs and increases the beam damage caused to the sample [70, 35].

2.4.2 Scanning Transmission Electron microscopy imaging

Scanning transmission electron microscopy (STEM) is a microscopy that combines the principles of scanning electron microscopy (SEM) and conventional transmission electron microscopy (CTEM). In STEM, a focused beam of electrons is transmitted through a thin sample, and the electrons that pass through the sample are collected and used to generate an image. However, unlike TEM, STEM´s focused beam scans along a whole region, instead of illuminating a bigger surface. Further, the STEM is advised to be used over TEM in cases where the specimen is too thick

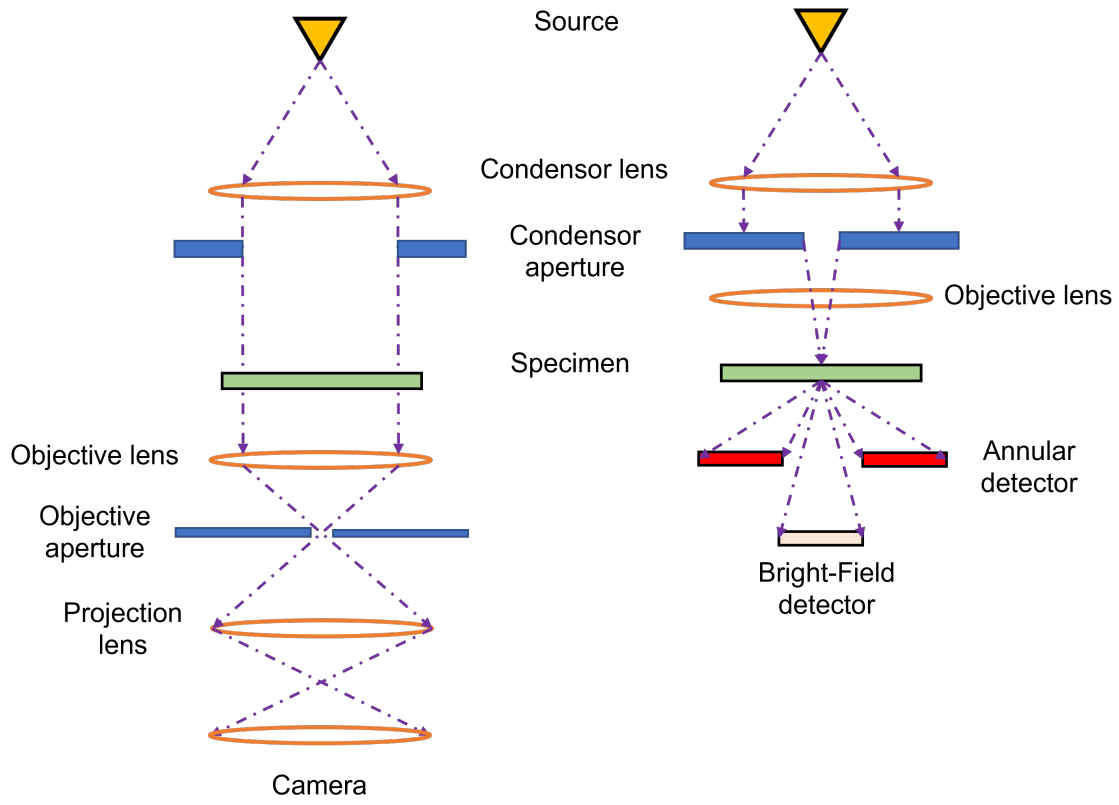

Figure 2.5: Comparison of the beam path and setups between CTEM and STEM regard to image formation.

that chromatic aberration limits its usage, the specimen is beam sensitive, and or it has low contrast in the TEM mode [70]. Moreover, a STEM microscope offers different types of images depending on the angle of scattering observed. For example, the image modes include bright field, dark field, and high-angle annular dark field (HAADF) imaging. Whereas HAADF mode is very sensitive to the material atomic mass revealing the specimen Z-contrast, which is a contrast formed by the elastic scattering of the electrons with the nucleus of the atoms. Such scattering is also known as Coulomb, or Rutheford scattering [70]. Overall, STEM offers a powerful tool for materials characterization, with the ability to provide high-resolution images and chemical information of samples by the usage of an EDS sensor exploiting the generated characteristic X-ray emanating from the sample [70]. Figure 2.5, presents a beam diagram showing how the image is formed, and the position of the camera and detectors in a CTEM and STEM setup.

2.4.3 Sample preparation

Despite the equipment setup, a good result is only obtainable through good sampling. Thus, a shared saying among TEM users, the thinner the sample, the better the results[72]. Thus, to properly prepare a specimen the first thing to be considered is in which state the material is available. For instance, a material can be prepared from a bulk sample, a thin film, or from fibers and powders [70]. So, each sample will need a different support or holder set up for its observation. Additionally to it, the type of washer to be used needs to be taken into account, and it can change depending on the morphology and chemical composition of the sample. For example, powder and fibrous material can be supported by a grid washer, while a thin TEM lamella can support itself. Figure 2.6 presents different holders setup and washers to be used on each.

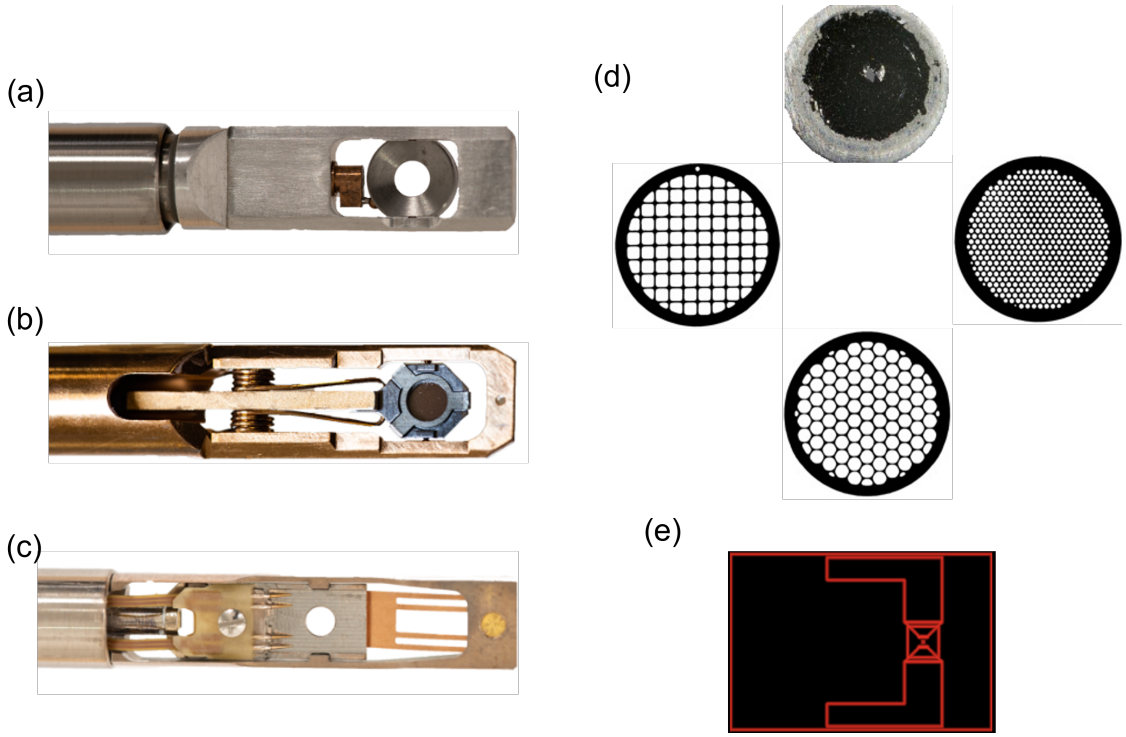

Figure 2.6: The insets show different TEM holders and distinct sample carriers. Inset (a) displays a double tilt Gatan holder capable of cryogenic in situ experiments; inset (b) shows a Thermofisher double tilt holder for 3D tomography characterization; in inset (c) one can see a protochip fusion holder for in situ heating experiments. Furthermore, inset (d) shows the possible washer used to carry powder, or fiber samples and an Al thin lamella; inset (e) presents a microelectronic mechanical specimen holder for the in situ heating fusion holder shown in inset (c).

Table 2.3: Different sample preparation techniques for TEM

Type of sample	TEM preparation method
Powder, fiber [44, 70]	Immersion of the washer in the solution, or pipetting the solution onto the washer
Organic material [70, 73, 74]	(1) Replica technique. (2) Cryfixation (3) Chemical fixation
Bulk [70, 44, 75]	(1) Precision ion polishing; (2) Focused ion beam polishing; (3) Electropolishing; (4) Mechanical polishing.
Thin film [70, 75, 76, 77]	(1) E-beam evaporation; (2) Atomic layer epitaxy; (3) Replica; (4) Photochemical etching lithography; (5) Polishing techniques used for bulk samples.

Nevertheless, prior to adding the sample to the TEM holder a preparation step is necessary depending on the type of the sample. Table 2.3 describes the different techniques according to each type of sample.

2.4.4 In situ heating

As mentioned before, different species of in situ treatments or experiments can be studied in a TEM. To illustrate some, one can study thermally activated mechanisms within a crystal [78], phase changes in nanowires, and nanoparticles [79], physical and mechanical changes in grain boundaries [80], and chemical changes in batteries or capability of nanoparticles to work as sensors [81, 82], to cite some. In spite of that, the cornerstone of that dissertation orbits around in situ heating experiments. So, some possible frameworks will be herein introduced. During heating experiments, the samples are either heated or cooled promoting phenomena like reaction and/or phase transformation that can be observed dynamically [83, 80]. There-

fore, the operator can control some of the thermodynamic parameters found within the TEM system. Unfortunately, one of the main limitations concerning parameter control is found in the high vacuum necessary to run the TEM, which hinders the observation of the effect involving gases and liquids due to sublimation and or vaporization [11]. Yet, due to these limitations, new solutions were found in modern or innovative holder setups enabling overcoming some of these [83]. Nowadays, in situ heating enables the investigation of solid-solid, solid-liquid, and solid-gas reactions [83, 70]. For each of the following systems, a unique holder is needed. Figure 2.7, hand over sketches of distinct holders used for one of the aforementioned conditions.

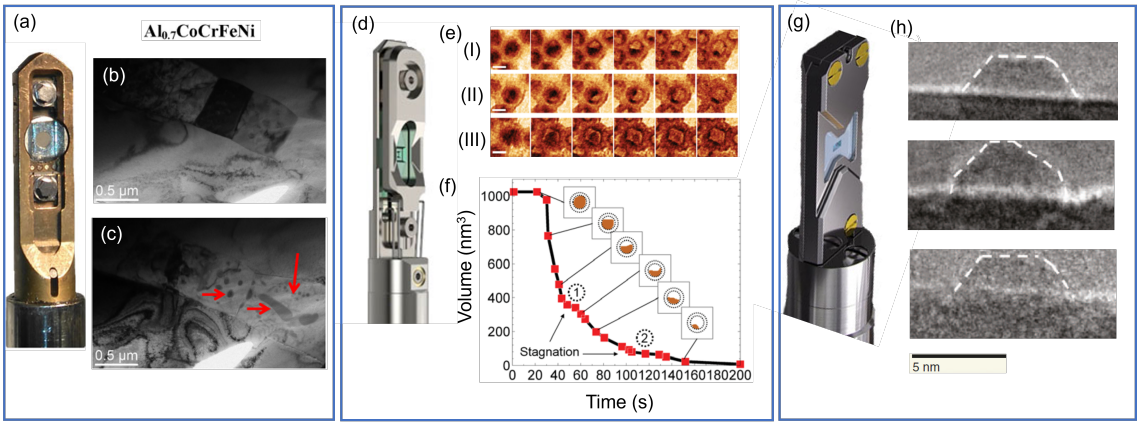

Figure 2.7: Example of different holders capable of in situ heating, where (a) shows a holder containing a solid specimen [84]; (d) a holder with solid-liquid specimens [85], (g) and an environmental holder [86]. Insets (b) and (c) present precipitates formed after in situ heating annealing of a high entropy alloy, where precipitate formation can be observed [87]; Inset (e) shows the change of a Co nanoparticle in an oxygen-rich environment, while (f) its volume decrease over time [88]; insets (h) shows a Cu nanoparticle under different liquid environment varying pure H_2 to a mixture with H_2O, where the first and the last are exposed to H_2, and the middle one exposed to 3:1 H_2:H_2O mixture [89].

However, regarding solid-solid in situ heating, another limitation can be found in the form of thermal drifting and longer waiting times until system stabilization [90]. Therefore, a possible solution for such impairment can be found in SiN microelectronic mechanical system (MEMS), which can perform fast cooling, and heating without compromising image quality, or promoting longer waiting time [86]. The holder functions through joule heating, whereas the observed area does not conduct any current with only the Cu surrounding capable of conducting electricity. In addition, the heating is controlled by the calibration file that relates the resistance

measured to the temperature, and for that specific system, it can reach a maximum temperature of 1200 °C [86]. The setup MEMS chip and holder are framed in Figure 2.8.

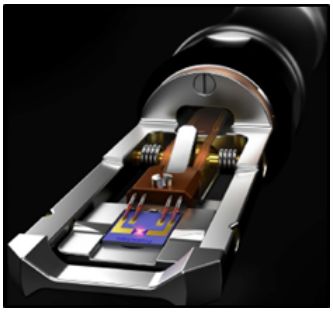

Figure 2.8: Protochip holder, with an SiN e-chip [86]

2.5 Reference

[1] Kal Renganathan Sharma. *Nanostructuring operations in nanoscale science and engineering*. McGraw-Hill Education, 2010.

[2] Samuel K Moore, Dexter Johnson, Mark Harris, Emily Waltz, Prachi Patel, and Michelle Hampson. The latest developments in technology, engineering, and science: News. *IEEE Spectrum*, 58(8):5–12, 2021.

[3] Gibson BC., Williams J.R., Fromhold Jr AT., Bozack MJ., Neely WC., and . Whitaker Ann F. The interaction of atomic oxygen with thin copper films. *The Journal of chemical physics*, 96(3):2318–2323, 1992.

[4] Robert Chau, Suman Datta, and Amlan Majumdar. Opportunities and challenges of III-V nanoelectronics for future high-speed, low-power logic applications. In *IEEE Compound Semiconductor Integrated Circuit Symposium, 2005. CSIC'05.*, pages 4–pp. IEEE, 2005.

[5] Mark L Allen, Mikko Aronniemi, Tomi Mattila, Ari Alastalo, Kimmo Ojanperä, Mika Suhonen, and Heikki Seppä. Electrical sintering of nanoparticle structures. *Nanotechnology*, 19(17):175201, 2008.

[6] Qingzhou Cui, Fan Gao, Subhadeep Mukherjee, and Zhiyong Gu. Joining and interconnect formation of nanowires and carbon nanotubes for nanoelectronics and nanosystems. *Small*, 5(11):1246–1257, 2009.

[7] Donglai Yao, Gang Zhang, and Baowen Li. A universal expression of band gap for silicon nanowires of different cross-section geometries. *Nano Letters*, 8(12):4557–4561, 2008.

[8] Mark A Koten, SA Voeller, MM Patterson, and Jeffrey E Shield. In situ measurements of plasma properties during gas-condensation of cu nanoparticles. *Journal of Applied Physics*, 119(11):114306, 2016.

[9] Inshakova E., Inshakova A., and Goncharov A. Engineered nanomaterials for energy sector: Market trends, modern applications and future prospects. In *IOP Conference Series: Materials Science and Engineering*, volume 971, page 032031. IOP Publishing, 2020.

[10] Rupesh Kumar, S Ranjith, Hrishikesh Balu, DR Bharathi, K Chandan, and Syed Sagheer Ahmed. Role of nanotechnology in biomedical applications: an updated review. *UPI Journal of Pharmaceutical, Medical and Health Sciences*, pages 39–43, 2022.

[11] Diego Santa Rosa Coradini, Matheus Araujo Tunes, Patrick Willenshofer, Cameron Quick, Thomas Kremmer, Stefan Luidold, Peter J Uggowitzer, and Stefan Pogatscher. Unravelling nanometallurgy with in situ electron-microscopy: A case study with cu nanowires.

[12] Carol López de Dicastillo, Eliezer Velásquez, Adrián Rojas, Abel Guarda, and María José Galotto. The use of nanoadditives within recycled polymers for food packaging: Properties, recyclability, and safety. *Comprehensive Reviews in Food Science and Food Safety*, 19(4):1760–1776, 2020.

[13] Monica Distaso et al. Potential contribution of nanotechnology to the circular economy of plastic materials. *Acta Innovations*, (37):57–66, 2020.

[14] Olga Ivanova, Christopher Williams, and Thomas Campbell. Additive manufacturing (am) and nanotechnology: promises and challenges. *Rapid prototyping journal*, 19(5):353–364, 2013.

[15] Oleg D Neikov and NA Yefimov. *Handbook of non-ferrous metal powders: Technologies and applications*. Elsevier, 2009.

[16] Wei Lu and Charles M Lieber. Nanoelectronics from the bottom up. *Nature materials*, 6(11):841–850, 2007.

[17] Shuguang Zhang. Building from the bottom up. *Materials Today*, 6(5):20–27, 2003.

[18] Parvez Iqbal, Jon A Preece, and Paula M Mendes. Nanotechnology: The "top-down" and "bottom-up" approaches. *Supramolecular chemistry: from molecules to nanomaterials*, 2012.

[19] Mamalis AG. Recent advances in nanotechnology. *Journal of Materials Processing Technology*, 181(1-3):52–58, 2007.

[20] Lina Marcela Hoyos-Palacio, Diana Paola Cuesta Castro, Isabel Cristina Ortiz-Trujillo, Luz Elena Botero Palacio, Beatriz Janeth Galeano Upegui, Nelson Javier Escobar Mora, and Jesus Antonio Carlos Cornelio. Compounds of carbon nanotubes decorated with silver nanoparticles via in-situ by chemical vapor deposition (cvd). *Journal of materials research and technology*, 8(6):5893–5898, 2019.

[21] Ravi BG., Sampath S., Gambino R., Parise JB., and Devi PS. Plasma spray synthesis from precursors: Progress, issues, and considerations. *Journal of thermal spray technology*, 15(4):701–707, 2006.

[22] Elena Inshakova and Oleg Inshakov. World market for nanomaterials: Structure and trends. In *MATEC web of conferences*, volume 129, page 02013. EDP Sciences, 2017.

[23] Scott E Thompson and Srivatsan Parthasarathy. Moore's law: the future of Si microelectronics. *Materials Today*, 9(6):20–25, 2006.

[24] Bin Hu, Man He, and Beibei Chen. Nanometer-sized materials for solid-phase extraction of trace elements. *Analytical and bioanalytical chemistry*, 407:2685–2710, 2015.

[25] . Qi WH and . Wang MP. Size effect on the cohesive energy of nanoparticle. *Journal of Materials Science Letters*, 21(22):1743–1745, 2002.

[26] Alexander van Teijlingen, Sean A Davis, and Simon R Hall. Size-dependent melting point depression of nickel nanoparticles. *Nanoscale Advances*, 2020.

[27] Ingo Müller. *A history of thermodynamics: The doctrine of energy and entropy*. Springer Science & Business Media, 2007.

[28] Robert J Silbey, Robert A Alberty, Moungi G Bawendi, and George A Papadantonakis. *Physical chemistry*. John Wiley & Sons, 2022.

[29] EA Guggenheim. An advanced treatment for chemists and physicists. *Thermodynamics*, 1967.

[30] Charles Kittel and Herbert Kroemer. *Thermal physics*. American Association of Physics Teachers, 1998.

[31] Kenneth S Suslick. Encyclopedia of physical science and technology. *Sonoluminescence and sonochemistry, 3rd edn. Elsevier Science Ltd, Massachusetts*, pages 1–20, 2001.

[32] Lydia Patton. Hermann von helmholtz, Dec 2018.

[33] Daniel A Crowl. Using thermodynamic availability to determine the energy of explosion. *Plant/operations progress*, 10(3):136–142, 1991.

[34] Rainer Schmid-Fetzer. Phase diagrams: the beginning of wisdom. *Journal of Phase Equilibria and Diffusion*, 35(6):735–760, 2014.

[35] Crispin Hetherington. Aberration correction for TEM. *Materials Today*, 7(12):50–55, 2004.

[36] Yong Zhong Zhan, Yong Du, and Ying Hong Zhuang. Determination of phase diagrams using equilibrated alloys. In *Methods for Phase Diagram Determination*, pages 108–150. Elsevier, 2007.

[37] Ji-Cheng Zhao. *Methods for phase diagram determination*. Elsevier, 2011.

[38] Chu-Kun Kuo, Zu-Xiang Lin, and Dong-Sheng Yan. *High temperature phase equilibria and phase diagrams*. Elsevier, 2017.

[39] A. Picone. Metal thin film growth on metals: Surfactant effects. In Klaus Wandelt, editor, *Encyclopedia of Interfacial Chemistry*, pages 221–231. Elsevier, Oxford, 2018.

[40] Masoomeh Ghasemi, Zeila Zanolli, Martin Stankovski, and Jonas Johansson. Size-and shape-dependent phase diagram of in–sb nano-alloys. *Nanoscale*, 7(41):17387–17396, 2015.

[41] Dibyendu Ganguli. Size effect in melting: a historical overview. *Transactions of the Indian Ceramic Society*, 67(2):49–62, 2008.

[42] P Pawlow. Über die Abhängigkeit des Schmelzpunktes von der Oberflächenenergie eines festen Körpers. *Zeitschrift für physikalische Chemie*, 65(1):1–35, 1909.

[43] Joanne WL Yim, Bin Xiang, and Junqiao Wu. Sublimation of GeTe nanowires and evidence of its size effect studied by in situ TEM. *Journal of the American Chemical Society*, 131(40):14526–14530, 2009.

[44] Diego SR Coradini, Matheus A Tunes, Thomas M Kremmer, Claudio G Schön, Peter J Uggowitzer, and Stefan Pogatscher. Degradation of Cu nanowires in a low-reactive plasma environment. *npj Materials Degradation*, 4(1):1–8, 2020.

[45] Peiyuan Guan, Renbo Zhu, Yanzhe Zhu, Fandi Chen, Tao Wan, Zhemi Xu, Rakesh Joshi, Zhaojun Han, Long Hu, Tom Wu, et al. Performance degradation and mitigation strategies of silver nanowire networks: A review. *Critical Reviews in Solid State and Materials Sciences*, 47(3):435–459, 2022.

[46] Shiyun Xiong, Weihong Qi, Baiyun Huang, Mingpu Wang, and Yejun Li. Size and shape dependent Gibbs free energy and phase stability of titanium and zirconium nanoparticles. *Materials Chemistry and Physics*, 120(2-3):446–451, 2010.

[47] Paul Becher. The calculation of cohesive energy density from the surface tension of liquids. *Journal of Colloid and Interface Science*, 38(2):291–293, 1972.

[48] Raghuvesh Kumar and Munish Kumar. Effect of size on cohesive energy, melting temperature and debye temperature of nanomaterials. 2012.

[49] LM Skinner and JR Sambles. The Kelvin equation—A review. *Journal of Aerosol Science*, 3(3):199–210, 1972.

[50] Behnam Farid and RW Godby. Cohesive energies of crystals. *Physical Review B*, 43(17):14248, 1991.

[51] Dixie J Goss and Ralph H Petrucci. *General Chemistry Principles & Modern Applications, Petrucci, Harwood, Herring, Madura: Study Guide*. Pearson-/Prentice Hall, 2007.

[52] Sergey Vyazovkin, Nobuyoshi Koga, Christoph Schick, Sergey P Verevkin, Dzmitry H Zaitsau, Florian Heym, René Androsch, Martin Hunkel, Holger Surm, Matthias Steinbacher, et al. *Recent advances, techniques and applications*, volume 3. Elsevier, 2002.

[53] Gabor A Somorjai. Mechanism of sublimation: Structural and chemical rearrangements at the vaporizing surface control the rate of sublimation. *Science*, 162(3855):755–760, 1968.

[54] Robert A Meyers. *Encyclopedia of physical science and technology*. Elsevier, 2001.

[55] Oliver LI Brown. The clausius-clapeyron equation. *Journal of Chemical Education*, 28(8):428, 1951.

[56] William Thomson. 4. on the equilibrium of vapour at a curved surface of liquid. *Proceedings of the Royal Society of Edinburgh*, 7:63–68, 1872.

[57] Dorothy J Woodland and Edward Mack Jr. The effect of curvature of surface on surface energy. rate of evaporation of liquid droplets. thickness of saturated vapor films. *Journal of the American Chemical Society*, 55(8):3149–3161, 1933.

[58] Felix Klein, Andrey Litnovsky, Tobias Wegener, Xiaoyue Tan, Jesus Gonzalez-Julian, Marcin Rasinski, Janina Schmitz, Christian Linsmeier, Martin Bram, and Jan Willem Coenen. Sublimation of advanced tungsten alloys under demo relevant accidental conditions. *Fusion engineering and design*, 146:1198–1202, 2019.

[59] Steffen Wetzel, Annemarie Pucci, and Hans-Peter Gail. Vapor pressure and evaporation coefficient measurements at elevated temperatures with a knudsen cell and a quartz crystal microbalance: new data for sio. *Journal of Chemical & Engineering Data*, 57(5):1594–1601, 2012.

[60] K Thomas Jacob. Knudsen effusion measurements on Cr–Mn alloys. *Z. Metallkd.*, 76(6):415–419, 1985.

[61] Jiwon Jeong, Subin Lee, Youbin Kim, Seung Min Han, Daniel Kiener, Youn-Bae Kang, and Sang Ho Oh. Microstructural evolution of a focused ion beam fabricated mg nanopillar at high temperatures: Defect annihilation and sublimation. *Scripta Materialia*, 86:44–47, 2014.

[62] JW Arblaster. Thermodynamic properties of copper. *Journal of Phase Equilibria and Diffusion*, 36:422–444, 2015.

[63] Kalman Thurnay. *Thermal properties of transition metals*. Forschungszentrum Karlsruhe Karlsruhe, 1998.

[64] Chapter 4 - Strengthening of metal alloys. In Adrian P. Mouritz, editor, *Introduction to Aerospace Materials*, pages 57–90. Woodhead Publishing, 2012.

[65] Ph Sciau. Transmission electron microscopy: Emerging investigations for cultural heritage materials. In *Advances in Imaging and Electron Physics*, volume 198, pages 43–67. Elsevier, 2016.

[66] Ray F Egerton et al. *Physical principles of electron microscopy*, volume 56. Springer, 2005.

[67] Peter A Crozier and Thomas W Hansen. In situ and operando transmission electron microscopy of catalytic materials. *MRS Bulletin*, 40(1):38–45, 2015.

[68] Jana Nebesářová and Marie Vancová. How to observe small biological objects in low voltage electron microscope. *Microscopy and Microanalysis*, 13(S03):248–249, 2007.

[69] Zongli Li, Matthew L Baker, Wen Jiang, Mary K Estes, and BV Venkataram Prasad. Rotavirus architecture at subnanometer resolution. *Journal of virology*, 83(4):1754–1766, 2009.

[70] C Barry Carter and David B Williams. *Transmission electron microscopy: Diffraction, imaging, and spectrometry*. Springer, 2016.

[71] Tang CY. and Yang Z. Transmission electron microscopy (TEM). In *Membrane characterization*, pages 145–159. Elsevier, 2017.

[72] Jeanne Ayache, Luc Beaunier, Jacqueline Boumendil, Gabrielle Ehret, and Danièle Laub. *Sample preparation handbook for transmission electron microscopy: techniques*, volume 2. Springer Science & Business Media, 2010.

[73] Mehedi Reza, Eero Kontturi, Anna-Stiina Jääskeläinen, Tapani Vuorinen, and Janne Ruokolainen. Transmission electron microscopy for wood and fiber analysis- a review. *BioResources*, 10(3):6230–6261, 2015.

[74] Suhan Kim, Moon Jeong Park, Nitash P Balsara, Gao Liu, and Andrew M Minor. Minimization of focused ion beam damage in nanostructured polymer thin films. *Ultramicroscopy*, 111(3):191–199, 2011.

[75] Lucille A Giannuzzi and Frederick A Stevie. A review of focused ion beam milling techniques for TEM specimen preparation. *Micron*, 30(3):197–204, 1999.

[76] D Theis, H Oppolzer, G Ebbinghaus, and S Schild. Cross-sectional transmission electron microscopy of electroluminescent thin films fabricated by various deposition methods. *Journal of crystal growth*, 63(1):47–57, 1983.

[77] Lynnette D Madsen, Louise Weaver, and Sissel N Jacobsen. Influence of material properties on TEM specimen preparation of thin films. *Microscopy research and technique*, 36(5):354–361, 1997.

[78] Chapter 6 - experimental studies of peierls–nabarro-type friction forces in metals and alloys. In D. Caillard and J.L. Martin, editors, *Thermally Activated Mechanisms in Crystal Plasticity*, volume 8 of *Pergamon Materials Series*, pages 159–224. Pergamon, 2003.

[79] M. Longo. Nanowire phase change memory (pcm) technologies: properties and performance. In Yoshio Nishi, editor, *Advances in Non-volatile Memory and Storage Technology*, pages 231–261. Woodhead Publishing, 2014.

[80] Y. Takahashi, H. Kondo, R. Asano, M. Takuma, K. Saitoh, S. Arai, S. Muto, and N. Tanaka. In situ micro-mechanical testing of grain boundaries combined with environmental TEM. In Lin Ye, editor, *Recent Advances in Structural Integrity Analysis - Proceedings of the International Congress (APCF/SIF-2014)*, pages 570–574. Woodhead Publishing, Oxford, 2014.

[81] Xueqing Wang, Ming Li, Pengcheng Xu, Ying Chen, Haitao Yu, and Xinxin Li. In Situ TEM Technique Revealing the Deactivation Mechanism of bimetallic Pd–Ag Nanoparticles in Hydrogen Sensors. *Nano Letters*, 22(7):3157–3164, 2022.

[82] Meng Gu, Yang He, Jianming Zheng, and Chongmin Wang. Nanoscale silicon as anode for Li-ion batteries: The fundamentals, promises, and challenges. *Nano Energy*, 17:366–383, 2015.

[83] Hiroyasu Saka, Takeo Kamino, Shigeo Ara, and Katsuhiro Sasaki. In situ heating transmission electron microscopy. *MRS bulletin*, 33(2):93–100, 2008.

[84] M Gaumé, P Baldo, Frédéric Mompiou, and F Onimus. In-situ observation of an irradiation creep deformation mechanism in zirconium alloys. *Scripta materialia*, 154:87–91, 2018.

[85] Climate sample holder, Nov 2021.

[86] Protochips. In situ tem electrothermal analysis: Fusion, Feb 2022.

[87] JC Rao, HY Diao, V Ocelík, D Vainchtein, C Zhang, C Kuo, Z Tang, W Guo, JD Poplawsky, Y Zhou, et al. Secondary phases in Al_xCoCrFeNi high-entropy alloys: An in-situ TEM heating study and thermodynamic appraisal. *Acta Materialia*, 131:206–220, 2017.

[88] Huolin L Xin, Kaiyang Niu, Daan Hein Alsem, and Haimei Zheng. In situ TEM study of catalytic nanoparticle reactions in atmospheric pressure gas environment. *Microscopy and Microanalysis*, 19(6):1558–1568, 2013.

[89] Franklin Tao and Miquel Salmeron. In situ studies of chemistry and structure of materials in reactive environments. *Science*, 331(6014):171–174, 2011.

[90] Andrew T DeLaRiva, Thomas W Hansen, Sivakumar R Challa, and Abhaya K Datye. In situ transmission electron microscopy of catalyst sintering. *Journal of catalysis*, 308:291–305, 2013.

Chapter 3

Materials, methodology, and approach

As described, the topic of nanometallurgy is a flourishing new field of study in the area of nanoengineering. A reason for such is the development of new techniques like in situ heating within a TEM and its stability which increased drastically in the last decade. Moreover, nanomaterials in general present different properties due to the size effect. So, the present work will exploit and study these properties by observing changes in the behaviour of Cu NWs under different oxidation ex-situ conditions, and TEM in-situ heating with the use of MEMS. TEM in-situ nanoalloying will be also another focus of the work. It will be attempted by using Au NPs, and Cu NWs laid upon Al thin foils. Therefore, this chapter will cover in a general way the approaches used to prepare and characterize the different samples studied over the course of this thesis, exploiting the use of MEMS technology.

3.1 Sample preparation

Different setups and samples were used for the experiments. For the nanowire preparation, two different Cu NWs specimens were supplied by SIGMA-ALDRICH, the first one in powder condition batch number MKCL4542, and the second one in an ethanol solution with lot batch number MKCL4540. For the first batch, it was necessary to prepare a liquid solution to disperse the NWs. The solution used in this work was made with 8 mg of Cu NWs for 6.8 g of isopropanol[1]. The same dilution method was used for the second batch. Ultrasonic mixing was used for

the two solutions and it was done 30 min before the TEM sample preparation to unclutter the Cu NWs in the solution. After ultrasonic mixing, the Cu NWs in solution were pipetted directly onto metallic substrates and left to dry in the air [1]. These metallic substrates consisted of 3 mm electro-polished TEM disks [1]. For the experiments, different metallic substrates were used, and the results reported here were reproduced using three different substrates (Sn, Al, and steel AISI347). For the MEMS samples, the Cu NWs were pipetted on top of the MEMS chips [1].

3.2 Substrate preparation

For the substrate preparation, the twin-jet electropolishing techniques was used. The process was carried out at a temperature of 223 K and a voltage of 12 V, where twin jets of electrolyte are pumped and shot at the sample central area promoting the removal of impurities. The thinning is caused by a chemical reaction that occurs due to the presence of a pair of electrodes, one positive and one negative. The positive electrode, or anode, is typically made of stainless steel or titanium, while the negative electrode, or cathode, was the sample itself. The solution used was a mixture of 1 : 3 HNO_3 plus methanol, and the process aimed to smooth the surface and generate an electron-transparent region around the hole punctured by the central area of the sample [1]. Figure 3.1, displays an example of the apparatus, showing the region where the hole is eroded.

3.2.1 Sample sectioning

For the nanoalloying step, it was necessary to add on top of the MEMs chips a part of the electron transparent area of an electropolished Al 3 mm disk [1]. The method consists of the manual sectioning of an electropolished disk around an electron-transparent region found around the hole in the middle of the sample. The cutting is done by sectioning the sample in half, after that, the piece is divided around the transparent region until it has a diameter of around 50 μm. After that, the piece is placed onto the e-chip with the assistance of a bristle [2, 3].

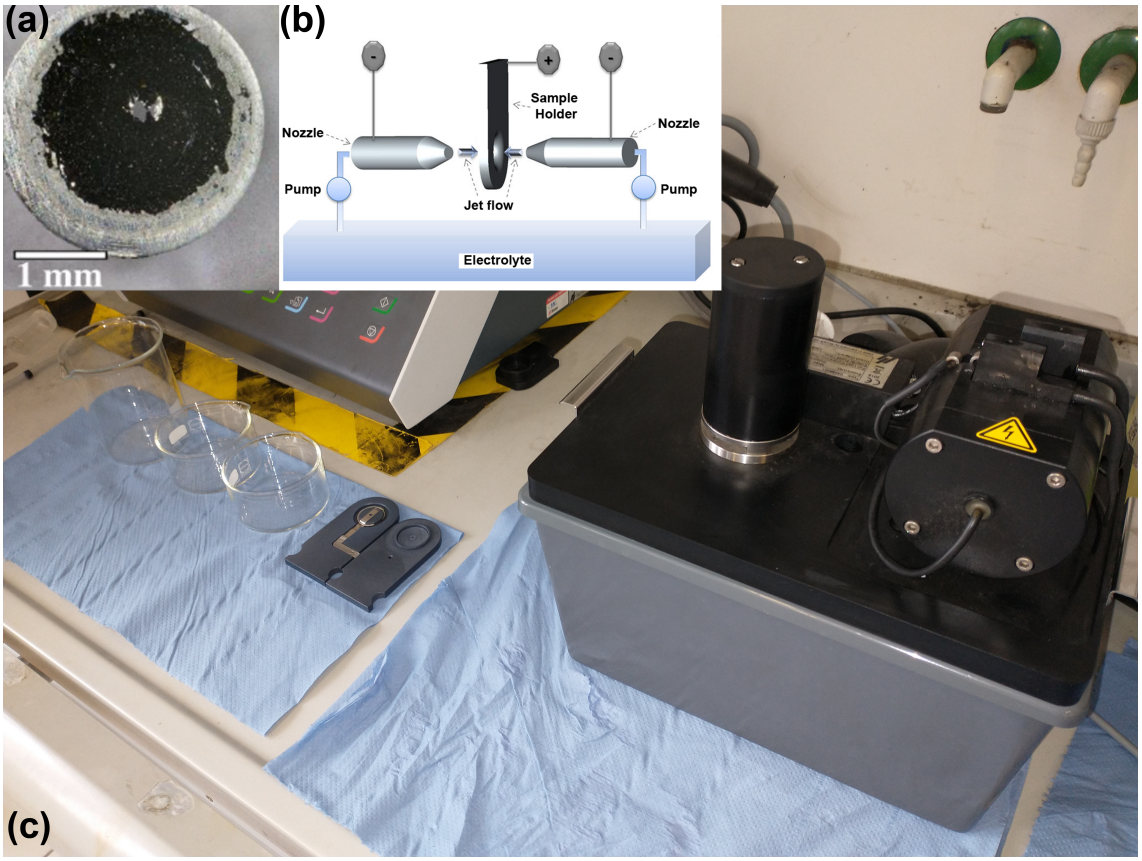

Figure 3.1: The electropolishing setup and sketch are presented in the insets (a) to (c), where inset (a) shows the electropolished sample with the hole formed in the middle of the sample; inset (b) presents a sketch showing how the equipment works [4]; (c) shows the apparatus presents in the laboratory used to electropolish the samples.

3.3 Image analysis

The microscope used to generate the image was a ThermoFisher Scientific Talos F200X G2 operated at 200 kV with a field-emission gun, and it was equipped with Super-X EDX detectors. To properly understand and characterize the phenomena being studied, pre- and post-characterization results were compared using static micrographs. This was achieved by taking bright-field TEM (BFTEM) and high-annular angle dark field (HAADF) images, as well as using STEM-EDX mapping, selected electron-area diffraction (SAED), and high-resolution imaging for material or phase characterization. To analyze ongoing effects, videos were recorded using the HAADF sensor, as Cu, Au, and Al have strong contrast differences due to their atomic masses, which results in good Z-contrast. The ThermoFisher Velox software (version 2.9) was used for image and video post-processing.

3.4 MEMS Heating programs and calibration

Different heating programs were created for various experimental setups. For the Cu sublimation assessment, the programs focused on heating to temperatures of 600, 650, 700, 750, 800, and 850°C for varying lengths of time to gather enough data to evaluate the sublimation effect. For temperature calibration, the provided calibration program by Thermofisher was sufficient. However, for the nanoalloying heating sequence, a separate calibration step was necessary. The goal was to correct the read temperature since Al melting temperature was being registered, in some cases (specifically for rapid heating) 150 °C off. So, Pure Al (99.9995%) supplied by Alfa Aesar was heated until melting was observed. After that, the calibration was replaced by the corrected one by using 660 °C and 25 °C as the calibration points. So, by using at first the wrong temperature scale as a base, the material was pre-heated to 404°C for 2 minutes to alleviate thermal stress and prevent sample displacement. Then, a heating spike increased the temperature to 510°C for 300ms before quenching to 404°C. If melting was not observed, the methodology was repeated with an additional 10°C added to the spike temperature. Melting was confirmed by a change in volume. Once calibrated, the heating programs were used for heat treatment and melting. Heat treatments were based on the research of Dumitraschkewitz et al. and Bourgeois et al. [5, 6]. Melting was achieved by heating the pure Al above 660 °C for 300 ms [6], a time frame chosen to allow for melt to occur without forming a droplet. For the heat treatments, different ones have been used accordingly to the binary system in question. For the Al-Au alloy, a 2h heating under 250 °C was used [5]. For the Al-Cu system, the sample was heated to 440 °C for 5 min [6].

3.5 Reference

[1] Diego SR Coradini, Matheus A Tunes, Thomas M Kremmer, Claudio G Schön, Peter J Uggowitzer, and Stefan Pogatscher. Degradation of Cu nanowires in a low-reactive plasma environment. *npj Materials Degradation*, 4(1):1–8, 2020.

[2] Matheus A Tunes, Cameron R Quick, Lukas Stemper, Diego SR Coradini, Jakob Grasserbauer, Phillip Dumitraschkewitz, Thomas M Kremmer, and Stefan Pogatscher. A fast and implantation-free sample production method for large scale electron-transparent metallic samples destined for MEMS-based in situ S/TEM experiments. *Materials*, 14(5):1085, 2021.

[3] Diego Santa Rosa Coradini, Matheus Araujo Tunes, Patrick Willenshofer, Cameron Quick, Thomas Kremmer, Stefan Luidold, Peter J Uggowitzer, and Stefan Pogatscher. Unravelling nanometallurgy with in situ electron-microscopy: A case study with cu nanowires.

[4] Zhang HK., Long F., Yao Z., and . Daymond MR. Novel techniques of preparing Tem samples for characterization of irradiation damage. *Journal of Microscopy*, 252(3):251–257, 2013.

[5] Laure Bourgeois, Zezhong Zhang, Jiehua Li, and Nikhil V Medhekar. The bulk and interfacial structures of the η (Al_2Au) precipitate phase. *Acta Materialia*, 105:284–293, 2016.

[6] Phillip Dumitraschkewitz, Matheus A Tunes, Cameron R Quick, Diego Santa Rosa Coradini, Thomas M Kremmer, Parthiban Ramasamy, Peter J Uggowitzer, and Stefan Pogatscher. MEMS-based in situ electron-microscopy investigation of rapid solidification and heat treatment on eutectic Al-Cu. *Acta Materialia*, 239:118225, 2022.

Chapter 4

Degradation of Cu nanowires in a low-reactive plasma environment*

Author´s Contribution

Diego Santa Rosa Coradini - Conceptualization, Methodology, Investigation, Visualization, Writing the original draft.

Matheus A. Tunes - Investigation, Conceptualization, Methodology, Writing - Review and Editing.

Thomas Kremmer - Supervision, Investigation - Review and Editing.

Claudio G.Schön - Supervision, Investigation - Review and Editing.

Peter J. Uggowitzer - Supervision, Investigation, Methodology, Writing - Review and Editing.

Stefan Pogatscher - Project Administration, Supervision, Investigation, Writing - Review and Editing.

*Status: Chapter 4 is accepted for publication in the Journal nature material degradation, written by Diego S R Coradini, Matheus A. Tunes, Thomas M. Kremmer, Claudio G. Schön, Peter J. Uggowitzer, and Stefan Pogatscher.

Acknowledgments

Funding for this research was provided by the European Research Council (ERC) excellent science grant “TRANSDESIGN” through the Horizon 2020 programme under contract

757961 and by the financial support from the Austrian Research Promotion Agency (FFG) in the project 3DnanoAnalytics (FFG-No 858040). C.G.S. acknowledges the financial assistance of the Brazilian National Research, Development, and Innovation Council (CNPq) through the grant number 308565/2018-5. D.S.R.C. and M.A.T. would like to thank Mr. Matthias Honner for his support with the Cu NWs solution preparation and to Mr. Luigi Cattini for the support with electron-microscopy.

Abstract

The quest for miniaturisation of electronic devices is one of the backbones of industry 4.0 and nanomaterials are an envisaged solution capable of addressing these complex technological challenges. When subjected to synthesis and processing, nanomaterials must be able to hold pristine its initial designed properties, but occasionally, this may trigger degradation mechanisms that can impair their application by either destroying their initial morphology or deteriorating of mechanical and electrical properties. Degradation of nanomaterials under processing conditions using plasmas, ion implantation and high temperatures is up to date largely sub-notified in the literature. The degradation of single-crystal Cu nanowires when exposed to a plasma environment with residual active O is herein investigated and reported. It is shown that single-crystal Cu nanowires may degrade even in low-reactive plasma conditions by means of a vapour–solid–solid nucleation and growth mechanism.

4.1 Introduction

The advent of nanoscaled materials such as nanoparticles (NPs), nanotubes (NTs) and nanowires (NWs) has been subjected to intense research studies in the recent years given their reported electrical, mechanical and optical properties which differ from bulk materials mainly due to the large surface-to-volume ratio (SVR)[1, 15]. This set of properties explains the wide range of suggested applications that nanomaterials face nowadays in several areas of industry and science such as biomedical and electronics industries[2, 3, 4, 3].

A recent application of nanomaterials involves miniaturisation of electronic circuits and devices which has potential to revolutionise the electronics industry [5, 6, 7, 8, 9, 10], not only by extending the validity of Moore's law, but exceeding the scientific vision beyond it [11, 14, 15]. In this context, the search for reliable synthesis and processing routes for nanomaterials remains a significant challenge for academia and technology companies: for example, the ion-beam-induced processing doping of semiconductor nanowires was shown to severely degrade them via mechanisms known as ion-induced bending [16, 17]. Additional studies exploring degradation effects (from distinct and/or multiple sources operating synergistically) in nanomaterials are still largely required.

Despite the ongoing research and industrial interest on the semiconductor branch, metallic nanomaterials are also focusing the attention of the scientific community due to the recently reported superior properties when compared with their metallic bulk form [18]. Among the wide variety of metallic nanomaterials under investigation, Cu is commonly used in the microelectronics industry due to its suitable cost–benefit and appropriate mechanical and electrical properties [19]. As an example, in its oxide form, it has been discovered that Cu can be used as a one-dimensional nanostructure with envisaged applications in solar cells, gas and humidity sensors, high-temperature conductors and field emitter miniaturised transistors[2, 20, 21]. Many of these applications are related with its narrow band gap that varies from 1.2 to 2.1 eV (both CuO and Cu_2O are p-type semiconductors) at room temperature [2, 20, 21].

Nevertheless, the applicability of metallic nanomaterials like Cu NWs in nanocircuitry may be impaired when the thermodynamic stability of its (metallurgical) phase upon exposure to degradation environments is considered. The use of Cu can be limited by its susceptibility to oxidation at low temperatures [22], resulting in the formation of a

partial self-passivation layer as opposed to Al which reacts with O creating a more uniform and continuous self-passivation layer [19, 22, 23]. In addition, as observed in thin films, the reaction with monoatomic O and/or O_2-rich environments may induce the formation of oxides like CuO and Cu_2O which can degrade the initial electrical and mechanical properties of pure Cu [22].

An important requirement of microelectronics is the appropriate cleaning of materials and devices before and after their processing. The presence of carbonaceous impurities may destroy the component or reduce its initial designed functionality. A method frequently used by industry to carry out such cleaning is via the use of plasma which can remove superficial impurities by means of physical processes such as ablation, bombardment, physi- and/or chemisorption [19, 24, 12, 25]. Besides cleaning the surface of a material, plasma has been also used in inorganic nanostructure fabrication [26, 27, 28]. The latter fact is due to the distinct physicochemical properties of plasma such as the presence of several ionised chemical species that have a high reactivity with some metallic surfaces [2, 3, 28, 29, 30, 31]. For application in electron microscopy, for example, plasma cleaning devices are designed to neither induce heat nor sputtering of samples, but to remove the outermost layers of surface contamination (in a form of carbonaceous impurities and/or C–H-based weakly bonded contaminants)33. Notwithstanding, the presence of active species in a plasma environment can also lead to undesired degradation effects in nanomaterials, but to the best of our knowledge, there is a current lack of reports regarding the effects of reactive plasma exposure in Cu NWs.

Although the low- or high-reactive plasma degradation of NWs is largely sub-notified in the literature, several authors reported degradation effects of plasma on metallic thin films. Gibson et al.[5] observed the effects of a simulated plasma environment (similarly to that found in low earth orbit) on a Cu thin films by analysing interaction of monoatomic O with their surfaces. In the study, the authors observed that the Cu thin films (Cu_2O) had a higher reactivity with monoatomic O than with molecular O (i.e. O_2), even in low-pressure conditions (0.0013 mbar)[5]. This was similarly investigated by Kennedy and Friesen [7] whose concluded that the growth of Cu films via sputtering processes can be affected by the O partial pressure and that the presence of a low-content O atmosphere can lead to adsorption, which upon segregation at the surface may initiate oxide layer growth.

The effects of plasma exposure in nanomaterials has been recently reviewed by Ostrikov et al.[29] who also were pioneers to investigate the degradation effects of a high-reactive (O-rich) plasma environment on metallic substrates in promoting nucleation and growth of different types of metal oxide NWs. In this context, two distinct physicochemical mechanisms were identified: the solid–liquid–solid (SLS) and vapour–solid–solid (VSS)[29] mechanisms. SLS mechanism is observed for metallic substrates with low melting point and it consists on the melting of a nanoregion caused by the reaction of the metal with the monatomic O present in the plasma. VSS mechanism is observed for metals with higher melting point, such as Fe for example. The melting of a nanoregion may also occur in the VSS, but the direct adsorption of a gas-phase into the molten-metal nanoregion (or activated nanoregion) and the higher temperatures involved with these processes can catalyse recrystallisation and growth of an oxide solid phase at the liquid–solid interface [29].

In the present study, the effects of low-reactive plasma exposure on Cu NWs will be reported. The NWs were characterised within a scanning/transmission electron microscope (S/TEM) before and after the plasma exposure. The low-reactive plasma is mainly composed of Ar ions with residual gases—such as O which was not intentionally added—and the initial objective was to clean the Cu NWs before electron microscopy. However, the exposure to such plasma environment revealed an unexpected degradation of the Cu NWs, which was the main motivation for the investigations that will be reported in this study. The characterisation of this degradation effect was carried out by the detailed use of electron-microscopy techniques such as high-angle annular dark field (HAADF), energy-dispersive X-ray (EDX) spectroscopy mapping and also via conventional TEM techniques such as selected-area electron diffraction (SAED).

4.2 Methods

The experimental methodology used to characterise the degradation effects of low-reactive plasma exposure on single-crystal Cu NWs will be detailed and described in this section.

4.2.1 Sample preparation

Single-crystal Cu NWs in a form of powder was received from Sigma Aldrich. The total mass of Cu NWs was 250 mg and the batch number is MKCL4542. The preparation of a liquid solution was necessary to disperse the NWs. The solution used in this work was made with 8 mg of Cu NWs for 6.8 g of isopropanol. Ultrasonic mixing was used for 30 min before the TEM sample preparation in order to unclutter the Cu NWs in solution. This type of sample preparation for nanomaterials has been described elsewhere [57, 56].

After ultrasonic mixing, the Cu NWs in solution were pipetted directly onto metallic substrates and left to dry in air. These metallic substrates consisted of 3 mm electro-polished TEM disks. For the experiments reported in this work, different metallic substrates were used, and the results reported here were reproduced using three different substrates (Sn, Al and steel AISI347).

4.2.2 Low-reactive plasma exposure experiments

Plasma exposure was carried out using the plasma cleaning device model FEMTO with a 2.8 L chamber from Diener. The generator was operating at 60% of maximum power which corresponds to 100 W. The frequency of the generator was 40 kHz. The chamber was pumped (pre-purge) to a pressure of 0.2 mbar. At this condition, as a matter of comparison, a quick calculation considering the air as an ideal gas and 1 L of volume (for simplification) shows that at this pressure level, the O_2 concentration is around 414 ppm. Then Ar gas was purged until the pressure stabilised at 0.3 mbar. The used Ar gas was 99.999% pure; therefore, the generated plasma is herein defined as low-reactive plasma, i.e., a low-content of reactive species may be present, but not intentionally added, due to the vacuum conditions. It is worth emphasising that a pressure level of 0.3 mbar corresponds to the category of medium vacuum, often referred in the literature as not high enough to mitigate the influence of active species such as O [57]. Therefore, given the residual concentration of monoatomic active species such as O, the term “low-reactive plasma” has been adopted throughout this work. For the experiments reported in this work, plasma exposure was carried out in function of two time lengths: 10 and 25 min.

4.2.3 Electron-microscopy characterisation

For these experiments, a ThermoFisher ScientificTM Talos F200X G2 electron microscope was used. The TEM operated a field-emission gun at 200 kV and it is equipped with Super-X EDX detectors. Before plasma exposure, a TEM pre-characterization was carried out in the pristine Cu NWs onto metallic 3 mm disks. The edges of the 3 mm disks were used as landmarks to pinpoint specific Cu NWs. After plasma exposure, some Cu NWs were not found in their landmarked areas, most likely because they were washed away during plasma exposure. The pre and post-plasma exposure TEM characterisation under identical conditions—consisted of BFTEM, HAADF and STEM-EDX mapping. SAED patterns using a 660 mm camera length were also recorded to monitor the crystallinity of the NWs. The EDX maps presented in this work were processed in the ThermoFisher Velox software (version 2.9) and represent the net intensities of Cu and O. Elemental quantification was carried out within Velox using the Schreiber-Wims ionisation cross-section model and a multi-polynomial (parabolic) fit function for the EDX spectra. The radius of each quantified NW was measured a priori and this value was used for absorption correction purposes along with a density of 9.0 g.cm^{-}3. As the standardless error for elemental composition is around 20% of the value (from the manufacturer [13]), a set of three different areas were measured for all the quantified NWs reported in this work in order to confirm the estimated compositions within a standard deviation $\leq$5%.

4.3 Results

4.3.1 Morphology of the pristine Cu NWs

The pre-plasma exposure electron-microscopy characterisation of the Cu NWs is shown in Figure 4.1. This Cu NWs condition is herein referred as pristine. SAED pattern and bright-field TEM (BFTEM)analysis, shown in Figure 4.1b, c, respectively, revealed that the CuNWs are initially single-crystalline and nanoroughness (known as“hillocks” in the literature [29]) is noticeable on the surface of the CuNWs. The superficial inhomogeneities observed on the Cu NWs in BFTEM were also previously reported as partial passivation layer [23, 24]. Insets in Figure 4.11d–f show micrographs from the STEM analysis including HAADF, Cu and O EDX mapping measurements, respectively.

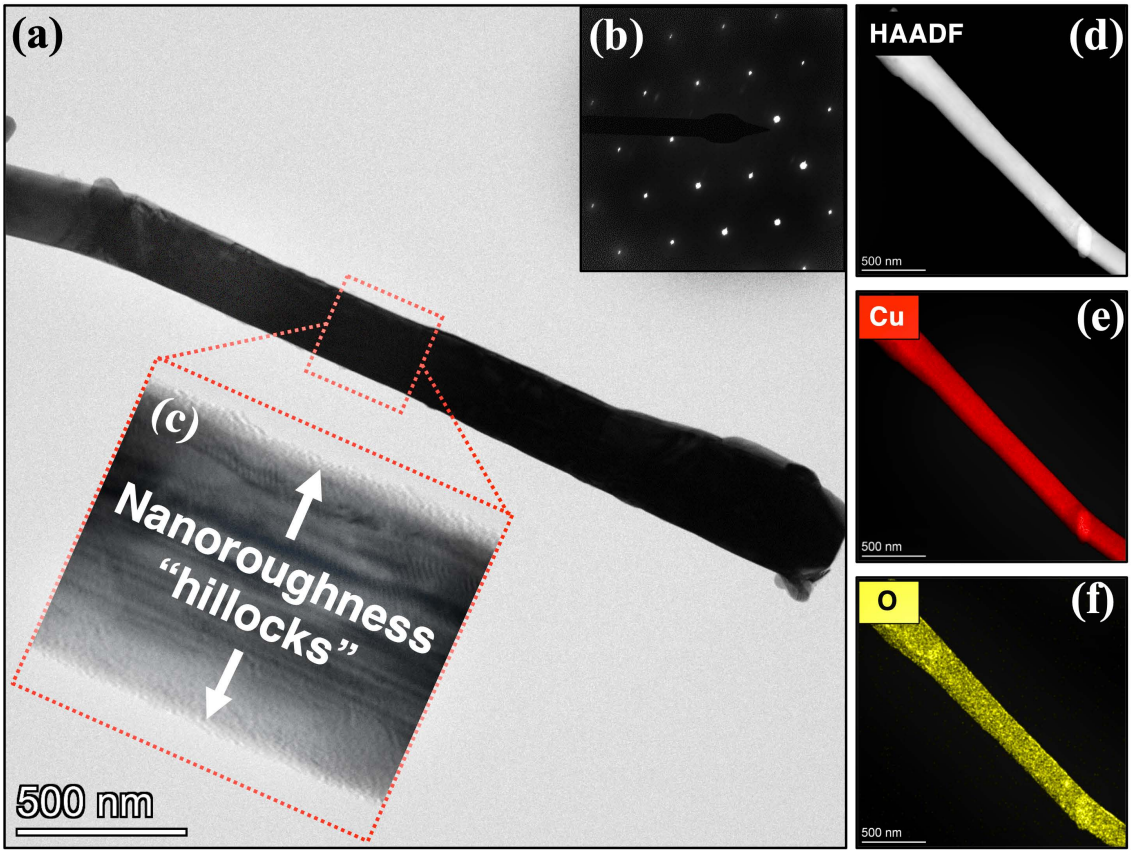

Figure 4.1: Pre-plasma exposure electron-microscopy characterisation of a Cu NWs. a BFTEM micrograph of a Cu NW along a zone axis including b the SAED pattern confirming the single-crystallinity of the NWs. The BFTEM micrograph in c shows inhomogeneities often observed in the surface of the Cu NWs. The STEM analysis ind–f show the Cu NWs viewed with the HAADF detector and the Cu andO elemental maps, respectively.

4.3.2 Morphology of Cu NWs after exposure to a low-reactive plasma

Typical morphologies of the Cu NWs after exposure to the low-reactive plasma environment as a function of time are shown in Figure 4.2. The set of STEM micrographs, EDX maps and the SAED pattern presented in Figure 4.2a shows the electron-microscopy characterisation of a typical Cu NW after 10 min of plasma exposure while the set of micrographs in Figure 4.2b shows two CuNWs after 25 min of exposure. From the analysis presented in Figure 4.2, two major experimental observations can be pointed out so far: (i) the Cu NWs—initially single-crystals—have altered their crystal structure as per exposure to the low-reactive plasma and (ii) the modification of their crystal structure is followed by the formation of small rounded-shape nuclei as can be observed in detail with brighter

contrast in the HAADF micrographs. These nuclei will be hereafter referred to either nanoclusters (NCs) or nuclei. It is important to emphasise that such low-reactive plasma effect was not observed to occur on the different metallic substrates (TEM lamellae) used in this work; therefore, this phenomenon was restricted to the Cu NWs.

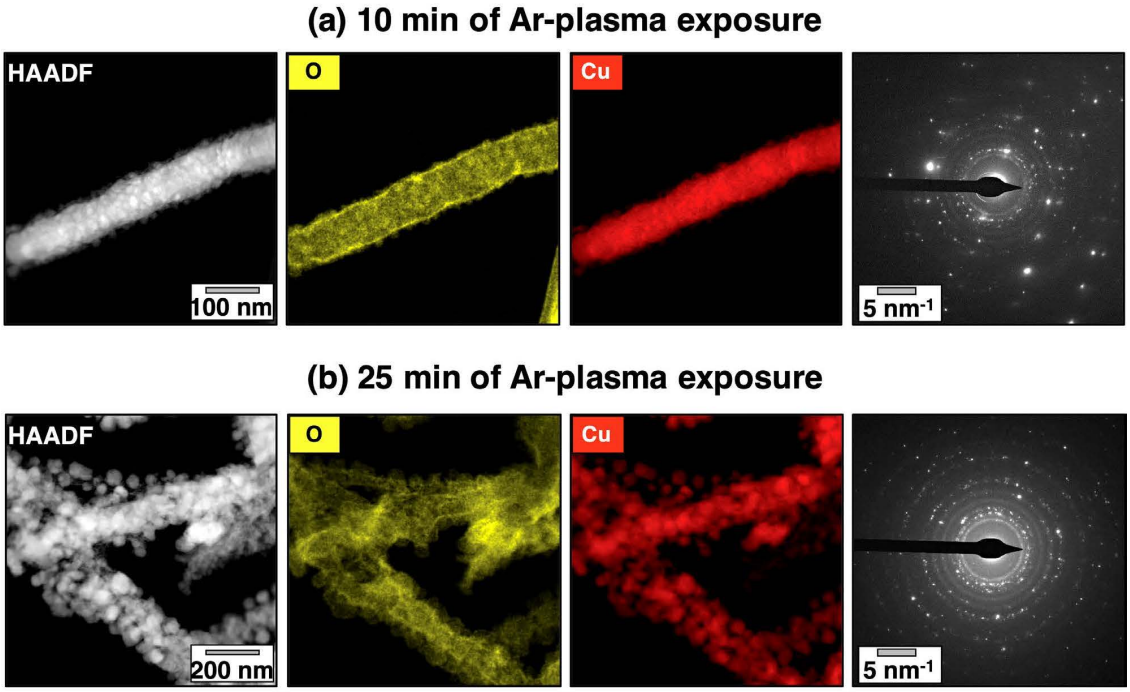

Figure 4.2: Analytical electron-microscopy characterisation of the Cu NWs.After a 10 and b 25 min of low-reactive plasma exposure with their respective SAED patterns. Upon exposure to a low-reactive plasma, the initial single-crystal Cu NWs are observed to degrade to randomly oriented NCs as indicated by the SAED polycrystalline patterns in a and b.

4.3.3 Analysis of pristine and plasma-exposed Cu NWs

With the EDX analysis, an elemental quantification of both Cu and O as a function of the low-reactive plasma exposure time was carried out. Figure 4.3 shows a plot where the atomic concentration of O was observed to increase with the plasma exposure time and a trend towards the expected composition of Cu_2O was detected. The pristine Cu NW has a passivation layer circumventing its core as shown in the overlapped O and Cu maps in Figure 4.3. By measuring the radius difference between O and the Cu in the pristine condition, the value was estimated to be 14.1±1.3 nm. The overlapped O and Cu maps for the 10 and 25 min plasma-exposed Cu NWs also show the association of O both with the formed NCs and the degraded NW core.

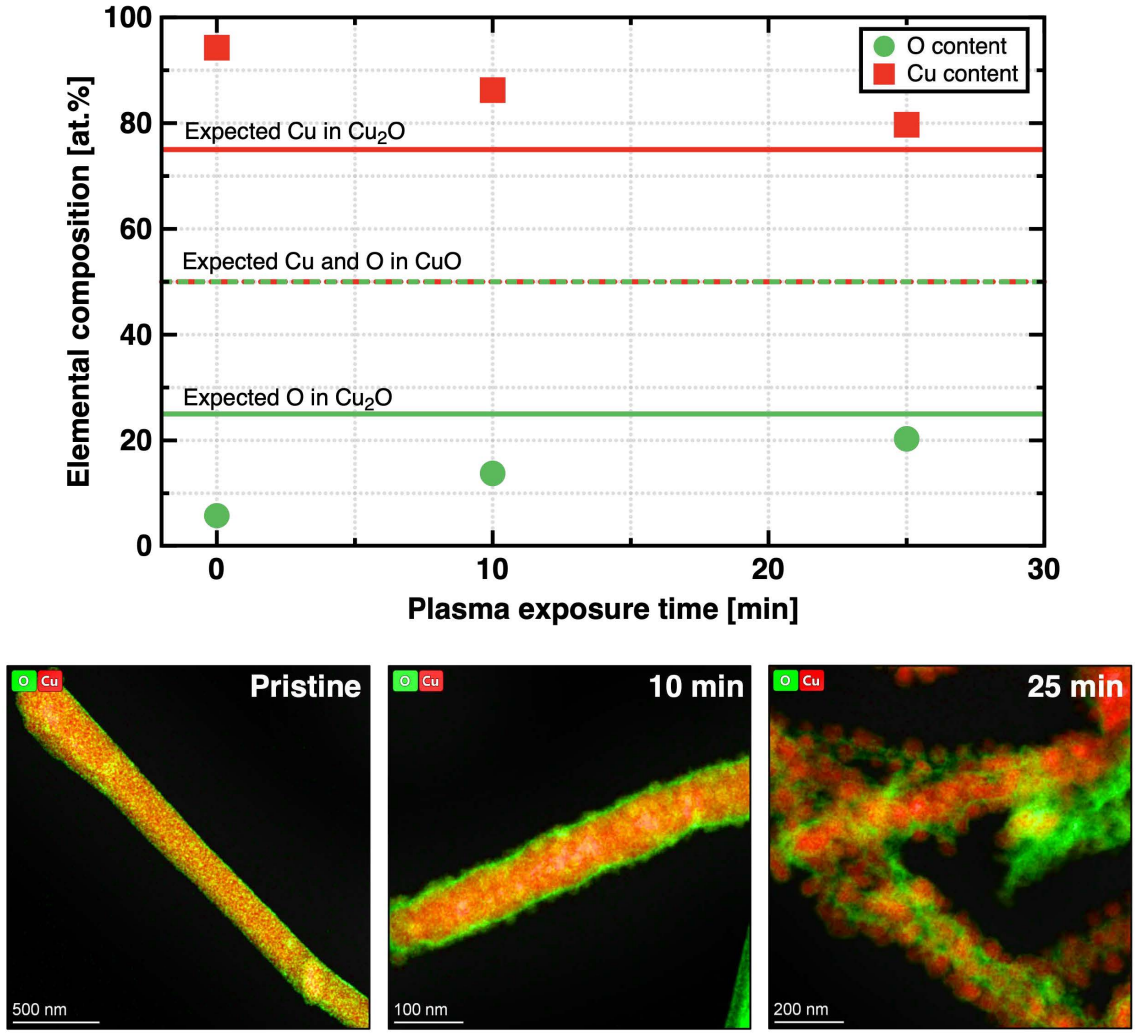

Figure 4.3: Analytical characterisation of the Cu NWs plasma exposure degradation.The elemental composition of the Cu NWs before and after exposure to the low-reactive plasma is shown in plot a. The overlapped O and Cu elemental maps are shown for b pristine,c 10 and d 25 min plasma-exposed Cu NWs. As the O content was observed to increase as a function of the plasma exposure time, a trend towards the expected Cu_2O composition was noted.

4.3.4 Formation of rounded-shape NCs

The formation of rounded-shape NCs from the Cu NWs can be better assessed when looking at the surface of the metallic substrates after the plasma exposure. Figure 4.4a shows a Cu NWs above a pure Al substrate after 10 min of low-reactive plasma exposure. NCs are observed both at the surfaces of the NWs and as-deposited on the pure Al substrate. The latter case occurs when the nuclei are formed at the surface of the Cu NWs and then deposits onto the substrate during plasma exposure. Figure 4.4 shows an NCs size distribution estimated using the Cu EDX map presented in Figure 4.4d: the histogram of NCs radii resembles abi-modal distribution.The O map from the area shown

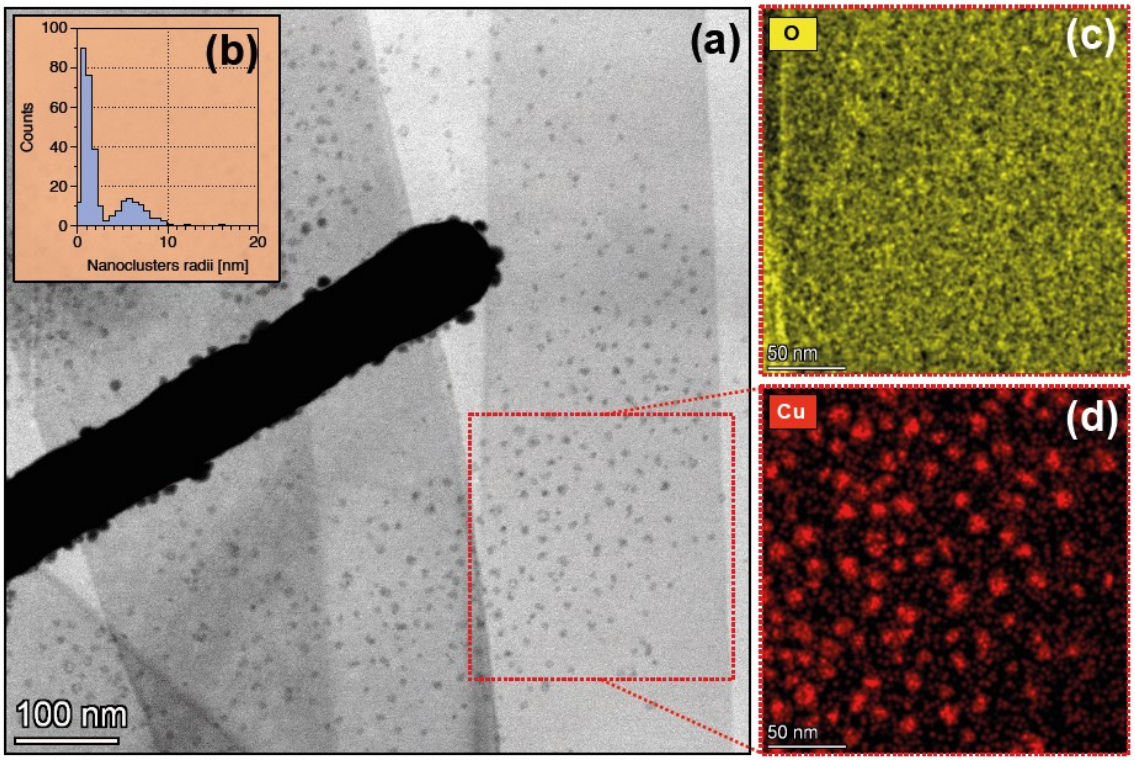

Figure 4.4: Formation of rounded-shape nanoclusters.Electron-microscopy characterisation of the Cu-rich nanoclusters formed after 10 min of low-reactive plasma exposure:a BFTEM micrograph a Cu NWs above the pure Al substrate where some NCs are observed deposited onto it,and b NCs size distribution from the NCs present in the red dashed-square area. The EDX maps of O and Cu are shown in c and d, respectively,and they correspond to the red dashed-square area in a.

as a red dashed-square in Figure 4.4a revealed no significant enrichment of this element around the formed NCs. The absence of O-enrichment is also noticeable in the EDX maps presented in Figure 4.2a, b.

4.3.5 SAED pattern indexing

SAED pattern indexing was carried out with the electron-diffraction pattern recorded from a Cu NWs after 25 min of low-reactive plasma exposure as shown in the plot in Figure 4.5. This SAED pattern resembles to a polycrystalline material which is consistent with the formation of NCs. Crystallographic reference data from both Cu and Cu oxide phases (CuO and Cu_2O only) were used [32, 33, 34]. The indexing was performed by measuring the radii of the Debye–Scherrer rings with respect to the transmitted beam. In order to improve the accuracy in measuring the rings radii (with an estimated error of 5%), the customised ImageJ script"radial profile extended" was used and the detected diffraction peaks were overlapped with the SAED pattern in Fig.4.5. These measured radii corre-

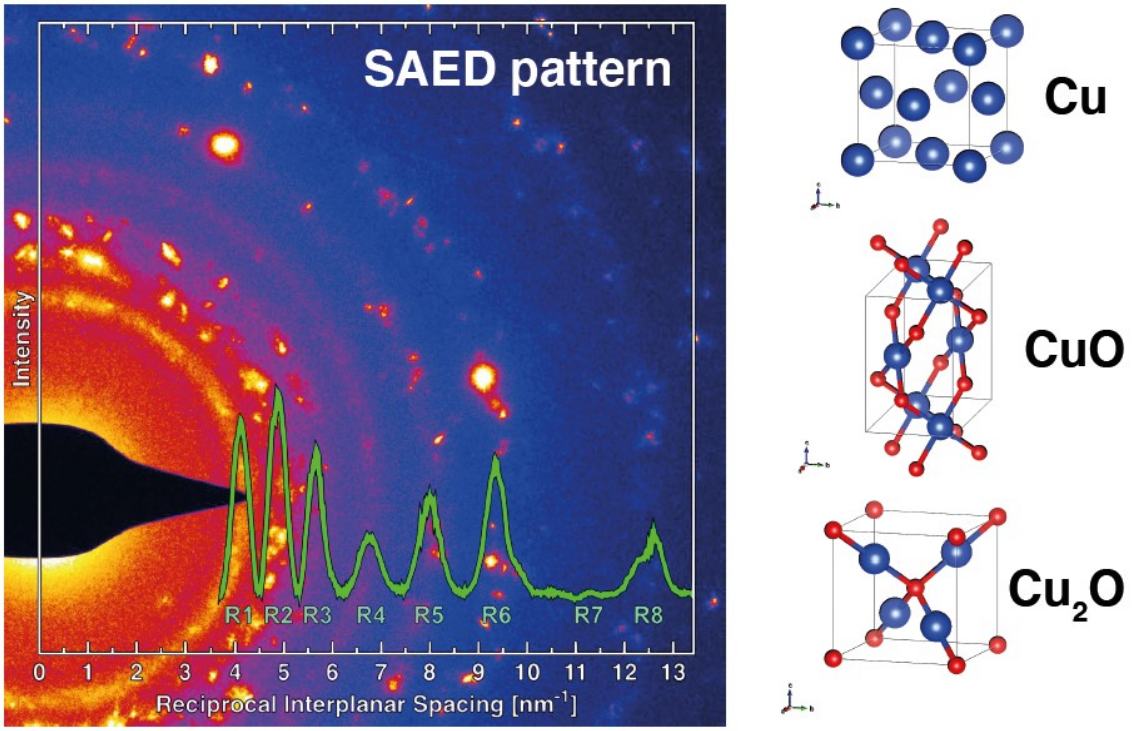

Figure 4.5: Crystallographic identification of possible Cu oxide phases.a SAED pattern indexing using a typical electron-diffraction pattern from a Cu NW after 25 min of low-reactive plasma exposure. The diffraction peaks overlapping the SAED pattern were obtained with radial profile extended analysis within the ImageJ software. The crystallographic models for b Cu,c CuO and d Cu_2O were generated based on crystallographic database data available in the literature [32, 33, 34]

spond to the reciprocal interplanar spacing of the potential phases present in the material syste mafter plasma exposure. Table 1 shows experimental and crystallographic database reference values. In some cases, an overlapping between the experimental and reference interplanar spacing data from multiple phases was noticeable. By this, the following criterium was used to perform the SAED pattern indexing: (i) numerical value matching; prioritisation of planes with (ii) lower indexes and (iii) higher diffraction intensities. Using this criterium, both Cu and Cu_2O phase were indexed with higher probability of occurrence than the CuO phase.

4.4 Discussion

Comparing the STEM micrographs in Figure 4.1 a and Figure 4.2 a, b, it is possible to conclude that a significant morphological change of the Cu NWs has occurred as a result of low-reactive plasma exposure. Such changes are that the initial single-crystal Cu NWs

Experimental data			Crystallographic database values		
Peak Indext	d[A]	Error	Cu[33]	CuO[34]	Cu_2O[35]
			d [A] and reflection planes		
R1	2.43	0.12	-	-	-
R2	2.05	0.10	2.087 (1 1 1)a	-	2.134 (0 0 2)
R3	1.76	0.09	1.808 (0 0 2)a	1.797 (1 1 2)	1.743 (1 1 2)
R4	1.48	0.07	-	1.515 (1 1 -3)	1.509 (0 2 2)a
R5	1.25	0.06	-	1.261 (2 2 -2)a	1.232 (2 2 2)
R6	1.07	0.05	1.090 (1 1 3)a	1.079 (1 3 1)	1.067 (0 0 4)
R7	0.89	0.04	0.904 (0 0 4)	0.899 (2 2 4)	0.871 (2 2 4)a
R8	0.79	0.04	0.808 (0 2 4)a	0.798 (4 0 4)	0.793 (2 3 4)

Note: The crystallographic database values marked with a are satisfying the indexing criterium adopted in this work

became polycrystalline upon plasma exposure and this degradation effect manifests as a function of the low-reactive plasma exposure time: the higher the exposure time, the more nanocrystals are formed, leading to a complete degradation of the Cu NWs core. Remarkably, using the HAADF detector, it was possible to confirm that the formation of such NCs is driven by a phenomenon occurring at the surface of the Cu NWs. This is reflected by the experimental detection of NCs formation at the surface of a Cu NW after 10 min of low-reactive plasma exposure as shown in the HAADF micrograph in Figure 4.2 a.

It is worth emphasising that although the plasma degradation of metallic thin films and nanomaterials have been already reported under high-reactive plasma exposure [29, 35], the results herein reported and the detailed characterisation presented clearly indicate that severe degradation can occur—in the case of single-crystal Cu NWs—even in low-reactive plasma environments.

The degradation of the single-crystal Cu NWs can be empirically interpreted via the electron-beam-induced contrast mechanisms of the HAADF micrographs [58, 36, 37] obtained during the characterisation before and after low-reactive plasma exposure. When imaged with the HAADF detector and along a specific zone axis, the initial single-crystal structure of the Cu NWs is of a complete uniform bright contrast as can be noted in

Figure 4.1 d. But after 10 min of low-reactive plasma exposure—the micrograph in Figure 4.2a—the HAADF contrast is strongly changed when compared with the pristine Cu NW in Figure 4.1 d: this contrast alteration is due to the presence of the randomly oriented NCs at the surface of the plasma-exposed Cu NW. Due to a combination of the HAADF signals emerging from both NCs and NW, at the surface of the latter, the NCs are of brighter contrast. By this, both shape and size of NCs are revealed.

These superficial NCs were further characterised in Figure 4.4 where it was observed that they can form at the surface of the Cu NW and then deposit onto a substrate directly beneath the Cu NW. By using the EDX signal from Cu, the sizes of such NCs were estimated to have a bi-modal distribution which has been already associated with characteristic nucleation and growth mechanisms described in the literature [10, 38].

The hypothesis of surficial degradation triggered by the low-reactive plasma exposure was investigated in-depth via SAED pattern indexing. The EDX measurements presented in Figures 4.1e, f, 4.2a, b as well as the overlapped O and Cu maps in Figure 4.3 suggest the presence of O at the NW before and after plasma exposure. As mentioned in the results section, the presence of O before plasma exposure is probably associated with a partial passivation layer at the Cu NW surface as metals (at low temperatures) do not dissolve O atoms in solid solution. Using the Cu and O maps, this passivation layer was estimated to have a thickness of around 14.1 $\pm$ 1.3 nm. The presence of O within the NW–NCs system persists after low-reactive plasma exposure, which motivated the use of the Cu, CuO and Cu_2O crystallographic data to index the polycrystalline rings in Figure 4.5. Giving the limits of detection, the presence of either CuO or Cu_2O cannot be ruled out by the SAED indexing analysis, but this creates an apparent contradiction with the facts that neither O does not show a significant enrichment around the NCs in the EDX maps of the Fig. 4.2a, b nor the estimated atomic composition after plasma exposure matches with the CuO or Cu_2O oxide phases, although a trend has been detected towards the elemental composition of the latter.

The formation of Cu-rich oxide NCs after low-reactive plasma exposure can be better understood by analysing the reported thermodynamic data on the Cu–O system and its phase diagrams [39, 40, 41, 42]. It is established that at the nanoscale [43, 44], conventional thermodynamics does not necessarily correlate nanomaterials with bulk materials [45, 46] due to the large surface-to-volume ratio and the prevalence of surface tension effects [47];

however, these Cu–O phase diagrams are herein used for shedding light on the discussion of the obtained results.

In the Cu–O phase diagrams reported in the literature, for the regime of very low O partial pressures, the formation of oxide phases such as Cu_2O is already thermodynamic favoured. Naturally, upon a reduction of such O partial pressure after purging and plasma generation, the oxide phases can form in non-stoichiometric conditions (i.e. metal rich) given the favourable thermodynamic conditions [40, 48]. It is worth of emphasising that in the plasma chamber, the pressure before Ar gas purging was measured to be around 0.2 and 0.3 mbar after purge. Although no O was intentionally added into the chamber, it is reasonable to assume some O will be present as impurity in the chamber in low O partial pressure, which allows oxide formation off the ideal stoichiometry. In summary, the exposure to a low-reactive plasma induce the formation of small non-stoichiometric NCs of Cu-rich oxide phases, but a reasonable physical mechanism for explaining this phenomenon is still required.

A first hypothesis to shed light on the degradation mechanism observed to occur in pristine Cu NWs is the possibility of Ar ion bombardment within the plasma chamber. The plasma chamber in our work is not equipped with a device to intentionally accelerate Ar ions in a limited set of directions (i.e. it does not generate an Ar ion beam). Under the conditions herein studied, the literature reports that the kinetic energy of Ar ions within a plasma under a pressure of approximately 0.3 mbar is of around 5 eV [49]; however, the sputtering yield of Cu by Ar ions in this energy range is close to zero [50, 51, 59]. To confirm this, additional experiments of Ar ion bombardment of pristine Cu NWs were performed in this work and are shown in the Supplementary Information file: the results of these experiments demonstrate that Ar ion bombardment itself is not capable of explaining the observed Cu NWs degradation when exposed to a low-reactive plasma.

The mechanism of Cu NW degradation under low-reactive plasma exposure can be better understood using existing models that were recently studied and reviewed by Ostrikov et al. [29] regarding the synthesis of metal oxide NWs under exposure to a high-reactive plasma. It has been reported that when an elemental metallic substrate is subjected to a high-reactive plasma (i.e. O-rich plasma), its surface undergoes localised molten nano-regions which can promote the heterogeneous nucleation and growth of metal oxide NWs upon adsorption of O atoms. These nucleation and growth mechanisms—known as SLS

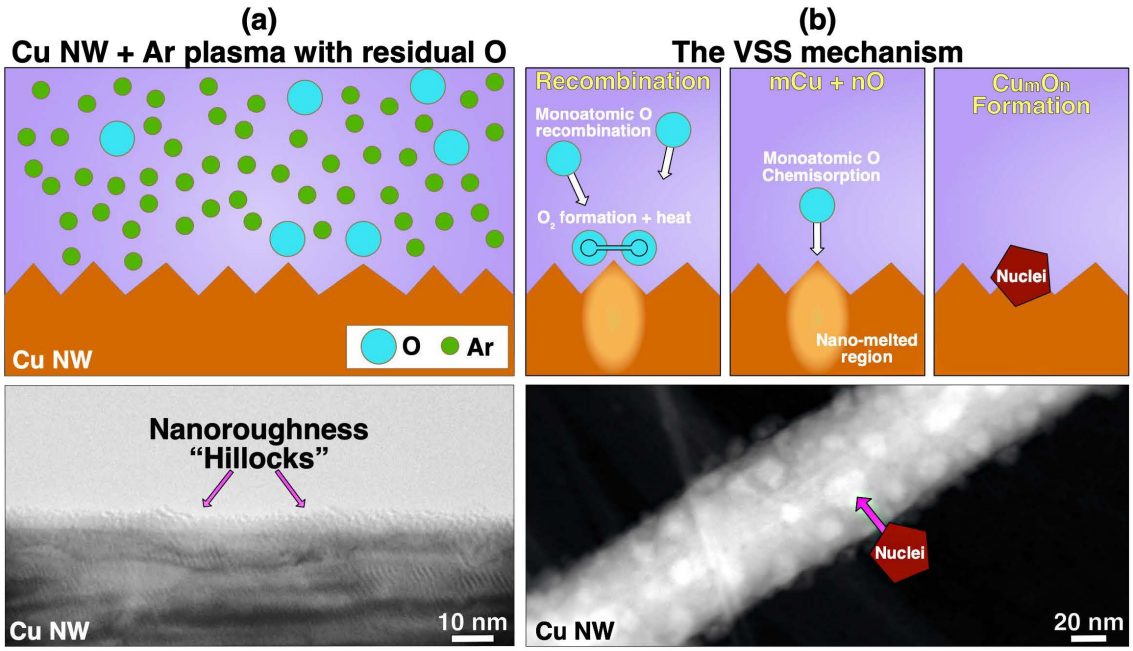

Figure 4.6: Proposed sequence for the observed Cu NWs degradation in a low-reactive plasma.An adaptation of the VSS mechanism as a hypothesis to explain the surface-driven degradation of single-crystal Cu NWs. The scheme in a shows an initial stage where the plasma is generated and co-exist with the Cu NW; the BFTEM micrograph shows that the Cu NWs used in this work always present nanoroughness at their surfaces. The schemes in b show the subsequent stages of monoatomic O recombination, O adsorption and nuclei formation; the micrograph shows that these nuclei are detected using the HAADF detector.

and VSS—were already discussed in the introduction.

In contrast to the SLS, the VSS mechanism is responsible for surface degradation of metals with a high melting point, as here for Cu NWs. This model can be adapted to the results reported in this present work on the exposure of single-crystal Cu NWs to a low-reactive plasma. The diagram pictured in Figure 5.6 further elaborates this core idea.

In Figure 4.6a, the surface of a Cu NW is represented with roughness (or "hillocks") at the nanoscale, in contact with Argon atoms, along with a residual content of O atoms, thus setting up a low-reactive plasma. The BFTEM micrograph presented in Figure 4.6a shows that such nanoroughness is recurrent feature observed in the Cu NWs investigated in this study.

A hypothetical process to explain the low-reactive plasma induced degradation of Cu NWs is exhibited in the scheme presented in Figure 4.6b. The presence of monoatomic O atoms within the plasma suggests that a recombination reaction between two O atoms at a hillock site on the Cu NW's surface is possible and likely to occur. Such O recombination reaction is highly exothermic [29]; thus, the energy generated can be absorbed at a hillock

site and it is sufficient to raise the temperature in a nanoregion. Due to the rapidly increase in the local temperature, monoatomic O chemisorption can occur, which leads to an incorporation of O in the Cu nano-melted region. It should be noted that nanomaterials have a lower melting point than their counterparts [52, 53, 54] and that low-energy Ar ion collisions (on average ±5 eV52 for the plasma conditions in this thesis) are able to promote Cu surface diffusion [55]. Both characteristics may facilitate the proposed degradation process. Upon O adsorption, non-stoichiometric Cu oxide nuclei are allowed to form upon cooling. These are the nuclei which are observed as NCs in the HAADF micrographs at the surface of the Cu NWs after plasma exposure. Because of their short-term melting and phase transformation, the compatibility of the nuclei with the NW is greatly reduced, so that they can fall off and the described process takes place repeatedly on the Cu NW surface.

A major distinction between the degradation model herein proposed and the metal oxide nucleation and growth model proposed by Ostrikov et al.[29] must be made. In the latter, after nuclei formation and given the high O content in the plasma (i.e. more recombination reactions implying in a higher temperature), a complete metal oxide NW is allowed to grow upon O adsorption. In the former case, given the lower O content, only nuclei are formed, and its crystallised phase is Cu-rich and O-poor.

As experimentally demonstrated in this work, the continuous formation of non-stoichiometric Cu oxide NCs upon exposure of single-crystal Cu NWs to a low-reactive plasma leads to a complete degradation of the NWs core via the destruction of the initial single-crystal structure and characteristic morphology. In contrast to previous works, the present research shows such degradation is able to occur in plasma environments with a low content of O.

A model based on the VSS mechanism has been proposed to explain the observed degradation results. This model assumes that the surface of the initial Cu NWs has nanoroughness (confirmed by electron-microscopy characterisation) which are preferential sites where monoatomic O recombination exothermic reactions are allowed to take place, releasing enough energy to induce local melting of a nanoregion, favouring the formation of such non-stoichiometric Cu oxide NCs upon O consumption via chemisorption.

Although the phenomenon herein observed to occur is referred as degradation of Cu NWs, the results show that this may be an alternative approach for the synthesis of Cu

oxide NCs when compared with the existing magnetron-sputtering methods.

Further research is needed to understand the mechanism of non-stoichiometric Cu oxide formation at low pressures as well as more accurate techniques to detect low content of O in the nanometre-sized nuclei. The question whether only metallic Cu NWs are subjected to such observed low-reactive plasma degradation needs further clarification.

4.5 Reference

[1] Xiaofang Wang, Fuli Zhao, Pingbo Xie, Shaozhi Deng, Ningsheng Xu, and Hezhou Wang. Surface emission characteristics of Zno nanoparticles. *Chemical physics letters*, 423(4-6):361–365, 2006.

[2] Cheng-Liang Hsu, Jia-Yu Tsai, and Ting-Jen Hsueh. Novel field emission structure of Cuo/Cu_2o composite nanowires based on copper through silicon via technology. *RSC Advances*, 5(43):33762–33766, 2015.

[3] Chaudhery Mustansar Hussain. *Handbook of nanomaterials for industrial applications*. Elsevier, 2018.

[4] Shiv Shankar and Jong-Whan Rhim. Facile approach for large-scale production of metal and metal oxide nanoparticles and preparation of antibacterial cotton pads. *Carbohydrate Polymers*, 163:137–145, 2017.

[5] BC Gibson, JR Williams, AT Fromhold Jr, MJ Bozack, WC Neely, and Ann F Whitaker. The interaction of atomic oxygen with thin copper films. *The Journal of chemical physics*, 96(3):2318–2323, 1992.

[6] Robert Chau, Suman Datta, and Amlan Majumdar. Opportunities and challenges of III-V nanoelectronics for future high-speed, low-power logic applications. In *IEEE Compound Semiconductor Integrated Circuit Symposium, 2005. CSIC'05.*, pages 4–pp. IEEE, 2005.

[7] JK Kennedy and Cody Friesen. The effect of oxygen adsorption on Cu {111} thin film growth stresses. *Journal of Applied Physics*, 101(5):054904, 2007.

[8] Qingzhou Cui, Fan Gao, Subhadeep Mukherjee, and Zhiyong Gu. Joining and interconnect formation of nanowires and carbon nanotubes for nanoelectronics and nanosystems. *Small*, 5(11):1246–1257, 2009.

[9] Donglai Yao, Gang Zhang, and Baowen Li. A universal expression of band gap for silicon nanowires of different cross-section geometries. *Nano letters*, 8(12):4557–4561, 2008.

[10] Mark A Koten, SA Voeller, MM Patterson, and Jeffrey E Shield. In situ measurements of plasma properties during gas-condensation of Cu nanoparticles. *Journal of Applied Physics*, 119(11):114306, 2016.

[11] Peter Sutter. How silicon leaves the scene. *Nature materials*, 8(3):171–172, 2009.

[12] B Kegel and H Schmid. Low-pressure plasma cleaning of metallic surfaces on industrial scale. *Surface and Coatings Technology*, 112(1-3):63–66, 1999.

[13] JW Arblaster. Thermodynamic properties of copper. *Journal of Phase Equilibria and Diffusion*, 36(5):422–444, 2015.

[14] Jung Han Choi and Krzysztof Iniewski. *High-speed and Lower Power Technologies: Electronics and Photonics*. CRC Press, 2018.

[15] Rong Chen, Yi-Cheng Li, Jia-Ming Cai, Kun Cao, et al. Atomic level deposition to extend Moore's law and beyond. *International Journal of Extreme Manufacturing*, 2(2):022002, 2020.

[16] Imran Hanif, Osmane Camara, Matheus A Tunes, Robert W Harrison, Graeme Greaves, Stephen E Donnelly, and Jonathan A Hinks. Ion-beam-induced bending of semiconductor nanowires. *Nanotechnology*, 29(33):335701, 2018.

[17] Diego R Gomes, Anatoliy A Turkin, David I Vainchtein, and Jeff Th M De Hosson. On the fabrication of micro-and nano-sized objects: The role of interstitial clusters. *Journal of materials science*, 53(10):7822–7833, 2018.

[18] Ovid'Ko IA., Valiev RZ., and Zhu YT. Review on superior strength and enhanced ductility of metallic nanomaterials. *Progress in materials science*, 94:462–540, 2018.

[19] Daniel Chir and Raymond Yeo. Plasma process considerations for copper wire bonding. In *2012 35th IEEE/CPMT International Electronics Manufacturing Technology Conference (IEMT)*, pages 1–3. IEEE, 2012.

[20] Jaewon Jang, Seungjun Chung, Hongki Kang, and Vivek Subramanian. P-type Cuo and Cu_2o transistors derived from a sol–gel copper (II) acetate monohydrate precursor. *Thin Solid Films*, 600:157–161, 2016.

[21] BP Rai. Cu_2o solar cells: A review. *Solar cells*, 25(3):265–272, 1988.

[22] Jian Li, JW Mayer, and EG Colgan. Oxidation and protection in copper and copper alloy thin films. *Journal of applied physics*, 70(5):2820–2827, 1991.

[23] Ranran Wang, Haitao Zhai, Tao Wang, Xiao Wang, Yin Cheng, Liangjing Shi, and Jing Sun. Plasma-induced nanowelding of a copper nanowire network and its application in transparent electrodes and stretchable conductors. *Nano Research*, 9(7):2138–2148, 2016.

[24] Hsieh JH., Fong LH., Yi S., and Metha G. Plasma cleaning of copper leadframe with Ar and Ar/H_2 gases. *Surface and Coatings Technology*, 112(1-3):245–249, 1999.

[25] Fangyu Wu, Galit Levitin, and Dennis W Hess. Low-temperature etching of cu by hydrogen-based plasmas. *ACS Applied Materials & Interfaces*, 2(8):2175–2179, 2010.

[26] Alberto Gasparotto, Davide Barreca, Daniela Bekermann, Anjana Devi, Roland A Fischer, Chiara Maccato, and Eugenio Tondello. Plasma processing of nanomaterials: Emerging technologies for sensing and energy applications. *Journal of Nanoscience and Nanotechnology*, 11(9):8206–8213, 2011.

[27] Liangliang Lin and Qi Wang. Microplasma: A new generation of technology for functional nanomaterial synthesis. *Plasma Chemistry and Plasma Processing*, 35(6):925–962, 2015.

[28] Jie Zheng, Rong Yang, Lei Xie, Jianglan Qu, Yang Liu, and Xingguo Li. Plasma-assisted approaches in inorganic nanostructure fabrication. *Advanced Materials*, 22(13):1451–1473, 2010.

[29] Kostya Ken Ostrikov, Igor Levchenko, Uros Cvelbar, Mahendra Sunkara, and Miran Mozetic. From nucleation to nanowires: A single-step process in reactive plasmas. *Nanoscale*, 2(10):2012–2027, 2010.

[30] Meyyappan M. A review of plasma enhanced chemical vapour deposition of carbon nanotubes. *Journal of Physics D: Applied Physics*, 42(21):213001, 2009.

[31] Saif Islam M., Sharma S., Kamins TI., and Stanley Williams R. A novel interconnection technique for manufacturing nanowire devices. *Applied physics A*, 80(6):1133–1140, 2005.

[32] Catherine F Smura, Dinah R Parker, Mohamed Zbiri, Mark R Johnson, Zoltán A Gál, and Simon J Clarke. High-spin cobalt (II) ions in square planar coordination: structures and magnetism of the oxysulfides $Sr_2CoO_2Cu_2S_2$ and $Ba_2CoO_2Cu_2S_2$ and their solid solution. *Journal of the American Chemical Society*, 133(8):2691–2705, 2011.

[33] Howard E Swanson and Eleanor Tatge. Standard x-ray diffraction patterns. *Journal of Research of the National Bureau of Standards*, 46(4):318, 1951.

[34] Armin Kirfel and K Eichhorn. Accurate structure analysis with synchrotron radiation. the electron density in Al_2O_3 and cu_2O. *Acta Crystallographica Section A: Foundations of Crystallography*, 46(4):271–284, 1990.

[35] Ana Borras, Angel Barranco, Juan P Espinós, José Cotrino, Juan P Holgado, and Agustín R González-Elipe. Factors that contribute to the growth of Agα TiO_2 nanofibers by plasma deposition. *Plasma Processes and Polymers*, 4(5):515–527, 2007.

[36] BARRY AUTOR CARTER, David Bernard Williams, C Barry Carter, and David Brian Williams. *Transmission electron microscopy: a textbook for materials science. Diffraction. II*, volume 2. Springer Science & Business Media, 1996.

[37] M Cowley. Stem imaging with a thin annular detector. *Journal of electron microscopy*, 50(3):147–155, 2001.

[38] Eric Dailey and Jeff Drucker. "Seedless" vapor-liquid-solid growth of Si and Ge nanowires: The origin of bimodal diameter distributions. *Journal of Applied Physics*, 105(6):064317, 2009.

[39] Bengt Hallstedt, Daniel Risold, and Ludwibg J Gauckler. Thermodynamic assessment of the copper-oxygen system. *Journal of phase equilibria*, 15(5):483–499, 1994.

[40] Pavel A Korzhavyi and Börje Johansson. Literature review on the properties of cuprous oxide Cu_2O and the process of copper oxidation. 2011.

[41] Schramm L., Behr G., Löser W., and Wetzig K. Thermodynamic reassessment of the Cu-O phase diagram. *Journal of phase equilibria and diffusion*, 26(6):605–612, 2005.

[42] Denis Shishin, Evgueni Jak, and Sergei A Decterov. Thermodynamic assessment and database for the Cu–Fe–O–S system. *Calphad*, 50:144–160, 2015.

[43] Joongchul Park and Joonho Lee. Phase diagram reassessment of Ag–Au system including size effect. *Calphad*, 32(1):135–141, 2008.

[44] Liang LH., Liu D., and Jiang Q. Size-dependent continuous binary solution phase diagram. *Nanotechnology*, 14(4):438, 2003.

[45] . Wang CX and Yang GW. Thermodynamics of metastable phase nucleation at the nanoscale. *Materials Science and Engineering: R: Reports*, 49(6):157–202, 2005.

[46] Chun Cheng Yang and Yiu-Wing Mai. Thermodynamics at the nanoscale: A new approach to the investigation of unique physicochemical properties of nanomaterials. *Materials Science and Engineering: R: Reports*, 79:1–40, 2014.

[47] Dick Bedeaux and Signe Kjelstrup. Hill's nano-thermodynamics is equivalent with Gibbs' thermodynamics for surfaces of constant curvatures. *Chemical Physics Letters*, 707:40–43, 2018.

[48] Eduardo Saiz, Rowland M Cannon, and Antoni P Tomsia. High-temperature wetting and the work of adhesion in metal/oxide systems. *Annu. Rev. Mater. Res.*, 38:197–226, 2008.

[49] James K Olthoff, Richard J Van Brunt, and SB Radovanov. Studies of ion kinetic-energy distributions in the gaseous electronics conference RF reference cell. *Journal of research of the National Institute of Standards and Technology*, 100(4):383, 1995.

[50] George Carter and John Smallwood Colligon. Ion bombardment of solids. *AMERICAN ELSEVIER PUBLISHING CO., NEW YORK, 1968. 446 P*, 1968.

[51] Kress JD., Hanson DE., Voter AF., Liu CL., Liu X-Y., and Coronell DG. Molecular dynamics simulation of Cu and Ar ion sputtering of Cu (111) surfaces. *Journal of Vacuum Science & Technology A: Vacuum, Surfaces, and Films*, 17(5):2819–2825, 1999.

[52] Alexander van Teijlingen, Sean A Davis, and Simon R Hall. Size-dependent melting point depression of nickel nanoparticles. *Nanoscale Advances*, 2(6):2347–2351, 2020.

[53] Hasan Hüseyin Kart, H Yildirim, S Ozdemir Kart, and T Çağin. Physical properties of Cu nanoparticles: A molecular dynamics study. *Materials Chemistry and Physics*, 147(1-2):204–212, 2014.

[54] Madan Singh, Sekhants'o Lara, and Spirit Tlali. Effects of size and shape on the specific heat, melting entropy and enthalpy of nanomaterials. *Journal of Taibah University for Science*, 11(6):922–929, 2017.

[55] Rossnagel SM. and Robinson RS. Surface diffusion activation energy determination using ion beam microtexturing. *Journal of Vacuum Science and Technology*, 20(2):195–198, 1982.

[56] Yeong Hwan Ko, Goli Nagaraju, Soo Hyun Lee, and Jae Su Yu. Facile preparation and optoelectronic properties of CuO nanowires for violet light sensing. *Materials Letters*, 117:217–220, 2014.

[57] Markus B Raschke. *Elementary surface reactions of hydrogen and oxygen on silicon: An optical second harmonic investigation*. Herbert Utz Verlag, 1999.

[58] Ugo Valdrè. *Electron microscopy in material science*. Elsevier, 2012.

[59] Klaus Wandelt. *Surface and Interface Science, Volumes 7 and 8: Volume 7-Solid-Liquid and Biological Interfaces; Volume 8-Applications of Surface*. John Wiley & Sons, 2020.

Chapter 5

Unravelling nanometallurgy with *in situ* electron-microscopy: a case study with Cu nanowires*

Author´s Contribution

Diego Santa Rosa Coradini - Conceptualization, Methodology, Investigation, Visualization, Writing the original draft

Cameron Quick - Investigation, Conceptualization, Writing the original draft

Matheus A. Tunes - Investigation, Conceptualization

Patrick D. Willenshofer - Picture editing

Thomas Kremmer - Supervision

Peter J. Uggowitzer - Supervision, Investigation, Methodology, Writing - Review and Editing

Stefan Pogatscher - Project Administration, Supervision, Investigation, Writing - Review and Editing

*Status: Chapter 5 is a paper under revision for publication in the Journal Material Nano Today, written by Diego S. R. Coradini, Cameron Q., Matheus A. Tunes, Patrick D. Willenshofer, Thomas M. Kremmer, Peter J. Uggowitzer, and Stefan Pogatscher.

Acknowledgments

All authors are grateful for the European Research Council (ERC) support via the excellent science grant "TRANSDESIGN" through the Horizon 2020 program under contract 757961 and also for the Austrian Research Promotion Agency (FFG) within the project 3DnanoAnalytics (FFG-No. 858040). MAT acknowledges support from the Laboratory Directed Research and Development (LDRD) program of Los Alamos National Laboratory under contract 20200689PRD2. The authors would like to thank Mr. Matthias Honner and Ms. Nadine Tatzreiter for their support with the Cu NWs solution preparation.

Abstract

Technological advances set new challenges for materials development. Miniaturization of electronic devices demands the migration of metallurgy from macro/micro to the nanoscale, thus requiring a re-definition of existing and classical concepts in metallurgy. The present study reports on the behaviour of pure Cu nanowires with diameters ranging from 40 to 140 nm heated in a low-pressure environment within a transmission electron microscope. The response of Cu nanowires was investigated at different temperatures up to 1123 K and analyzed using electron-microscopy techniques, revealing both volumetric and shape changes over time. Sublimation, with a steady-state length reduction of the nanowires, was identified as the dominant mechanism. Additionally, it was detected that sublimation occurred not only at temperatures above $\approx$ 1023 K, where Cu has a higher vapor pressure than the column pressure of the electron-microscope, but also at temperatures as low as 923 K. This unexpected behavior is explained by the presence of active regions at sharply curved regions at the nanowire tip and the imbalance of evaporation and redeposition rates of Cu atoms due to the experimentally-induced loss of vapor atoms. Nevertheless, by studying the Cu at the nanoscale, some fundamental aspects of the field of nanometallurgy are unraveled.

5.1 Introduction

Copper (Cu) has a rich history that has shaped the development of modern society, dating back to its first use in the Cu and Bronze Ages. Despite its traditional origins, Cu is still intensively studied at the frontiers of materials science. It is ubiquitous in electronics [1, 2], with a wide range of applications and contributing to the improvement and miniaturisation of circuits and electronic components, always extending the limits of Moore's law [3, 4, 5, 6, 7, 8, 9, 10]. It is used, for example, in high-efficiency vehicles or devices that require high power and are used over long time periods [11, 12, 13]. In addition, more than 80% of Cu is used in electronics and has a great price advantage compared to other metals [10, 14].

Further miniaturization of the electronics industry requires the study of metals proceeds at both nano and atomic scales, therefore, the invention of a new fundamental research field – the "nanometallurgy" – is required. Applications of metals and alloys as nanomaterials are a relatively new topic of research that spans over the last two decades [15, 16]. Hence, their processing techniques are still under development and has limitations. In the literature, specific properties of nanomaterials are generally attributed to their high surface-to-volume ratio and surface energy [17, 18, 19]. This enables them to maintain metastable phases, which is not possible for their bulk counterparts [20]. A classic example relating to the high surface-to-volume ratio is the melting point depression observed in metals such as Cu, Ni, Au, and Ag when in a form of nanomaterials [21, 19, 22]. However, the same properties that are desirable on the surface at the nanoscale can result in degradation, as shown in previous work where a Cu nanowire (NW), exposed to a low-reactive plasma containing impurities, degraded into CuO-Cu_2O nanoclusters [23]. Another fact reported in the literature concerns the sublimation of Ag and Mg nanoparticles in the Transmission Electron Microscope (TEM) [24, 25, 26, 27]. In these studies, the sublimation effect occurs at temperatures lower than the melting point and is mainly associated with surface energy effects, showing that nanometals undergo continuous sublimation when their radii are around 50 nm, or discontinuous sublimation when the radii are below 30 nm [24, 25, 26]. It is also worth mentioning other degradation effects observed in nanomaterials in TEM and Scanning Electron Microscope (SEM), such as the Rayleigh effect in Cu NW and Sn NW with a radius of about 30-50 nm [28, 29]. In Ag NW

networks, coalescence effects are observed when annealing is performed at temperatures up to 623 K [30]. Furthermore, a relationship between the surface-to-volume ratio of a NW and the cohesive energy was obtained, with a decrease in the cohesive energy for NWs smaller than 10 nm [8, 31].

Understanding the impact of surface effects on the behaviour of nanomaterials and its relationship with the thermodynamics of metals when confined to the nanoscale is of paramount importance for further establishing the field of nanometallurgy. This is due to the fact that classical concepts in metallurgy, derived from both empirical and theoretical knowledge from thousands of years of the investigation of metals, may drastically change in the nanoworld. Herein, we revisit the classical metallurgy study of the metal Cu, but at the nanoscale by means of *in situ* TEM experiments. We show this methodology can be used to harness the potential of nanometallurgy by studying how intensive and extensive thermodynamic core-properties are of particular importance when the metal Cu is confined within the nanoscale.

5.2 Experimental

5.2.1 Sample preparation for the transmission electron microscope (TEM)

Two types of MEMS chip sensors were used, SiN coated and uncoated e-chips from Protochips for Vacuum Applications. A solution supplied by SIGMA-ALDRICH (lot number MKCL4540) containing Cu NWs was used to place the Cu NWs on the chip membrane. The initial solution contained 5mg Cu NWs (99.999 %) in 1 ml C_2H_5OH with an average diameter of 80 nm $\pm$ 60 nm. To avoid stacking of the NW on the MEMS e-chips, the solution was diluted to 0.126 wt% by mixing 8 mg of the original solution with 6.35 g of ethanol (measured with Satorius precision analytical balance). Prior to TEM pre-characterization, the 0.126 wt% solution was treated in an ultrasonic bath for 15 min to disperse the Cu-NW in the solution. After treatment in the ultrasonic bath, 3 drops of the solution were pipetted onto the MEMS chips. This was repeated once the first application was dry. The e-chip was then placed on the Fusion Select double-tip holder from Protochips [23].

5.2.2 TEM analysis

Analyses in TEM (ThermoFisher ScientificTM Talos F200X) were performed differently for each set of objectives. Bright-field TEM (BFTEM) with a magnification of 310kX and electron diffraction in selected regions (SAED) were used for the experiments investigating the passivation layer. These experiments focused only on a limited area of the NW since the goal was to elucidate the evolution of the passivation layer morphology. High-angle annular dark field (HAADF) on the other hand was used for the analyses of the sublimation rate. The use of HAADF was required because of its advantages in the depth of field, maintaining each NW in focus during the acquisition of the experiment, and the use of Z-contrast. A frame rate of 4.235 frames per second with a resolution of 1024x1024 pixels was used for the acquisition.

5.2.3 Beam effect experiment

To analyse if the electron beam would affect the sublimation behaviour, an experiment was performed with minimal beam influence. The beam was exposing the samples only to observe the volume decrease over time and it remained "off" for most of the experiment. Moreover, the sublimation effect was observed under temperatures of 923 and 973 K. Where at 973 K, the observation was made periodically every 30 min being the beam was closed for most of the experiment, which went for 230 min. Additionally, for 1023 K, the observation occurred every 5 min for the first 40 min. After it, the NW was observed every 20 min until the end of the experiment which took 160 min.

5.2.4 Image analyses

Velox software was used for image analysis. This made it possible to manually measure the change in length of the NW. For each NW examined, at least 5 length measurements were made, each at a distance of about 50 to 200 nm, to record the length change over time. For each of the selected test temperatures (923, 973, 1023, 1053, 1073, and 1123K), such a procedure was performed at approximately 6 NW. Thus, a total of more than 180 length/time value pairs were used to assess the sublimation behaviour.

5.3 Results and Discussion

5.3.1 Morphological changes and solid-vapour transition

The first series of experiments illustrate the observed phenomena of morphological changes of Cu-NW when heated in the TEM at a column pressure of $\approx 3–8\times10^{-6}$ Pa. The experiments have been performed under bright-field TEM (BFTEM). In the first experiment, a temperature increase with time was manually applied. Figure 5.1 shows the changes on the surface of the NW at temperatures up to 673 K, Fig. 5.1a-c. It can be seen that the twin located in the center of the NW disappears, and the oxide layer around the NW becomes thinner. Such effects of thinning of the passivation layer was observed occurring in Cu nanoparticles when annealed within a TEM [32]. The thinning of the oxide layer might be connected to desorption caused by the low pressure and high temperatures. Thermal decomposition under vacuum is also a potential process described in the literature [33]. Along with that, an EDS micrograph of a pristine NW is presented in the appendix in Figure 5.8 illustrating the oxide and C layer before the heating. These changes occurred before volume loss was observed. Fig. 5.1d-f shows the morphological change during annealing treatment for 6.5 ks at 973 K. The Cu NW has vanished completely. After degradation, only a "shell" from the surface layer of the NW remain, which consist mainly of C, as shown by the elemental mapping obtained with EDX in Fig. 5.1f. Similar observation can be found in the Literature [27, 34, 35].It is important to remark that the C present is a typical result of contamination in TEM. Possible sources could result from the existence of surfactants over the NWs or even come from the isopropanol used to prepare the sample [36].

The observations shown in Fig. 5.1 leads to the following question: which mechanism responsible for the degradation of the Cu NWs? In principle, three mechanisms have to be considered: (i) melting followed by evaporation, (ii) damage and/or heating induced by the electron beam, and (iii) direct sublimation of the Cu NWs.

To determine whether melting takes place or not, a probing experiment was performed using the scanning transmission electron mode (STEM), both equipped with dark-field (DF), and high-angle annular dark field (HAADF) detectors. Fig. 5.2 shows an isolated Cu NW at 1123 K. The aim was to detect a possible molten state in which the material

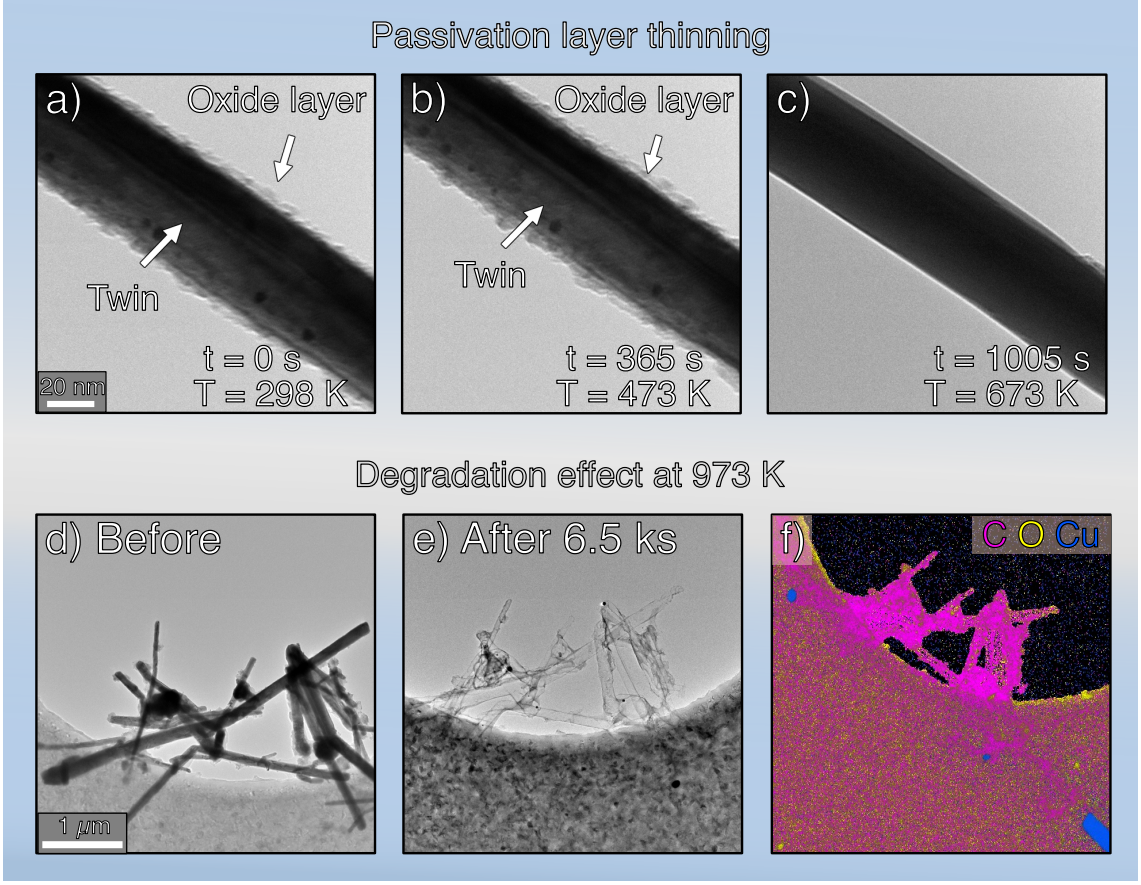

Figure 5.1: BFTEM micrographs and EDX of Cu NW; a) to c): Modifications on th surface of the NW by thinning of the oxide layer; d) and e): BFTEM micrographs showing a stack of Cu NWs before and after annealing at 973 K. Complete degradation of the NWs occured after 6.5 ks; f) STEM-EDX elemental map showing mainly the presence of carbon after annealing.

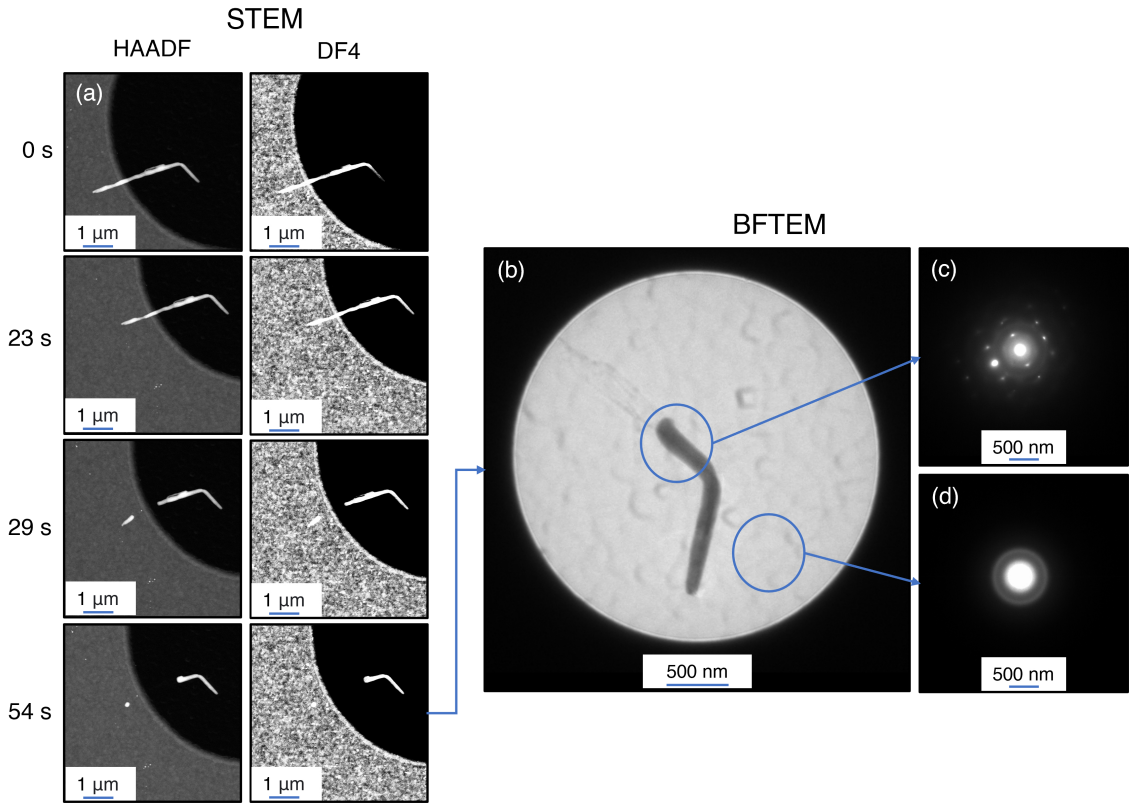

Figure 5.2: In situ TEM analysis of the material while holding at 1123K; (a) HAADF and DF sequences showing the sublimation effect; (b) BFTEM of the area where the convergent electron diffraction pattern (CBED) was measured; (c) NW CBED pattern and (d) CBED pattern of the amorphous protochip membrane

loses its crystallinity. The temperature of 1123 K was considered because it was the highest temperature used in our experiment. If melting did not occur at this temperature, we would not expect it to occur at temperatures lower than that. In case of melting, no contrast would be visible under DF imaging [37, 38, 39, 40], however, it would still be visible on the HAADF sensor, as it depends on the Z-contrast. Since no such discrepancy in contrast was observed, it can be concluded that the material has not melted. To further support the finding, convergent electron beam diffraction (CBED) was performed at 1123 K [39]. The result is shown in Fig. 5.2c. No loss of the crystallinity was detected, therefore, during the annealing experiments of Cu NWs under the TEM environment, no melting occurred, thus ruling out the melting followed by evaporation mechanism (i).

Regarding the damage caused by the electron beam, previous research refer this mechanism to deleterious effects of high-energetic electrons that may take place in samples during imaging in the TEM, and such a damage manifests in a form of sputtering or heating [41, 24, 42, 43]. Therefore, it was important to understand whether these effects

are also relevant to the observed degradation of Cu NWs during annealing. Equation 1 expresses the total dose (D) for our imaging conditions within the TEM, with the frame dosage (D_f), the number of frames (N_f), the measured beam current (I_b), the frame area (A), and the frame time (t_f):

$$D = D_f N_f = \frac{I_b}{A} t_f N_f \tag{5.1}$$

Under the conditions used in our experiments, the calculated dose was 3.69×10^4 Cm^{-2}. Konrad *et al.* observed the onset of sputtering in Ag nanoparticles (NPs) when the dose was 8.4×10^8 Cm^{-2} [41]. Thus, we conclude that beam damage does not play a significant role in the degradation of Cu NW that we observe (note that Ag and Cu are similar with respect to atomic density and melting point). The hypothesis of temperature increase caused by the electron beam was also checked. We carried out the same annealing experiments by switching off the electron beam and monitoring the Cu NWs periodically, as described in the materials and method section. The electron beam has not changed the degradation observed in Fig. 5.1, thus also ruling out the hypothesis on temperature increase by the electron beam. We can conclude that the electron beam causes no detectable sputtering or heating on the Cu NWs during our experiments, thus discarding the mechanism (ii).

As there is neither evidence of melting followed by evaporation nor any influence of the electron beam in a form of excess heating or sputtering, sublimation is considered to be the main effect behind the observed degradation of Cu NWs within the electron-microscope.

5.3.2 Analysis of the sublimation behaviour

Previous research assessed the sublimation process in nanomaterials. It typically starts from leakage on the surface layer, preferably at the NW's tips, and subsequently extends along its length. Several studies have reported sublimation effects on NPs and NWs made of different materials such as Mg, Ag, GeTe, Zn_2GeO_4 and Cu [27, 24, 35, 34, 44, 45]. These studies point that sublimation usually takes place upon an increased vapour pressure or reduced cohesive energy caused by the highly curved surface of nanomaterials [31, 8, 21]. Based on the experimental observations presented above and in Figs. 5.1 and 5.2, a series of degradation experiments were carried out using Cu NW with a diameter of

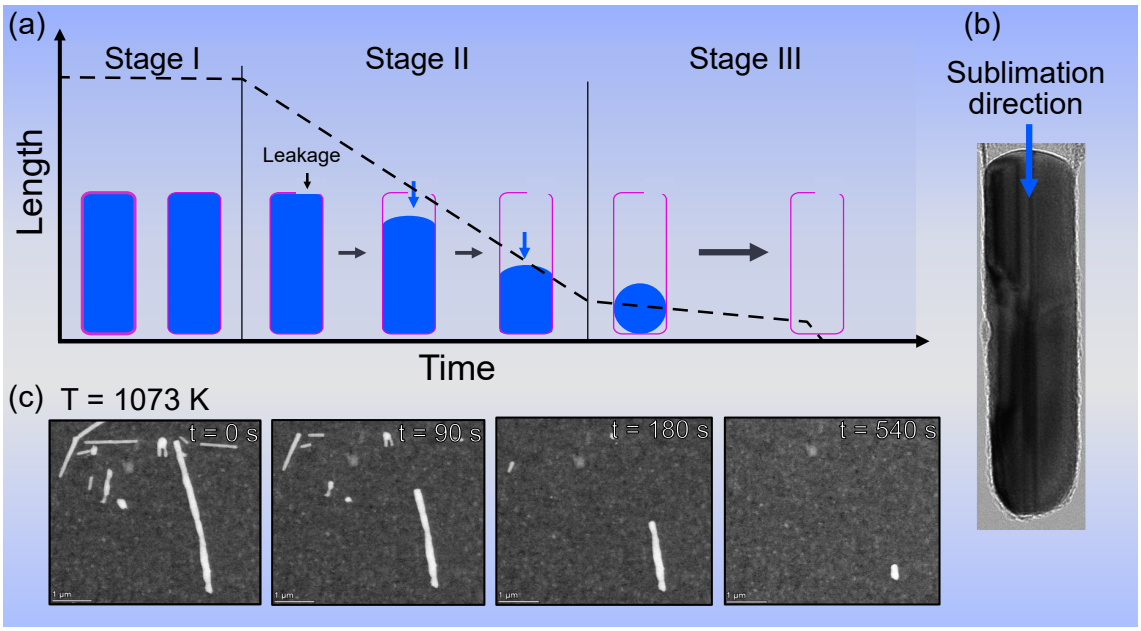

Figure 5.3: Schematic representation of the individual stages of the observed degradation of Cu NWs whilst annealing within the TEM. The sequence of micrographs on the right side was recorded at 1073 K and illustrates the degradation rate in stage II.

approximately 100 nm and in the temperature range from 923 to 1123 K. In each case, the sublimation process was observed to follow the same pattern. After a long initiation (or activation) phase, the onset of thinning and leakage through the oxide passive layer takes place (stage I), the sublimation of the Cu NW manifests itself by its shortening (stage II). The phase II is characterized by a constant sublimation rate. In the final phase, stage III, spheroidization of the Cu NW residue is observed, and after that, the Cu NW is observed to completely vanish. The gaseous phase of Cu escapes through the open surface skin and leaves behind an empty C-rich shell (Fig. 5.1). Fig. 5.3 shows a schematic representation of the individual stages of the degradation, accompanied by corresponding TEM images of the progressing sublimation (see also supplementary movie 1).

The change in the length of the Cu NWs with the annealing time at different temperatures was recorded by means of video sequences that were systematically analyzed. Fig. 5.4a-d shows the result for selected temperatures: 923, 973, 1073, and 1123 K. It is worth noting that the change in length is constant, *i.e.* the sublimated Cu volume increases proportionally with the sublimation time. Thus, a given sublimation rate can be easily determined for each temperature. The temperature dependence of the sublimation rate obtained in this way is shown in Fig. 5.4e for the entire temperature range investigated (additionally including two extra points at both 1023 and 1053 K). From 923 to 1123 K,

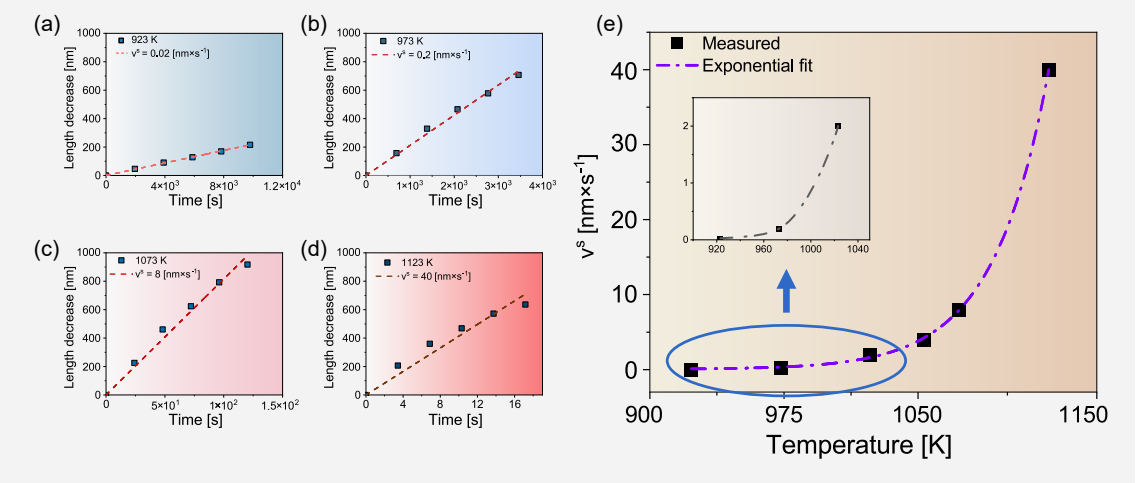

Figure 5.4: Diagrams presenting the sublimation rate (v^s) of Cu NWs with distinct initial (r_0) under different holding temperatures. Inset (a) shows a NW with r_0 = 54.5 nm, heated to 923 K, Inset (b) a NW with r_0 = 54.1 nm, heated to 973 k, Inset (c) a NW with r_0 = 37 nm, heated to 1073 K, and (d) a NW with r_0 = 67.3 nm, heated to 1123 K. The sublimation rate is presented in nm ·s^{-1} as a function of time. The dependence of v^s with the annealing temperature is summarized in (e) showing a clear exponential dependence. Note: the inset shows the variation of the sublimation rate in (e) at the lower temperature range (1073-923 K).

the sublimation rate changes by 3 orders of magnitude from approximately 0.02 to 40 nm·s^{-1}. The sublimation rate has notably an exponential dependence with the annealing temperature.

In order to shed light on these experimental results from a metallurgical point of view, we first consider the temperature range where the sublimation rate changed strongly with the annealing temperature (923 to 1123 K). According to Hertz-Knudson [46], the driving force for the sublimation of a condensed phase is its vapor pressure, or in our case the difference between the Cu vapor pressure, p^V, and the TEM column pressure,p^C. The analytical relationship between the sublimation rate and the difference in pressure is given by:

$$v^s = \frac{C}{\varrho} \cdot \left(\frac{\mu}{2\pi RT}\right)^{0.5} \cdot (p^V - p^C) \tag{5.2}$$

In equation 5.2,ϱ is the density of the sublimating material, μ its molar mass, R is the universal gas constant, T is the temperature on the sublimation surface and C is a dimensionless sublimation coefficient that varies between 0 and 1. The Cu vapour pressure (p^V) was calculated for different temperatures, by using equations given in previous works [47, 48]. The result based on the experimental results and the Kelvin equation show the

opposite of what was observed in the experiments, that Cu NWs exhibit sublimation even below the "threshold temperature" of 1023 K (see inset in Fig.5.4 e). Please note that such unexpected behaviour has also been observed purely phenomenologically in Ag-NWs [35], which makes our model seem generally valid. In the following, we address this unique Cu NW situation and discuss possible reasons for such "unexpected" behaviour. First, we take a closer look at the sublimation front. Figure 5.5 shows its typical shape as it forms during sublimation. Perpendicular to the direction of sublimation, *i.e.* in the axial direction of the NW, a dome forms with a curvature of several tens of nm. This curvature is – qualitatively speaking – more pronounced at lower sublimation temperatures. The transition region to the C-rich outer layer is characterized by the formation of a zone of strong curvature at the edge [35], which has a radius varying from 1 to 10 nm. Here, according to the Kelvin equation [49], the vapor pressure, and consequently the sublimation rate, are increased. This "active site" will now also be operative at temperatures below 1073 K and contribute to the unexpected sublimation behaviour. But, if more Cu atoms are emitted at the edge zones, where a smaller radius triggers sublimation [24], than toward the center of the wire, then this manifests itself in the formation of the observed dome. It is important to remark that in Figure 5.5 some blurred regions are observed. However, such regions are likely to present due to artifacts caused by the motion of the NWs resulting from the heating and sublimation.

We now determine the extent of the increase in the sublimation rate and the shift in the threshold temperature caused by the experimentally observed sharp curvature. To do this, we extend equation 5.2 by the Kelvin equation, *i.e.* we determine $p^V = p^V(T, r)$, with r as the radius of curvature. Fig. 5.6a-b illustrates the result of the calculation for $r = \infty$, $r = 5$nm and $r = 1$ nm, and a surface energy of 1.52 J·m^{-2} [50] (note that the sublimation coefficient C in equation 5.2 was set 1). Several conclusions can be drawn from the plots presented in Fig. 5.6: (i) The sublimation rate increases significantly at the active spot, by about an order of magnitude for r = 1 nm, (ii) at the same time, the threshold temperature shifts by a delta of 77 K from 1027 K to 950 K. However, this still does not explain why the measured sublimation – although small at 0.02 nm·s^{-1} – occurs at temperature of 923 K. Obviously, another aspect has to be considered, which we now identify as a sublimation-deposition imbalance.

The equilibrium vapor pressure can be defined as the pressure that is obtained when

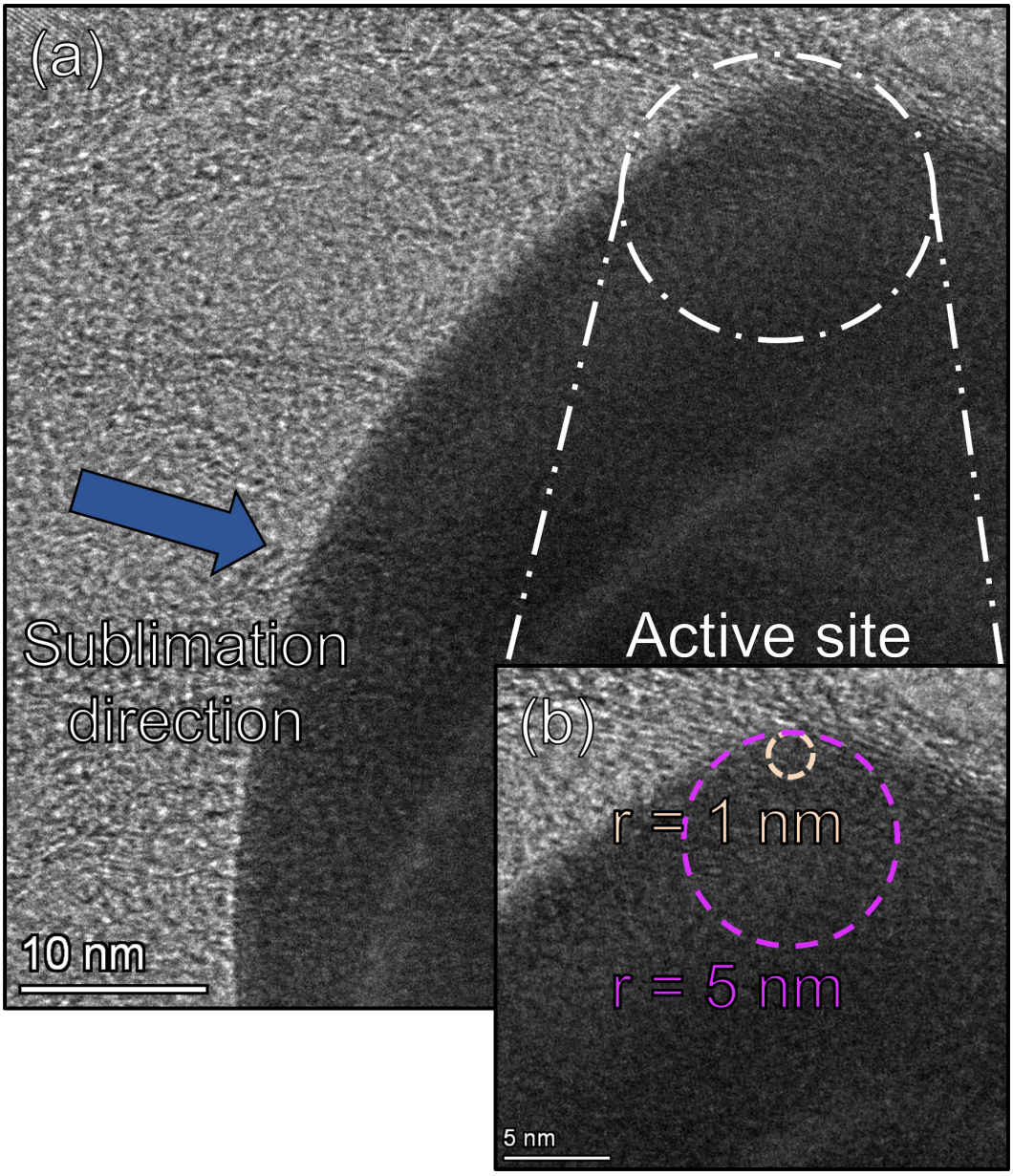

Figure 5.5: (a) High-resolution BFTEM of the Cu NW tip during sublimation at 1073 K. In the transition region to the C-rich outer layer, a zone of sharp curvature forms at the edge. Here, the vapor pressure and consequently also the sublimation rate are increased. These zones can be referred to as an "active site" and can have different radii of curvature.

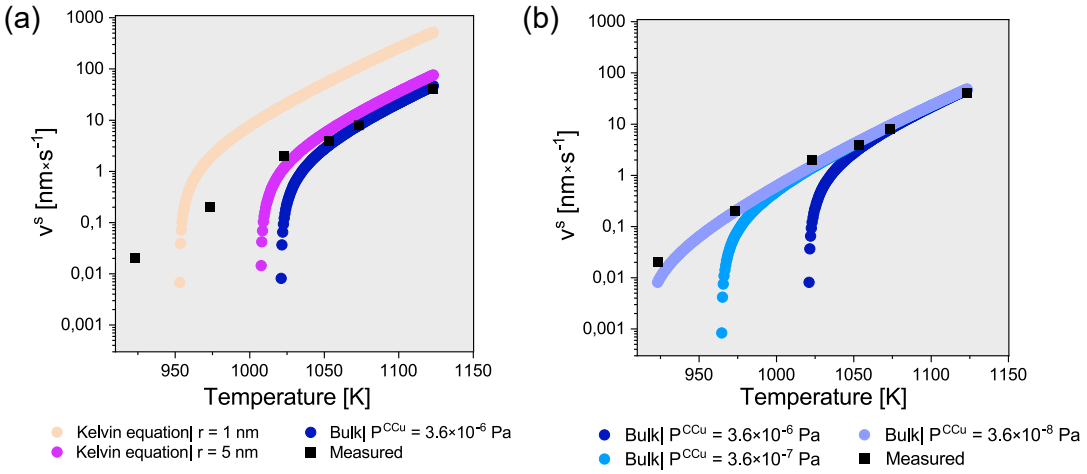

Figure 5.6: Comparison between the measured sublimation rate (v^s) versus calculated values on the basis of equation 5.2: (a) Influence of the edge curvature ($r = \infty$ (bulk), 5 nm and 1 nm) by considering the change of the vapor pressure, p^V, using the Kelvin equation [49]; (b) Influence of the column Cu vapor partial pressure, p^{CCu}, on the sublimation rate, assuming that the column Cu vapor partial pressure is lower than the TEM column pressure due to the escape of Cu vapor from the NW shell.

a condensed phase is in equilibrium with its own vapor. In the case of the Cu NW, this pressure is that at which the Cu evaporation rate equals the redeposition rate of the Cu vapor phase. However, this view implies a closed system, which is not applicable to our situation. As noted earlier, Cu atoms escape from the carbon shell through a leakage. They will deposit eventually at the cold column wall within the TEM. Seen in this way, we are dealing with an open system, in which the walls of the TEM chamber with a temperature of around 298 K work as a cold finger, and thus the column pressure in equation (2) can be neglected. This, however, shifts the evaporation-deposition balance in favor of evaporation. In other words, it is not the column pressure *per se* that is decisive for the ambient pressure, but the column Cu vapor partial pressure, p^{CCu}. However, because of the loss of Cu vapor, p^{CCu} is lower than the TEM column pressure p^C. Fig. 5.6 b illustrates the influence of the column Cu vapor partial pressure, *i.e.* the pressure difference (p^V-p^{CCu}) on the sublimation rate. It can be seen that a reduction of p^{CCu} by one order of magnitude will shift the limiting temperature for sublimation by about 100 K to lower values. Thus, it seems quite plausible that the interaction of active spots and a sublimation-deposition imbalance caused by Cu vapor loss can be considered responsible for the shift of the sublimation limit temperature down to values as low as 923 K.

As it is the sublimation enthalpy (ΔH_{subl}) that reflects the energy required to transform atoms from the solid crystal into vapor, we now consider the activation energy which

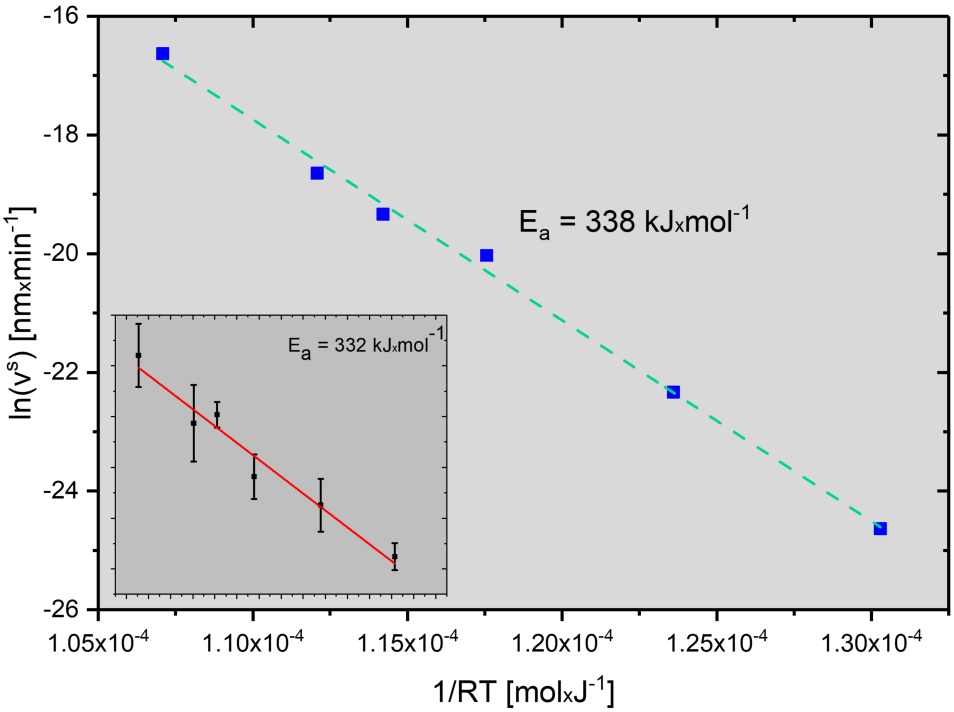

Figure 5.7: Arrhenius plot of the measured values where the x-axis shows the ln of the sublimation rate in nm.s^{-1} and the y-axis shows the temperature multiplied by the gas constant; (a) shows a fit where the activation energy is 338 kJmol^{-1}; (b) presents a fit considering the whole dataset where the activation energy is 332 kJmol^{-1}.

can be derived from the experiments carried out. The exponential dependence of the sublimation rate on temperature shown in Fig. 5.4e is illustrated in Fig. 5.7 as an Arrhenius plot. A straight line fit reveals an activation energy of 338 kJ·mol^{-1}, which surprisingly agrees with published data for the sublimation enthalpy of Cu (ΔH_{subl} = 337.2 ± 1.7 kJ·mol^{-1}) [47]. The insert in Fig. 5.7 shows the Arrhenius plot for all measured Cu NW, even for those wires that varied in diameter from 40 nm to 140 nm. A considerable scattering of the data can be seen, but the activation energy is comparable to that evaluated with the selected reduced data set. Although not specifically mentioned here, it can be stated that the thinner NWs degrade somehow faster, which could be explained by a greater effect of the active sites, because of the higher specific proportion. However, due to the scatter of the data, a quantitative evaluation of the diameter influence was not performed.

Besides the influence of the NWs radii, additional factors may be responsible for the scatter of the data, namely different sizes, shapes, numbers, and positions of the leakages in the C-rich outer layer as well as variations in the temperature of the NW due to a

beam effect. In order to clarify whether the electron beam heats the Cu NW and thus influences the sublimation behavior, experiments were conducted in which the beam was only open for a short time in order to measure the length change. For example, during a test at 923 K, which lasted 230 minutes, measurements were made only every 30 minutes, meaning that the beam was closed for most of the experiment. At 1023 K, the length determination was done every 5 minutes for the first 40 minutes, after which the NW was measured every 20 minutes until the end of the experiment, which took 160 minutes. In both experiments, the deviation from the experiment with a permanently open beam was insignificant.

In stage III, the final phase of the degradation process, a spheroidization of the Cu NW residues is observed. It was found that the sublimation of these spherical nanoparticles generally occurs at a lower rate than that of NW (see a kink in the schematic diagram in Fig. 5.3a). A possible explanation is provided by the omission of active sites, since here, at least up to the terminal step, no extreme radii of curvature are present.

5.4 Conclusions

We observed that Cu NWs degrade upon temperature under low pressure in distinct stages. In the initial stage, the passivation layer on the surface of the Cu NWs is thinned and breaks open, triggering a second stage of degradation characterized by a shortening of NWs at a constant length reduction rate driven by sublimation. In the last stage, spheroidization and sublimation at lower rates are observed. Looking at the temperature dependence of the sublimation effect at a fundamental level gives remarkable interesting insights for establishing the field of nanometallurgy. The temperature dependence of sublimation is governed by the enthalpy of sublimation. However, the temperature range where sublimation happens is surprisingly wide. That Cu sublimates when exhibited to temperature-pressure conditions, where the Cu vapor pressure is above the ambient pressure is common textbook knowledge and can be well described by the Herz-Knudsen equation. But, herein we observed that even a difference of 150 K below the equilibrium temperature where the Cu vapor pressure equals the ambient pressure significant sublimation occurs. Simply considering the NWs‘ radii by the Kelvin equation cannot explain the effect for the studied nanowire diameters (around 100 nm). Using *in situ* electron-

microscopy we found that a sharp edge in the range of a few nanometers can exist at the sublimation front during the length reduction stage which acts as an active spot to trigger further sublimation at lower vapor pressure. Nevertheless, such a low-temperature limit, which can be derived from the established theory of reaction rates and thermodynamics and their size dependence, proves to be insufficient to describe satisfactorily the sublimation observed at low temperatures. A potential explanation can be given by the imbalance between the sublimation-deposition part of the reaction due to the non-closed system and the resulting Cu vapor loss.

Our experimental findings clearly demonstrates that metals at nanoscale can degrade via sublimation at unexpectedly low temperatures, which needs to be considered in future products made from such materials, such as nanoalloys for functional applications. The field of nanometallurgy is emerging and it will be not surprising if deviations from classical theories are unexpectedly observed in future experiments.

5.5 Appendix: Supplementary information

Supplementary movie 1.

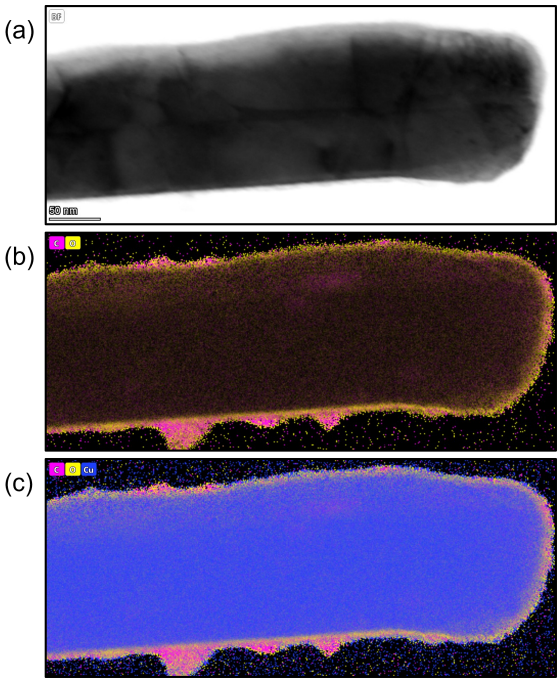

Figure 5.8: The micrograph shows an Energy Dispersive X-ray Spectroscopy (EDS) image of a nanowire (NW), captured using the Bright-Field Scanning Transmission Electron Microscopy (BF-STEM) sensor. Inset a) displays the micrograph of the NW, which was taken using the BF-STEM sensor. Inset b) presents the EDS map, showing only C and O's presence on a pristine NW. Inset c) displays the complete EDS map, which considers the presence Cu in addition to C and O.

5.6 Reference

[1] Rolf E Hummel. The first materials (stone age and copper-stone age). In *Understanding Materials Science*, pages 3–11. Springer, 1998.

[2] Ronald Frank Tylecote. *A history of metallurgy*. 1992.

[3] Robert Chau, Suman Datta, and Amlan Majumdar. Opportunities and challenges of iii-v nanoelectronics for future high-speed, low-power logic applications. In *IEEE Compound Semiconductor Integrated Circuit Symposium, 2005. CSIC'05.*, pages 4–pp. IEEE, 2005.

[4] Mark A Koten, SA Voeller, MM Patterson, and Jeffrey E Shield. In situ measurements of plasma properties during gas-condensation of cu nanoparticles. *Journal of Applied Physics*, 119(11):114306, 2016.

[5] Peter Sutter. How silicon leaves the scene. *Nature materials*, 8(3):171–172, 2009.

[6] BC Gibson, JR Williams, AT Fromhold Jr, MJ Bozack, WC Neely, and Ann F Whitaker. The interaction of atomic oxygen with thin copper films. *The Journal of chemical physics*, 96(3):2318–2323, 1992.

[7] JK Kennedy and Cody Friesen. The effect of oxygen adsorption on cu {111} thin film growth stresses. *Journal of Applied Physics*, 101(5):054904, 2007.

[8] Rong Chen, Yi-Cheng Li, Jia-Ming Cai, Kun Cao, et al. Atomic level deposition to extend moore's law and beyond. *International Journal of Extreme Manufacturing*, 2(2):022002, 2020.

[9] Mahmudul Islam, Md Shajedul Hoque Thakur, Satyajit Mojumder, Abdullah Al Amin, and Md Mahbubul Islam. Mechanical and vibrational characteristics of functionally graded cu–ni nanowire: A molecular dynamics study. *Composites Part B: Engineering*, 198:108212, 2020.

[10] Xingsheng Li, Yumeng Wang, Chengri Yin, and Zhenxing Yin. Copper nanowires in recent electronic applications: progress and perspectives. *Journal of Materials Chemistry C*, 8(3):849–872, 2020.

[11] Michael T Barako, Vincent Gambin, and Jesse Tice. Integrated nanomaterials for extreme thermal management: A perspective for aerospace applications. *Nanotechnology*, 29(15):154003, 2018.

[12] James Benford. Space applications of high-power microwaves. *IEEE Transactions on Plasma Science*, 36(3):569–581, 2008.

[13] Sung Mi Jung, Daniel J Preston, Hyun Young Jung, Zhengtao Deng, Evelyn N Wang, and Jing Kong. Porous cu nanowire aerosponges from one-step assembly and their applications in heat dissipation. *Advanced Materials*, 28(7):1413–1419, 2016.

[14] Tapan Gupta. *Copper interconnect technology*. Springer Science & Business Media, 2010.

[15] Eduard Arzt, Stanislav Gorb, and Ralph Spolenak. From micro to nano contacts in biological attachment devices. *Proceedings of the National Academy of Sciences*, 100(19):10603–10606, 2003.

[16] Ralph Spolenak. *Mechanical properties of metals at the nanoscale*. World Scientific, 2011.

[17] G Ouyang, XL Li, X Tan, and GW Yang. Surface energy of nanowires. *Nanotechnology*, 19(4):045709, 2008.

[18] WH Qi and MP Wang. Size effect on the cohesive energy of nanoparticle. *Journal of Materials Science Letters*, 21(22):1743–1745, 2002.

[19] Alexander van Teijlingen, Sean A Davis, and Simon R Hall. Size-dependent melting point depression of nickel nanoparticles. *Nanoscale Advances*, 2020.

[20] Zhen Hua Li and Donald G Truhlar. Nanothermodynamics of metal nanoparticles. *Chemical Science*, 5(7):2605–2624, 2014.

[21] Madan Singh, Sekhants'o Lara, and Spirit Tlali. Effects of size and shape on the specific heat, melting entropy and enthalpy of nanomaterials. *Journal of Taibah University for Science*, 11(6):922–929, 2017.

[22] Dan McLachlan Jr and Ernest G Ehlers. Effect of pressure on the melting temperature of metals. *Journal of Geophysical Research*, 76(11):2780–2789, 1971.

[23] Diego SR Coradini, Matheus A Tunes, Thomas M Kremmer, Claudio G Schön, Peter J Uggowitzer, and Stefan Pogatscher. Degradation of cu nanowires in a low-reactive plasma environment. *npj Materials Degradation*, 4(1):1–8, 2020.

[24] Michael A Asoro, Desiderio Kovar, and Paulo J Ferreira. In situ transmission electron microscopy observations of sublimation in silver nanoparticles. *ACS nano*, 7(9):7844–7852, 2013.

[25] Junjie Li, Zhongchang Wang, Yunping Li, and Francis Leonard Deepak. In situ atomic-scale observation of kinetic pathways of sublimation in silver nanoparticles. *Advanced Science*, 6(8):1802131, 2019.

[26] Qian Yu, Min-Min Mao, Qing-Jie Li, Xiao-Qian Fu, He Tian, Ji-Xue Li, Scott X Mao, and Ze Zhang. In situ observation on dislocation-controlled sublimation of mg nanoparticles. *Nano letters*, 16(2):1156–1160, 2016.

[27] Jiwon Jeong, Subin Lee, Youbin Kim, Seung Min Han, Daniel Kiener, Youn-Bae Kang, and Sang Ho Oh. Microstructural evolution of a focused ion beam fabricated mg nanopillar at high temperatures: Defect annihilation and sublimation. *Scripta Materialia*, 86:44–47, 2014.

[28] ME Toimil Molares, AG Balogh, TW Cornelius, R Neumann, and C Trautmann. Fragmentation of nanowires driven by rayleigh instability. *Applied physics letters*, 85(22):5337–5339, 2004.

[29] Ho Sun Shin, Jin Yu, and Jae Yong Song. Size-dependent thermal instability and melting behavior of sn nanowires. *Applied Physics Letters*, 91(17):173106, 2007.

[30] DP Langley, Mélanie Lagrange, Gael Giusti, Carmen Jiménez, Yves Bréchet, Ngoc Duy Nguyen, and Daniel Bellet. Metallic nanowire networks: effects of thermal annealing on electrical resistance. *Nanoscale*, 6(22):13535–13543, 2014.

[31] Xinlei Li. Modeling the size-and shape-dependent cohesive energy of nanomaterials and its applications in heterogeneous systems. *Nanotechnology*, 25(18):185702, 2014.

[32] Zaoli Zhang and Dangsheng Su. Behaviour of tem metal grids during in-situ heating experiments. *Ultramicroscopy*, 109(6):766–774, 2009.

[33] M Liehr, JE Lewis, and Go W Rubloff. Kinetics of high-temperature thermal decomposition of sio2 on si (100). *Journal of Vacuum Science & Technology A: Vacuum, Surfaces, and Films*, 5(4):1559–1562, 1987.

[34] Joanne WL Yim, Bin Xiang, and Junqiao Wu. Sublimation of gete nanowires and evidence of its size effect studied by in situ tem. *Journal of the American Chemical Society*, 131(40):14526–14530, 2009.

[35] Ruixue Lian, Han Yu, Longbing He, Lei Zhang, Yilong Zhou, Xinyang Bu, Tao Xu, and Litao Sun. Sublimation of ag nanocrystals and their wetting behaviors with graphene and carbon nanotubes. *Carbon*, 101:368–376, 2016.

[36] Simon Hettler, Manuel Dries, Peter Hermann, Martin Obermair, Dagmar Gerthsen, and Marek Malac. Carbon contamination in scanning transmission electron microscopy and its impact on phase-plate applications. *Micron*, 96:38–47, 2017.

[37] Joachim Loos, Erwan Sourty, Kangbo Lu, Gijsbertus de With, and Svetlana v. Bavel. Imaging polymer systems with high-angle annular dark field scanning transmission electron microscopy (haadf- stem). *Macromolecules*, 42(7):2581–2586, 2009.

[38] Aleksandr Kryshtal, Alexey Minenkov, Sergey Bogatyrenko, and Adam Gruszczyński. Melting process and the size depression of the eutectic temperature in ag/ge and ge/ag/ge layered films. *Journal of Alloys and Compounds*, 786:817–825, 2019.

[39] Takeshi Yokota, M Murayama, and JM Howe. In situ transmission-electron-microscopy investigation of melting in submicron al-si alloy particles under electron-beam irradiation. *Physical review letters*, 91(26):265504, 2003.

[40] Mehrdad Shaygan, Thomas Gemming, Viktor Bezugly, Gianaurelio Cuniberti, Jeong-Soo Lee, and M Meyyappan. In situ observation of melting behavior of znte nanowires. *The Journal of Physical Chemistry C*, 118(27):15061–15067, 2014.

[41] Bárbara Konrad, Zacarias E Fabrim, Mariana M Timm, and Paulo FP Fichtner. Electron irradiation effects on ag nanoparticles. *Journal of Materials Science*, 56(13):8202–8208, 2021.

[42] C Barry Carter and David B Williams. *Transmission electron microscopy: Diffraction, imaging, and spectrometry*. Springer, 2016.

[43] RF Egerton, R McLeod, F Wang, and M Malac. Basic questions related to electron-induced sputtering in the tem. *Ultramicroscopy*, 110(8):991–997, 2010.

[44] Chen Luo, Jiefang Li, Xin Yang, Xing Wu, Siyu Zhong, Chaolun Wang, and Litao Sun. In situ interfacial sublimation of zn2geo4 nanowire for atomic-scale manufacturing. *ACS Applied Nano Materials*, 3(5):4747–4754, 2020.

[45] Chunlin Chen, Ziyu Hu, Yanfen Li, Limin Liu, Hirotaro Mori, and Zhangchang Wang. In-situ high-resolution transmission electron microscopy investigation of overheating of cu nanoparticles. *Scientific reports*, 6(1):1–8, 2016.

[46] Jafar Safarian and Thorvald A Engh. Vacuum evaporation of pure metals. *Metallurgical and Materials Transactions A*, 44(2):747–753, 2013.

[47] JW Arblaster. Thermodynamic properties of copper. *Journal of Phase Equilibria and Diffusion*, 36(5):422–444, 2015.

[48] Herbert N Hersh. The vapor pressure of copper. *Journal of the American Chemical Society*, 75(7):1529–1531, 1953.

[49] LM Skinner and JR Sambles. The kelvin equation—a review. *Journal of Aerosol Science*, 3(3):199–210, 1972.

[50] VK Kumykov, IN Sergeev, VA Sozaev, and MV Gedgagova. Surface tension of copper in solid phase. *Bulletin of the Russian Academy of Sciences: Physics*, 81(3):357–359, 2017.

Chapter 6

In situ transmission electron microscopy as a toolbox for the emerging science of nanometallurgy*

Author´s Contribution

Diego Santa Rosa Coradini - Conceptualization, Methodology, Investigation, Visualization, Writing the original draft

Matheus A. Tunes - Investigation, Conceptualization

Patrick D. Willenshofer - Picture editing, and revision

Sebastian Samberger - Picture editing, and revision

Thomas Kremmer - Supervision

Phillip Dumitraschkewitz - Investigation, Methodology, revision

Peter J. Uggowitzer - Supervision, Investigation, Methodology, Writing - Review and Editing

Stefan Pogatscher - Project Administration, Supervision, Investigation, Writing - Review and Editing

*Status: Chapter 6 is a paper accepted for publication in the Journal RSC – Lab-on-a-chip, written by Diego S R Coradini, Matheus A. Tunes, Patrick D. Willenshofer, Sebastian Samberger, Thomas M. Kremmer, Peter J. Uggowitzer, and Stefan Pogatscher.

Acknowledgments

All authors are grateful for the European Research Council (ERC) support via the excellent science grant "TRANSDESIGN" through the Horizon 2020 program under contract 757961 and also for the Austrian Research Promotion Agency (FFG) within the project 3DnanoAnalytics (FFG-No. 858040). MAT acknowledges support from the Laboratory Directed Research and Development (LDRD) program of Los Alamos National Laboratory under contract 20200689PRD2. The authors would like to thank Mr. Matthias Honner and Ms. Nadine Tatzreiter for their support with the Cu NWs solution preparation.

Abstract

Potential applications of nanomaterials range from electronics to environmental technology, thus a better understanding of their manufacturing and manipulation is of paramount importance. The present study demonstrates a methodology for the use of metallic nanomaterials as reactants to examine nanoalloying *in situ* within a transmission electron microscope. The method is further utilised as a starting point of a metallurgical toolbox, *e.g.* to study subsequent alloying of materials by using a nanoscale-sized chemical reactor for nanometallurgy. Cu nanowires and Au nanoparticles are used for alloying with pure Al, which served as the matrix material in the form of electron transparent lamellae. The results showed that both the Au and Cu nanomaterials alloyed when Al was melted in the transmission electron microscope. However, the eutectic reaction was more pronounced in the Al-Cu system, as predicted from the phase diagram. Interestingly, the mixing of the alloying agents occurred independently of the presence of an oxide layer surrounding the nanowires, nanoparticles, or the Al lamellae while performing the experiments. Overall, these results suggest that transmission electron microscope-based *in situ* melting and alloying is a valuable lab-on-a-chip technique to study the metallurgical processing of nanomaterials for the future development of advanced nanostructured materials.

6.1 Introduction

Energy efficiency and the generation of green energy are trending topics affecting technological development and the design of new materials. To ensure continued economic progress, today's technologies are often based on nanotechnology, which aims at improving both properties and efficiency of existing functional materials. New applications need to comply with stricter environmental and climate protection policies [1]. There are many examples of novel nanomaterial applications varying from electronics to environmental engineering where the manipulation on chips at nanoscale is of great research and development interest [1, 2, 3, 4]. For instance, in the electronics industry, the most commonly discussed challenges concern the miniaturization of circuitry and an increase in efficiency [5, 1, 6]. In the energy storage branch nanometallic alloys are being studied as possible candidates capable of storing thermal energy [7]. In medicine, nanomaterials can be used as drug-delivery systems and biosensors [8]. Environmental engineering uses nanofilters for water cleaning and waste recycling. In the case of polymers, nanoadditives can be added within the process to improve the properties of the recycled material [9]. Other important applications comprise the use of nanoadditives to depolymerize polymers back to monomers for recycling [10] and nanostructuring materials via additive manufacturing which can positively affect the final product properties [11]. Nevertheless, complex manufacturing methods are necessary to enable such applications. Production-wise, two different classifications are considered: top-down and bottom-up processes. The top-down process focuses on atomizing a bulk precursor, which can agglomerate in a film [12]. On the other hand, bottom-up aims at producing material by using basic fundamental blocks like atoms or molecules to generate its final product [13, 14, 15]. As a general example of the top-down route, one could refer to nanolithography [16, 15], where the material is etched from bulk to the desired volume. For the bottom-up route, one can consider techniques like chemical-vapor deposition (CVD), and plasma or flame spraying synthesis [17, 18]. Considering traditional smelting metallurgy on the nanoscale, current literature is limited. Many manufacturing methodologies of nanoscaled materials are based on the bottom-up route. For instance, metallic nanoparticles can be produced via organometallic synthesis or by using a colloidal solution [19]. An alternative could be to use laser metallurgy for the manufacturing of nanoparticles [20]. For the production of alloy nanoclusters

(nanoalloys) ultrasonication can be employed, as it is used in the case of Bi-Sn eutectic nanoalloys [21]. Besides, other techniques like laser vaporization, radiolysis, electrochemical synthesis, ion implantation, chemical reduction, and ion sputtering can be applied in the production of nanoalloys [22]. Ultimately, upon demonstration of alloy design, manufacturing and manipulation at the nanoscale (*i.e.* nanometallurgy), a long-standing desire [23] of producing light sails for photonic-based propulsion of interstellar probes up to fractions of the speed-of-light could be realized and nanomaterials have been recently investigated in this context [24, 25]. The current study aims to introduce a new nanometallurgical method for exploring alloying and phase transformations using nanomaterials in transmission electron microscopy (TEM). This lab-on-a-chip approach, which uses the TEM as a chemical reactor for metals, is based on a previously described method by Tunes *et al.* [26] where a material can be deposited on a micro-electro-mechanical systems (MEMS) chip without the need for focused ion beam (FIB) preparation. The experiments focus on the Al-Cu and Al-Au systems since both have well-established literature on their thermodynamic properties and precipitation sequences [27, 28, 29, 30]. In addition, Cu is a common alloying agent in commercial Al-based systems used for improving precipitation hardening [31, 32, 33]. Therefore, to validate the methodology, the results obtained are compared with previous findings available in the literature.

6.2 Methods

6.2.1 TEM sample preparation

The methodology used for the *in situ* nanomelting and heat treatment setup is shown in Figure 6.1. The drawing illustrates the sequence of steps necessary to obtain a viable sample. The first step is based on the methodology presented by Tunes *et al.* [26], in which a jet-electropolished electron-transparent sample can be sectioned and transferred onto a MEMS chip. For later alloying, a nanomaterial-diluted solution is pipetted upon the latter, which is the substrate and will act as a matrix material. Nanoparticles (NPs) or nanowires (NWs) can also be added before the substrate is transferred to the MEMS chips.

The material used as substrate and base for the *in situ* alloying was pure Al supplied

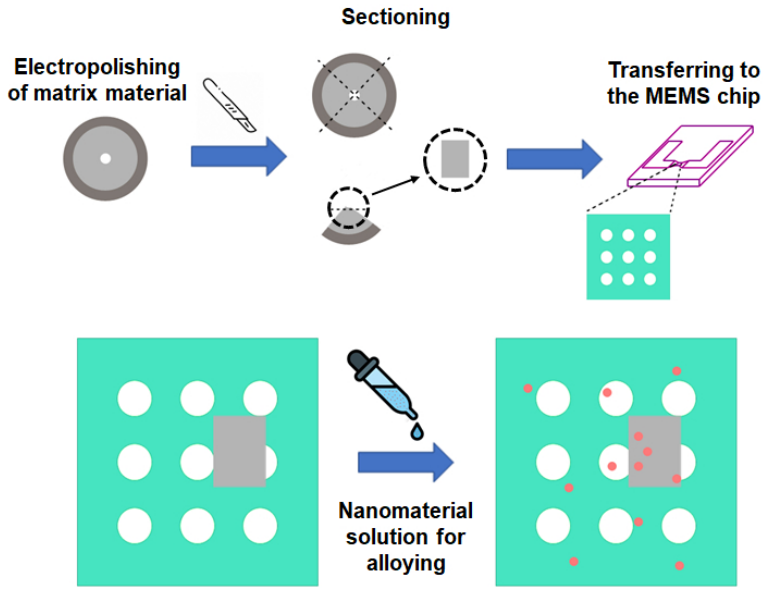

Figure 6.1: The sketch illustrates the preparation of the sample prior to the heating experiments. The sample is electropolished, sectioned using a scalpel, and transferred to a chip where NW or NP solutions are added. Note: this methodology is a modified, but new version of a previously reported sample preparation method for MEMS/TEM analysis [26].

by Sigma-Aldrich with 99.999% purity. For electropolishing, a Struers TenuPol-5 twin-jet electropolishing system was used. The temperature used was –25°C, the voltage was set to 12 V, and the electropolishing solution was composed of 33% nitric acid and 66% methanol in vol.%. After the electropolishing, the TEM lamella was sectioned using a ZEISS SteREO Discovery V12 light stereo-microscope. The sample was divided into 4 equal pieces, where the scalpel cuts through the sample taking the middle as the hole formed by the electropolishing. After the first sectioning, the exposed electron-transparent area is cut again until a piece around 50 μm in diameter is obtained. The sample is then transferred to the MEMs chip sensor membrane with the help of a fine electrostatic bristle used as a manipulator [26]. SiN-coated e-chips from Protochips for Vacuum Applications were used as MEMS chips. Two solutions supplied by Sigma-Aldrich, one containing Cu nanowires, serial number MKCL4540, and the other containing Au nanoparticles, serial number MKCK9621, were used as the carrier substance to be used as alloying elements. The initial solution contained 5 mg Cu NWs (99.999%) in 1 ml of ethyl alcohol with an average diameter of 80±60 nm. The Au NPs were supplied in powder condition with sizes smaller than 100 nm and a purity level of 99.9%. To avoid stacking the NWs and NPs on the MEMS e-chips, the solution was diluted to 0.126 wt.% for both, the Cu-NWs

and the Au-NPs. Prior to TEM pre-characterization, the diluted solutions were treated in an ultrasonic bath for 15 min to disperse the particles within. After treatment in the ultrasonic bath, 3 drops of 20 μm of the solution were poured onto the MEMS chips. This step was repeated once the first application was dried. The specimen was then adjusted with help of the bristle, and the e-chip was then placed on the Fusion Select double-tilt holder from Protochips [34].

6.2.2 MEMS chip sensor calibration

The MEMS chips used in the experiments were additionally calibrated for increased temperature accuracy in the applied temperature ramps. The calibration was performed using a pure Al sample before adding the nanoparticle solution. The FUSION software was utilized to create a heating program that would heat the Al until melting was observed, with the temperature at which melting occurred being considered 660°C. The melting was confirmed by a decrease in the volume of the specimen, as demonstrated in Figure 6.2. The change in shape was used as a marker for melting, as molten material tends to spheroidize. To prevent excessive spheroidization during the following experiments, the material was kept at the melting temperature for only 300 ms.

6.2.3 Heating programs and characterization

The heating programs were designed to allow a meaningful characterization of the sample. Moreover, a comparison of the sample was done prior to and after each step by using a selected area electron diffraction (SAED) pattern, and energy dispersive X-ray spectroscopy (EDX). Further, bright-field TEM and HAADF micrographs were taken. The heating programs used, varied accordingly to the system in question (Al-Au, and Al-Cu), and quenching was done after each heating step to preserve the microstructural state developed during the heat treatment. The two binary systems, Al-Cu and Al-Au, have in common that an eutectic is present on the Al-rich side, Al-Al_2Cu and Al-Al_2Au, respectively. The eutectic temperature is 548 °C for Al-Al_2Cu and 650 °C for Al-Al_2Au. The most significant difference is the maximum solubility, which is 2.5 at-% for Cu [35] and 0.3 at-% for Au [36]. For the Al-Cu system, the heating program starts with the melting of the Al at 660°C, after which the temperature is kept constant for 300 ms. After that

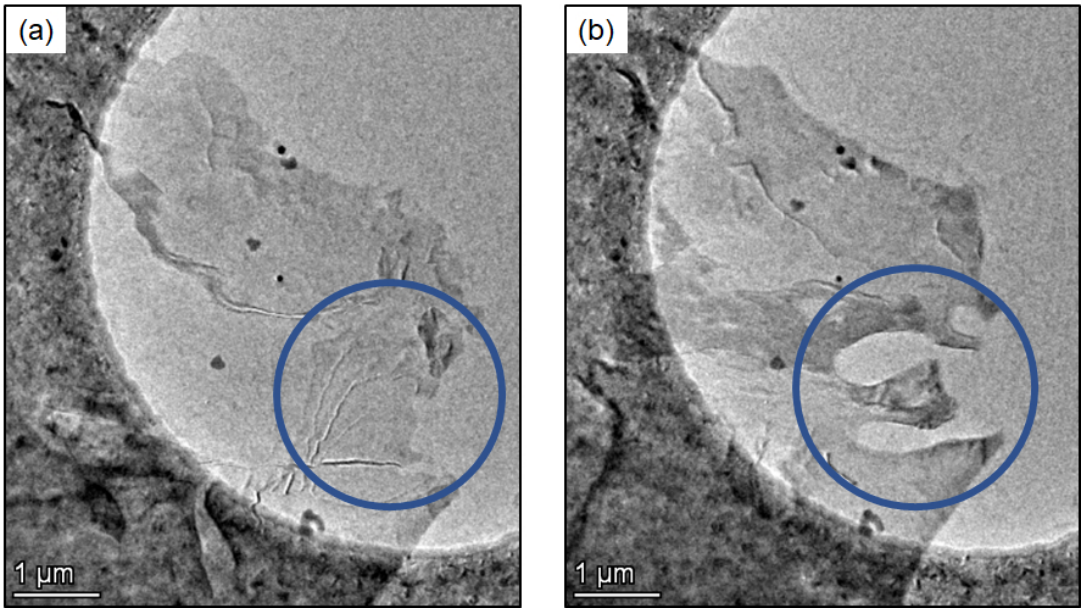

Figure 6.2: BFTEM micrographs featuring an Al thin foil resting on a SiN substrate. The Al foil appears as a translucent, ghostly veil against the darker gray of the substrate. The brighter area on the image indicates a hole present on the SiN substrate. In (a) and (b), a change in shape can be observed within the region highlighted by a blue circle. This alteration in shape was the result of melting and served as a temperature calibration.

two heating sequences were done, and a heating spike to near eutectic temperature (537 °C for 300 ms), in order to simulate solution annealing was applied. Subsequently, the sample was heated for 300 s at 440 °C. A different approach was taken for the Al-Au system to allow the results to be compared with literature data [37]. First, melting was performed (660°C using a 300 ms ramp) followed by a heat treatment at 460 C for 220 seconds. Subsequently, a remelting step at 660°C for 300 ms and a second heat treatment at 250°C for 2 hours was conducted.

6.3 Results and Discussion

The present study demonstrates the application of nanoalloying and the potential of subsequent heat treatment directly within a transmission electron microscope to be used as a metallurgical "lab-on-a-chip", where the sample will be made in situ through alloying, instead of ex-situ. As shown in Figure 6.1, a specific type of TEM sample preparation in combination with a MEMS chip is used to conduct the in situ experiments. The results of the nanometallurgical experiments on the Al-Cu and Al-Au systems are presented and discussed below.

6.3.1 Nanoalloying experiments

To assess the feasibility of melting and dissolving the nanomaterial alloying agents *in situ* within the TEM, both systems were heated to 660°C (the melting point of Al), and the temperature was maintained for 300 ms. The duration of 300 ms was chosen based on the findings of Dumitraschkewitz *et al.* [38] to ensure that melting would occur and to reduce the thickening of the sample due to surface tension. Prolonged exposure to the liquid state increases the risk of spheroidization/balling of the sample. Evidence of melting was observed in both systems, and the formation of an alloy was confirmed by the EDX maps and HAADF STEM micrographs shown in Figures 6.3 and 6.4, which compare the samples before and after melting. For the Al-Cu system, the effects of alloying were more pronounced and well visible by structural dendrite-like features whose formation is most likely due to solidification solute partitioning of Cu. The precipitated phase visible after the alloying experiment is of the type θ-Al_2Cu, as revealed by the SAED analysis (Fig. 6.5). The mixing of the alloying agent occurred regardless of the presence of the oxide layer surrounding the NWs or the Al foil. One possible explanation for this is a thinning of the oxide layers that may occur during heating [39]. Similar effects were noted by Coradini et al., who report that Cu NWs sublime through a leak in the oxide layer caused by the thinning of the layer upon heating [40].

In contrast to Al-Cu, the Al-Au system showed only marginal changes after alloying compared to the initial state. However, a couple of NP clusters dissolved after melting Al (as indicated by the red arrows in Figure 6.4), which indicates that alloying was carried out with it. At this point, it must be noted that at 660°C the equilibrium solubility of Au in the melt is much lower when compared with the Cu in the melt. Being it 2.5 at-% for Au in Al, and 36 at-% for Cu in Al (see phase diagrams in Fig. 6.7). Alloy formation is likely to be correspondingly more sluggish. Furthermore, it is assumed that a large part of the little alloyed Au remains in a supersaturated solid solution after rapid cooling and is not precipitated.

6.3.2 Heat treatments

Now that it has been shown that the alloying experiment was successful, the phase transformations in the course of heat treatment procedures for each system will be presented.

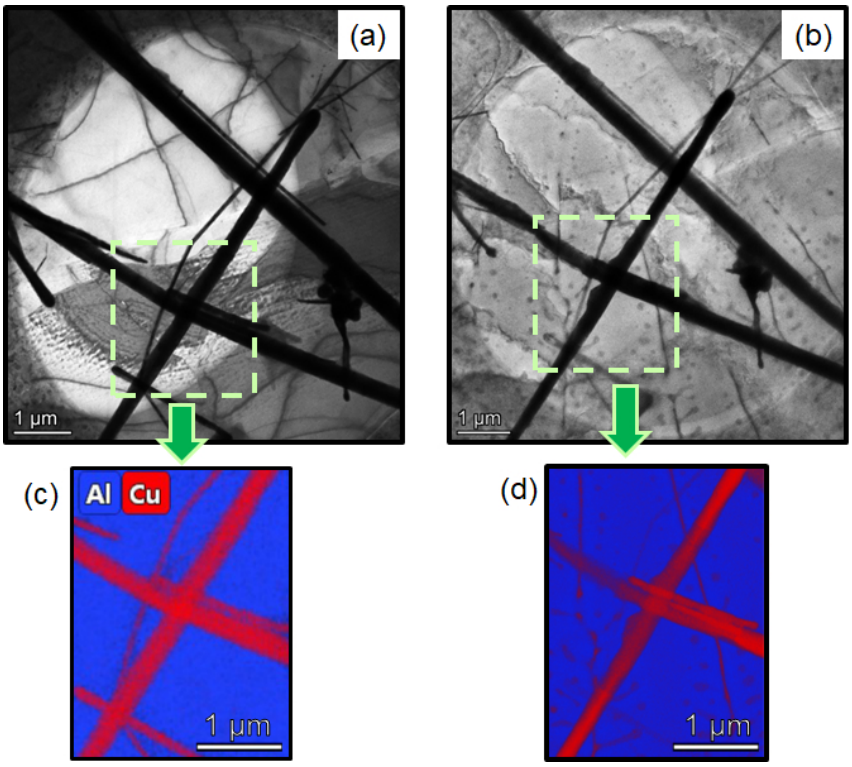

Figure 6.3: Results of melting and alloying for the Al-Cu system. The same region of the Al-Cu sample before and after alloying is shown. In the foreground are the Cu NWs, and in the background is the sample. (a) and (b) show BFTEM micrographs. (c) and (d) display the corresponding EDS maps of the sample.

The results show that the alloys synthesized in the TEM exhibit formation of precipitates, in the Al-Cu system as expected Al_2Cu, and in the Al-Au system, Al_2Au [41, 35]. To ensure that the heat treatment performed as expected, we monitored the composition change of the alloys over time and compared it with a phase diagram. Given the scale of our system, we considered a bulk phase diagram, which is reasonable since only particle sizes smaller than 100 nm show changes in formation temperature. For example, Bajaj et al. showed that the Al-Cu eutectic temperature changes are only significant for particles smaller than 30 nm [42].Since the Al foil in our system falls outside this size range, we did not consider a nanoscale diagram, although there might be minor temperature and solubility shifts. The formation of precipitates in the Al-Cu system at 440°C, following a spike ´solution annealing' at 537°C, is shown in Figure 6.5. After spike solution annealing, i.e. at time t=0, a new structure can be seen. According to the EDX analysis, the Cu content of the alloy is 2.47 at-%. As the annealing time progresses, the coalescence and coarsening of the precipitate progress. At the end of the experiment after 300 s, the matrix shows a depletion of Cu to a value of 0.8 at-%, which agrees very well with the equilibrium

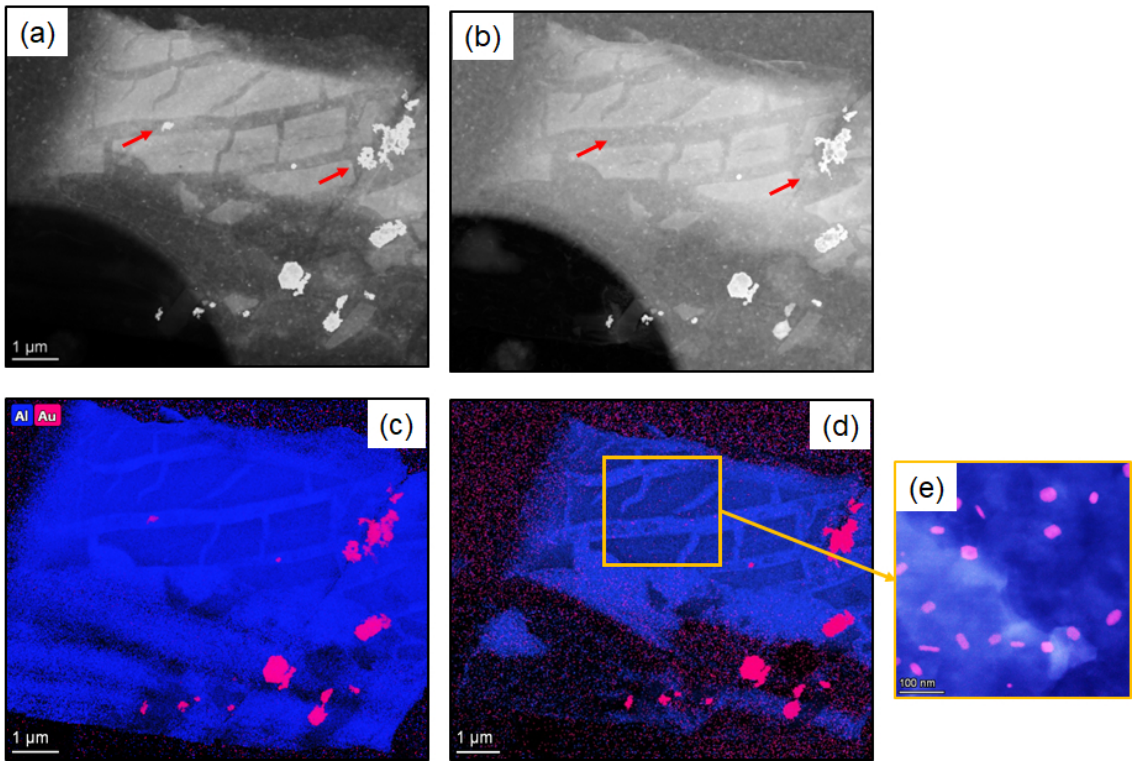

Figure 6.4: Results of melting and alloying for the Al-Au system. HAADF STEM micrographs and EDX maps before and after melting are shown in the insets (a) and (b), (c), and (d), respectively. Some Au NP clusters (highlighted by the red arrows) are no longer present after the melting experiment and small nanometric precipitates formed after solidification, which are presented in the inset (e). Note that the speckled pattern in the dark areas is an artifact of the EDX mapping.

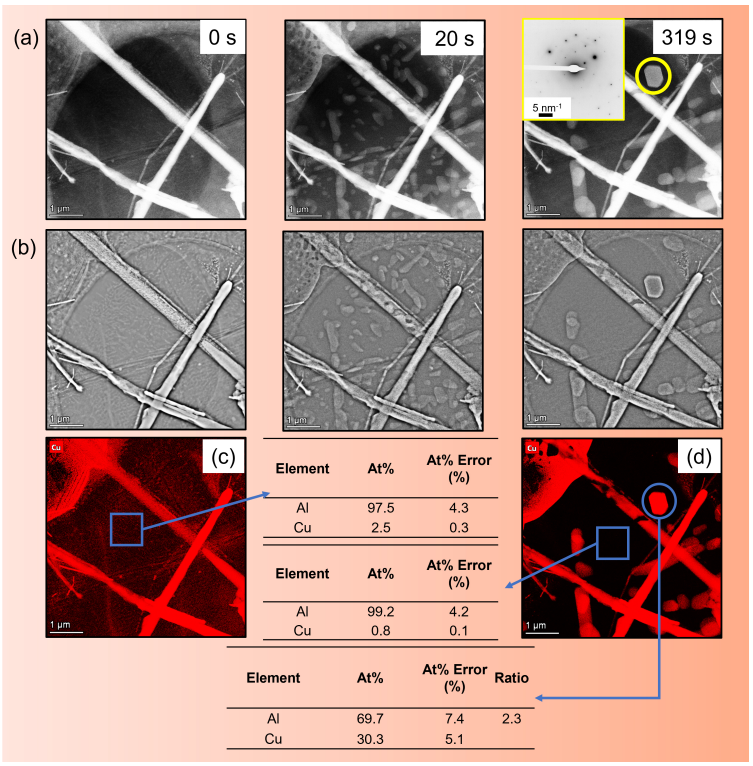

Figure 6.5: Annealing of the Al-Cu system at 440°C after solution treatment (spike annealing at 537°C). The image series (a) display HAADF micrographs taken at different times. Image series (b) show the sequence with a High-Pass filter applied in the Velox software. (c) and (d) show the EDX maps of the composition/matrix composition before and after the heat treatment. At the start of the annealing treatment, a different structure compared to the dendritic-like seen in Figure 6.3 is observed, followed by the spheroidization and coarsening of Al_2Cu-type precipitates (verified with SAED pattern of the precipitates, see insert in series (a) on the right).

concentration at 440°C (see Fig. 6.7). The fact that the precipitates are of Al_2Cu type was confirmed by SAED in Figure 6.5 in the inset (a).

With the intention of obtaining a clear picture of the precipitate formation in the Al-Au system and to be able to make a comparison of results with the literature, heat treatments were performed at two different temperatures, 460°C, and 250°C. The initial condition for the heat treatments was as-alloyed. Solution annealing was not performed due to the low maximum solubility of 0.26 at-%. It is shown in the table in Figure 6.6, that after the alloying procedure at least as much Au is present in supersaturated solution as would be the case after solution heat treatment. We first consider the ageing at 460°C (Fig. 6.6). In the initial state at 0 s, sporadic precipitates (possibly primary Al_2Au) are already present. As the annealing time increases, the precipitates grow and new ones are formed (see light green arrows in image series (a) and compare images (b) and (c)). Simultaneously, the content of Au in solid solution decreases from 0.13 at-% to 0.07 at-%

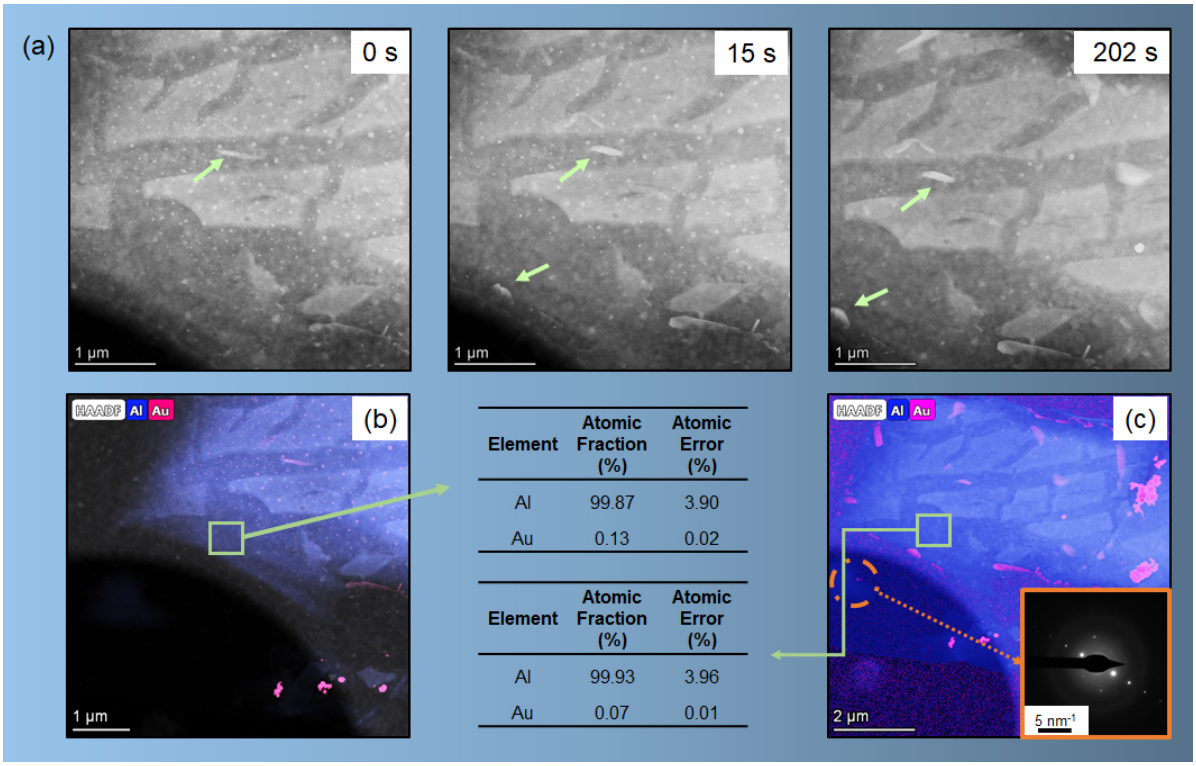

Figure 6.6: Annealing of the Al-Au system at 460°C after melting. The image series (a) display HAADF micrographs taken at different times, starting with the as-alloyed state (0 s). (b) and (c) show the EDX maps of the matrix composition before and after the heat treatment, respectively. At the start of the annealing treatment, precipitates are sporadically present in the Al matrix, followed by the formation of Al_2Au-type precipitates and EDS (indicated by the SAED pattern of the precipitates, see insert in c).

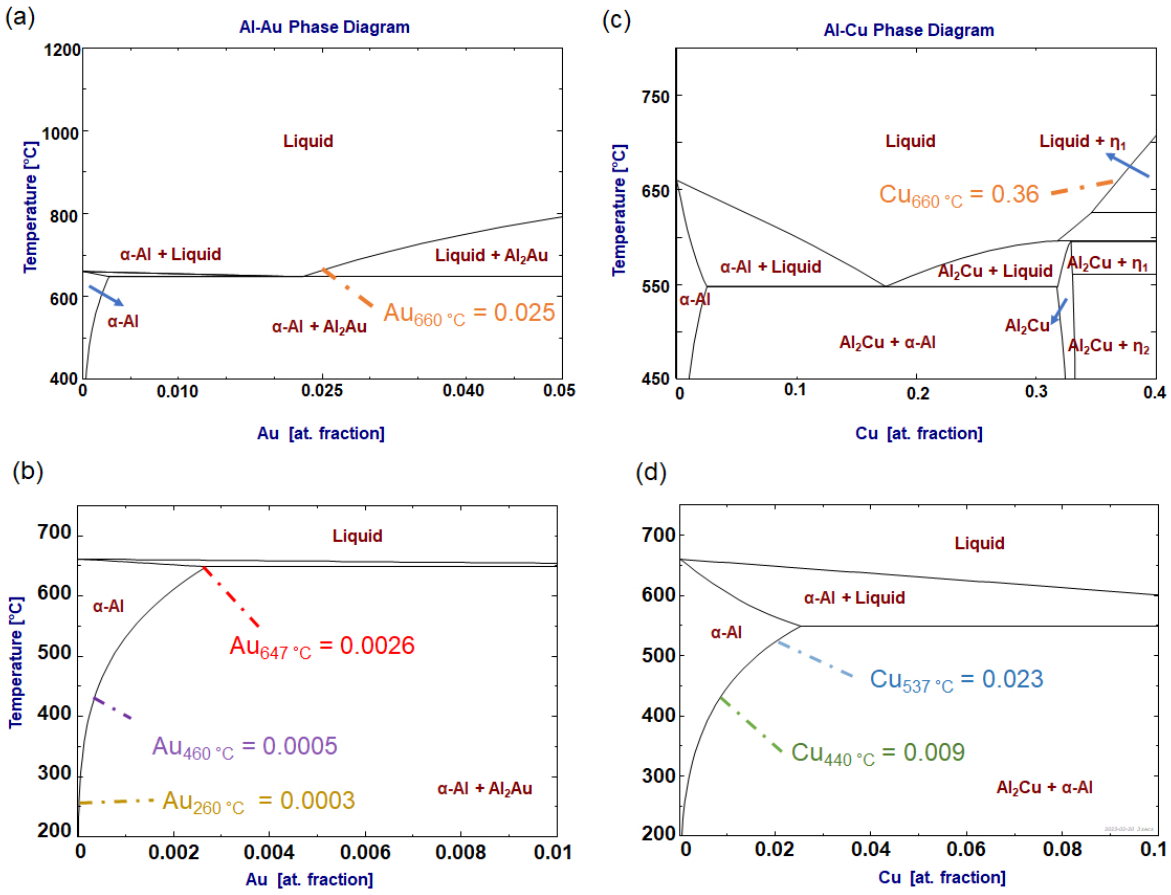

Figure 6.7: Calculated phase diagram of Al-Cu (a, b) and Al-Au (c, d), using the thermochemical software FactSage 8.2 [43]. (a) and (b) display the Al-Au diagram with two different regions, (a) presenting the limit solubility of the liquid phase at 660 °C, and (b) showing the limit of solubility in the solid phase. (c) and (d) show the Al-Cu, whereas (c) depicts the solubility of Au in the liquid phase, and (d) in the solid phase. The numbers indicate the solubility limits at the corresponding annealing temperatures.

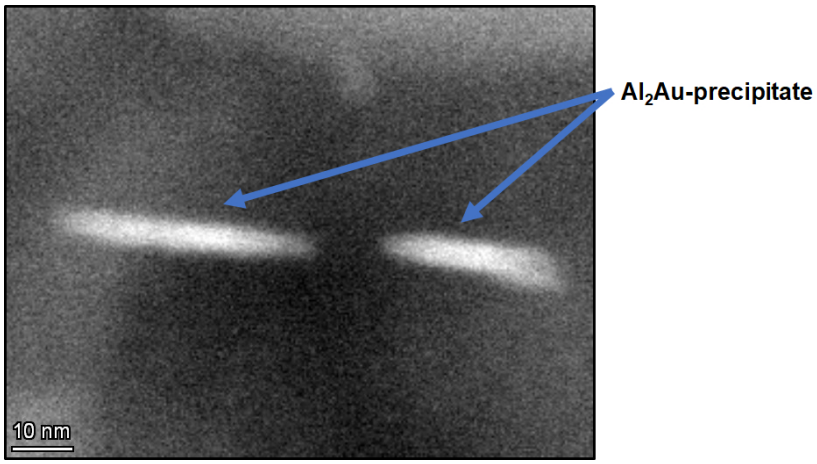

Figure 6.8: HAADF image illustrating the formation of plate-like Al_2Au structures during a heat treatment for 3600 s hour at 250 °C

after 220 s. The equilibrium state is almost reached, 0.05 at-%, see Fig. 6.7 (a). Bourgeois *et al.* [37] report on the bulk and interfacial structures of the Al_2Au after precipitation annealing at 250°C of an Al-Au alloy with 0.2 at-% Au. After an annealing time of 3600 s, they observe the formation of plate-like Al_2Au precipitates with a side length of about 50 nm. A comparable result can be observed in our 250 °C annealing experiment (Fig. 6.8).

6.4 Conclusions

The study of the application of in situ nanoalloying and its utilization for subsequent heat treatment direct within a transmission electron microscope has shown promising results in the examination of the effect of metallurgical processes using nanomaterials and Al matrix as precursors. Herein, the results showed that Au nanoparticles and Cu nanowires can undergo melting and alloying on an Al substrate within an electron microscope. In line with thermodynamic predictions and a higher solubility of Cu in Al, the effect of melting and alloying was more pronounced in the Al-Cu system. The formation of a precipitate composed of likely Al_2Cu was observed in the Al-Cu system. However, the mixing of the alloying agent occurred regardless of the presence of an oxide layer surrounding the NPs/NWs or the Al foil for both systems. The Al-Au system showed comparatively fewer changes, but alloying was achieved and precipitate formation could be observed. Overall, these results suggest that TEM-based *in situ* melting and alloying is a valuable technique for studying the effects of metallurgical procedures on nanomaterials and can provide crucial information for the development of advanced materials with improved properties while

undertaking alloying, heat treatment, and characterization steps entirely within the TEM. Therefore, we can conclude that the *in situ* TEM nanoalloying technique herein presented is a new "lab-on-a-chip" approach for the emerging science of nanometallurgy. Nevertheless, more studies are needed to define a more controlled way of introducing the alloying species to the Al sheet enabling better control of the outcome material composition.

6.5 Reference

[1] Nitika Thakur, Trupti R Das, Santanu Patra, Meenakshi Choudhary, and Sudheesh K Shukla. Miniaturization devices: A nanotechnological approach. In *Electrochemical Sensors*, pages 241–259. Elsevier, 2022.

[2] Langlang Yi, Lei Zhao, Qilu Xue, He Cheng, Hongyan Shi, Jinkun Fan, Shixuan Cai, Guoqian Li, Bo Hu, Liyu Huang, et al. Non-powered capillary force-driven stamped approach for directly printing nanomaterials aqueous solution on paper substrate. *Lab on a Chip*, 20(5):931–941, 2020.

[3] Mariana Medina-Sánchez, Sandrine Miserere, and Arben Merkoçi. Nanomaterials and lab-on-a-chip technologies. *Lab on a Chip*, 12(11):1932–1943, 2012.

[4] Arben Merkoçi and Jörg P Kutter. Analytical miniaturization and nanotechnologies. *Lab on a Chip*, 12(11):1915–1916, 2012.

[5] Du Huang, Zhenya Lu, Qian Xu, Xingyue Liu, Wenbin Yi, Junning Gao, Zhiwu Chen, Xin Wang, and Xiaoyi Fu. Nano-porous al/au skeleton to support mno 2 with enhanced performance and electrodeposition adhesion for flexible supercapacitors. *RSC advances*, 11(35):21405–21413, 2021.

[6] Andrea C Ferrari, Francesco Bonaccorso, Vladimir Fal'Ko, Konstantin S Novoselov, Stephan Roche, Peter Bøggild, Stefano Borini, Frank HL Koppens, Vincenzo Palermo, Nicola Pugno, et al. Science and technology roadmap for graphene, related two-dimensional crystals, and hybrid systems. *Nanoscale*, 7(11):4598–4810, 2015.

[7] Shilei Zhu, Mai Thanh Nguyen, and Tetsu Yonezawa. Micro-and nano-encapsulated metal and alloy-based phase-change materials for thermal energy storage. *Nanoscale Advances*, 3(16):4626–4645, 2021.

[8] Rupesh Kumar, S Ranjith, Hrishikesh Balu, DR Bharathi, K Chandan, and Syed Sagheer Ahmed. Role of nanotechnology in biomedical applications: an updated review. *UPI Journal of Pharmaceutical, Medical and Health Sciences*, pages 39–43, 2022.

[9] Carol López de Dicastillo, Eliezer Velásquez, Adrián Rojas, Abel Guarda, and María José Galotto. The use of nanoadditives within recycled polymers for food packaging: Properties, recyclability, and safety. *Comprehensive Reviews in Food Science and Food Safety*, 19(4):1760–1776, 2020.

[10] Monica Distaso et al. Potential contribution of nanotechnology to the circular economy of plastic materials. *Acta Innovations*, (37):57–66, 2020.

[11] Olga Ivanova, Christopher Williams, and Thomas Campbell. Additive manufacturing (am) and nanotechnology: promises and challenges. *Rapid prototyping journal*, 19(5):353–364, 2013.

[12] Oleg D Neikov and NA Yefimov. *Handbook of non-ferrous metal powders: technologies and applications*. Elsevier, 2009.

[13] Wei Lu and Charles M Lieber. Nanoelectronics from the bottom up. *Nature materials*, 6(11):841–850, 2007.

[14] Shuguang Zhang. Building from the bottom up. *Materials Today*, 6(5):20–27, 2003.

[15] Parvez Iqbal, Jon A. Preece, and Paula M. Mendes. *Nanotechnology: The Top-Down and Bottom-Up Approaches*. John Wiley and Sons, Ltd, 2012.

[16] AG Mamalis. Recent advances in nanotechnology. *Journal of Materials Processing Technology*, 181(1-3):52–58, 2007.

[17] Lina Marcela Hoyos-Palacio, Diana Paola Cuesta Castro, Isabel Cristina Ortiz-Trujillo, Luz Elena Botero Palacio, Beatriz Janeth Galeano Upegui, Nelson Javier Escobar Mora, and Jesus Antonio Carlos Cornelio. Compounds of carbon nanotubes decorated with silver nanoparticles via in-situ by chemical vapor deposition (cvd). *Journal of materials research and technology*, 8(6):5893–5898, 2019.

[18] BG Ravi, S Sampath, R Gambino, JB Parise, and PS Devi. Plasma spray synthesis from precursors: Progress, issues, and considerations. *Journal of thermal spray technology*, 15(4):701–707, 2006.

[19] Lena Staiger, Tim Kratky, Sebastian Günther, Alexander Urstoeger, Michael Schuster, Ondrej Tomanek, Radek Zbořil, Richard W Fischer, Roland A Fischer, and

Mirza Cokoja. Nanometallurgy in solution: organometallic synthesis of intermetallic pd–ga colloids and their activity in semi-hydrogenation catalysis. *Nanoscale*, 13(35):15038–15047, 2021.

[20] Wei Yan, Haoqing Jiang, Wendi Yi, Chengbin Zhao, Yucong Xia, Hengjiang Cong, Lin Tang, Gary J Cheng, Jianhua He, and Hexiang Deng. High-entropy-alloy nanoparticles synthesized by laser metallurgy using a multivariate mof. *Materials Chemistry Frontiers*, 6(19):2796–2802, 2022.

[21] Jianbo Tang, Rahman Daiyan, Mohammad B Ghasemian, Shuhada A Idrus-Saidi, Ali Zavabeti, Torben Daeneke, Jiong Yang, Pramod Koshy, Soshan Cheong, Richard D Tilley, et al. Advantages of eutectic alloys for creating catalysts in the realm of nanotechnology-enabled metallurgy. *Nature communications*, 10(1):1–14, 2019.

[22] Riccardo Ferrando, Julius Jellinek, and Roy L Johnston. Nanoalloys: from theory to applications of alloy clusters and nanoparticles. *Chemical reviews*, 108(3):845–910, 2008.

[23] George Marx. Interstellar vehicle propelled by terrestrial laser beam. *Nature*, 211(5044):22–23, 1966.

[24] Ho-Ting Tung and Artur R Davoyan. Low-power laser sailing for fast-transit space flight. *Nano Letters*, 22(3):1108–1114, 2022.

[25] Mohammadrasoul Taghavi, Mohammad Mahdi Salary, and Hossein Mosallaei. Multifunctional metasails for self-stabilized beam-riding and optical communication. *Nanoscale Advances*, 4(7):1727–1740, 2022.

[26] Matheus A Tunes, Cameron R Quick, Lukas Stemper, Diego SR Coradini, Jakob Grasserbauer, Phillip Dumitraschkewitz, Thomas M Kremmer, and Stefan Pogatscher. A fast and implantation-free sample production method for large scale electron-transparent metallic samples destined for mems-based in situ s/tem experiments. *Materials*, 14(5):1085, 2021.

[27] JL Murray, H Okamoto, and TB Massalski. The al- au (aluminum-gold) system. *Bulletin of Alloy Phase Diagrams*, 8(1):20–30, 1987.

[28] H Okamoto. Al-au (aluminum-gold). *Journal of Phase Equilibria and Diffusion*, 26(4):391, 2005.

[29] SK Son, M Takeda, M Mitome, Y Bando, and T Endo. Precipitation behavior of an al–cu alloy during isothermal aging at low temperatures. *Materials letters*, 59(6):629–632, 2005.

[30] M Von Heimendahl. Precipitation in aluminum-gold. *Acta Metallurgica*, 15(9):1441–1452, 1967.

[31] WF Miao and DE Laughlin. Effects of cu content and preaging on precipitation characteristics in aluminum alloy 6022. *Metallurgical and Materials Transactions A*, 31(2):361–371, 2000.

[32] Lukas Stemper, Matheus A Tunes, Phillip Dumitraschkewitz, Francisca Mendez-Martin, Ramona Tosone, Daniel Marchand, William A Curtin, Peter J Uggowitzer, and Stefan Pogatscher. Giant hardening response in almgzn (cu) alloys. *Acta Materialia*, 206:116617, 2021.

[33] Stefan Pogatscher, Helmut Antrekowitsch, and Peter J Uggowitzer. Interdependent effect of chemical composition and thermal history on artificial aging of aa6061. *Acta materialia*, 60(15):5545–5554, 2012.

[34] Diego SR Coradini, Matheus A Tunes, Thomas M Kremmer, Claudio G Schön, Peter J Uggowitzer, and Stefan Pogatscher. Degradation of cu nanowires in a low-reactive plasma environment. *npj Materials Degradation*, 4(1):33, 2020.

[35] Ondrej Zobac, Ales Kroupa, Adela Zemanova, and Klaus W Richter. Experimental description of the al-cu binary phase diagram. *Metallurgical and Materials Transactions A*, 50(8):3805–3815, 2019.

[36] G Piatti and G Pellegrini. The structure of the unidirectionally solidified al-al2au eutectic. *Journal of Materials Science*, 11(5):913–924, 1976.

[37] Laure Bourgeois, Zezhong Zhang, Jiehua Li, and Nikhil V Medhekar. The bulk and interfacial structures of the η (al2au) precipitate phase. *Acta Materialia*, 105:284–293, 2016.

[38] Phillip Dumitraschkewitz, Matheus A Tunes, Cameron R Quick, Diego Santa Rosa Coradini, Thomas M Kremmer, Parthiban Ramasamy, Peter J Uggowitzer, and Stefan Pogatscher. Mems-based in situ electron-microscopy investigation of rapid solidification and heat treatment on eutectic al-cu. *Acta Materialia*, 239:118225, 2022.

[39] Zaoli Zhang and Dangsheng Su. Behaviour of tem metal grids during in-situ heating experiments. *Ultramicroscopy*, 109(6):766–774, 2009.

[40] Diego Santa Rosa Coradini, Matheus Araujo Tunes, Patrick Willenshofer, Cameron Quick, Thomas Kremmer, Stefan Luidold, Peter J Uggowitzer, and Stefan Pogatscher. Unravelling nanometallurgy with in situ electron-microscopy: A case study with cu nanowires. *Preprint available at SSRN-4313569*, 2023.

[41] Takeshi Egami, Madhusudan Ojha, Donald M Nicholson, Dmitri V Louzguine-Luzgin, Na Chen, and Akihisa Inoue. Glass formability and the al–au system. *Philosophical Magazine*, 92(6):655–665, 2012.

[42] Saurabh Bajaj, Michael G Haverty, Raymundo Arróyave, and Sadasivan Shankar. Phase stability in nanoscale material systems: extension from bulk phase diagrams. *Nanoscale*, 7(21):9868–9877, 2015.

[43] Ch W Bale, P Chartrand, SA Degterov, G Eriksson, K Hack, R Ben Mahfoud, J Melançon, AD Pelton, and S Petersen. Factsage thermochemical software and databases. *Calphad*, 26(2):189–228, 2002.

Chapter 7

Conclusion and Outlook

The size effect in materials at the nanoscale is a matter of increasing importance with the reduction in the volume of the devices used in day-to-day life. Notwithstanding, the increase in significance ensues more challenges that surface with the intense usage of nanodevices or equipment reliant on them. Therefore, understanding size-related effects is of paramount importance for the development of metallurgy in such a field. So, by taking into account the topics of degradation and manufacturing, the present results aimed at unveiling some of the possible phenomena that might affect nonferrous metals while exposed to a distinct environment while a nanometric scale. The first publication presented in Chapter 4 revolved around the degradation of a Cu nanowire (NW) when exposed to a low-reactive plasma environment. The results displayed a surprising effect regarding the unexpected degradation presented in the form of oxidation and formation of nanoclusters with an increase in exposure time. The surprising part, however, doesn´t concern the oxidation, but its mechanism. Hence, it was considered that the degradation was a modified type of vapor-solid-solid mechanism where the existent monoatomic oxygen present within the plasma reacted. The reaction generated heat and promoted the melting of a nanorough region. Afterward, a monoatomic oxygen atom would chemisorb on this newly generated nano-molten region reacting into Cu-oxide clusters. Chapter 5 explored a distinct aspect of the size effect over a Cu NW, and its sublimation within a TEM. More specifically, the effect herein described consisted of its sublimation at a temperature lower than expected. The unexpected phenomena were attributed to

the size effect, as the high surface area-to-volume ratio in the NW can significantly affect their thermodynamic properties. The results showed that Cu nanowires exhibit lower sublimation temperatures compared to their bulk counterparts due to the existence of active spots, which are regions with sharp edges with radii of less than 5 nm. This information is crucial in the development of nanodevices, as it provides insight into the thermal stability of materials used in such applications. Finally, in Chapter 6, the focus shifted to the manufacturing aspect of nanometallurgy. The aim was to investigate the possibility of nanoalloying within a TEM environment, using Al as a solute material and Cu and Au as alloy elements. Thus, a common metallurgical methodology was used to achieve it, alloying by melting. Two different systems were analyzed, Al-Cu and Al-Au, due to their different solubility levels, chemical stability, and well-established thermodynamical studies in the Literature. The results showed successful nanoalloying between the elements and the potential for using in situ TEM observations to study and control such processes. Another interesting aspect of this methodology was the possibility of observing precipitation sequences and the development of the system under different conditions of an in situ prepared alloy. In conclusion, the studies presented in this thesis provide insight into the size-related effects of nonferrous metals at the nanoscale, with a focus on degradation, thermodynamic properties, and manufacturing. The findings presented herein contribute to the development of nanometallurgy and can aid in the design and implementation of nanodevices and related technologies.